The Dissertation Committee for Benjamin Lee Byerly Certifies that this is the approved version of the following dissertation:

Constraints from mantle xenoliths on the geodynamic evolution of Earth's upper mantle

Committee:

John C. Lassiter, Supervisor

James E. Gardner

Stephen P. Grand

Michael C. Rowe

Donggao Zhao

Constraints from mantle xenoliths on the geodynamic evolution of Earth's upper mantle

by

Benjamin Lee Byerly, B.S.

Dissertation

Presented to the Faculty of the Graduate School of
The University of Texas at Austin
in Partial Fulfillment
of the Requirements
for the Degree of

Doctor of Philosophy

The University of Texas at Austin
May 2014

Dedication

This dissertation is dedicated to my friends and family, especially my parents Maud and Gary, and my wife Elizabeth.

Acknowledgements

I could not have completed this dissertation without the help and guidance of many people. Foremost is my advisor, John Lassiter, whom I first met six years ago. Shortly after I applied to the University of Texas for graduate school, John telephoned me to talk about a project that would use mantle xenoliths to characterize the evolution of the mantle beneath the Rio Grande Rift. I was immediately drawn to the topic and the opportunity to learn from and work with John. I quickly learned from John the value of being able express and explain my ideas in a clear but concise manner. I also learned very quickly not to make the same mistake twice. Through this project and the many lessons he taught me, John turned me from a geologist to a geochemist.

My committee members have provided invaluable assistance and insight to my project during my time here. Jim Gardner helped me to sharpen my skills in petrology and to learn a thing or two about volcanology. Steve Grand and his students engaged me with many interesting discussions about the latest tomographic models of the Rio Grande Rift and adjacent regions. Mike Rowe helped in collecting many of the xenoliths I worked on and I can always rely on him to show up at my AGU and Goldschmidt posters ready for new discussions about our respective projects. Donggao Zhao trusted me very early on with the controls of the electron microprobe and was always eager to talk about my samples and share his own insights from his personal research experiences with mantle xenoliths.

Many faculty members helped me out along the way. Jaime Barnes has been a great mentor and friend who has provided me with considerable career advice. Our myriad conversations about serpentinites, peridotites, and the composition of the mantle

wedge were always a welcome diversion towards thinking about different mantle processes. Doug Smith has been a great source of information as the resident expert on Colorado Plateau mantle. He and I have had many conversations about my xenoliths and how they fit into the whole picture of the western North America lithosphere. He is always excited to peek at my thin sections and to have a chance converse about metasomatic textures.

I spent a tremendous amount of time in various mass spectrometry labs throughout the department and could not have accomplished what I have without the guidance and assistance of their patrons. Nate Miller was always happy to break out the 150-micron laser slit and do some "easy" pyroxene analyses. Staci Loewy and Eric James could always be counted on to help when something just wasn't right with the TIMS or whatever column chemistry I was doing. Alison Koleszar and Zhaoping Yang kept the Isoprobe alive and running, without which I could not have finished this project. Jaime Barnes and Toti Larsen opened me up to the world of stable isotopes and the oxygen line. Lastly, Todd Housh taught me all of the ins and outs of mass spectrometry.

My friends and fellow graduate students always kept me on track (emotionally and scientifically). I am especially grateful for assistance and insight from the other High-T geochemistry students: Lindsay Szramek, Rudra Chatterjee, Ruohan Gao, and Ed Marshall. Rudra and Ruohan are very familiar with frustrations that come from the geologic pace of wet lab chemistry and TIMS paired with the overwhelming desire for more data. Bobby, Jay, Kenny, and Ethan were with me for the long run and could always be counted on for a welcome distraction from the tedium.

The instructors for whom I TA'd gave me myriad lessons on teaching undergrads and helped me to develop my personal teaching philosophy. I have especially fond memories of the springs and summers that I spent teaching field courses with Mark

Helper and Randy Marrett. They had the audacity to recruit a geochemist to teach undergrads proper field techniques, which gave me the opportunity to visit world-class locales all over the western U.S. and learn the meaning of "bad fun".

The Jackson School of Geosciences provided me with generous financial support in the form of teaching and research assistantships as well as with a generous budget with which to conduct my research.

The National Science Foundation provided financial assistance in the form of grants EAR-0648409 and EAR-0911253.

Philip Guerrero always kept me on track and guided me through the maze of paperwork that is required of graduate students. Without him I would have forgotten to fill out just about every single form ever. He is great friend that is always willing to hear me vent about the pitfalls of graduate school. Philip's FFF brightened many Friday mornings.

My family has provided me with invaluable support. My parents exposed me to geology from a very early age and it was their passion for earth science that inspired me to become the geologist that I am today. My brother, Zach, did everything that good older brothers do, but most importantly he has been a constant source of encouragement for as long as I can remember. I couldn't have done any of this without the love and support of my wife, Elizabeth. She has put up with far too many late nights, long weeks, bad moods, and rants about mass spectrometers not working. In spite of this, she never hesitates to brighten my day, take care of me, and be the best wife ever.

Constraints from mantle xenoliths on the geodynamic evolution of Earth's upper mantle

Benjamin Lee Byerly, PhD

The University of Texas at Austin, 2014

Supervisor: John C. Lassiter

Geophysical studies identify a region of slow seismic velocity mantle beneath the central Rio Grande rift that potentially represents a region of hot asthenospheric mantle that has replaced destabilized lithosphere. We determine that the majority of mantle xenoliths from Elephant Butte on the central Rio Grande rift axis are, based on their geochemical affinity to depleted mantle, derived from asthenospheric mantle that has accreted to the base of the Proterozoic lithosphere. Using mantle heat flow models, we estimate the boundary between residual lithosphere and accreted asthenosphere to be at ~45km depth. The amount of lithosphere thinning that has occurred cannot be accounted for by rift-related extension and we therefore suggest that convective removal of a large portion of Proterozoic lithosphere has occurred.

Convecting upper mantle-derived peridotites display extreme isotopic depletions that are not observed in mid-ocean ridge basalts (MORB). Previous studies suggest that these isotopically ultradepleted domains represent rare refractory mantle domains that do not participate in MORB petrogenesis. We demonstrate the isotopically ultradepleted domains are not only a ubiquitous feature of convecting upper mantle, but are also capable of melting if advected beneath mid-ocean ridges. To explain the lack of MORB

with ultradepleted isotopes, we suggest that MORB compositions are biased towards fertile enriched source components. Estimates of upper mantle composition based on MORB therefore overestimate the fertility of the upper mantle.

The Lu-Hf system is commonly used to estimate the timing of melt depletion events in the lithospheric mantle. This is typically done with pseudoisochrons from genetically related mantle xenoliths. Most studies, however, misinterpret Lu/Hf – Hf isotopes correlations by using Cpx Lu/Hf ratios when whole rock Lu/Hf ratios are appropriate due to equilibration above the Lu-Hf closure temperature. Hafnium isotopes do not typically correlate with indicators of melt depletion, which suggests that Hf isotopes do not record ancient melting events. This is likely due to overprinting of Hf isotopes by later metasomatic events.

Table of Contents

List of Tables

List of Figures

Introduction

Understanding the composition of Earth's chemical reservoirs and how they have evolved through deep time are fundamental questions in the Earth Sciences that can ultimately help us understand how the Earth formed. Shortly after its formation, Earth underwent chemical differentiation (Boyet and Carlson, 2006; Kleine et al., 2002) and evolved to form a metallic core and a silicate crust and mantle. The extent of chemical exchange between the core and mantle is a hotly debated topic (Brandon and Walker, 2005). However, the complementary nature of the crust and mantle is unequivocal: partial melting of the mantle forms crust, which can later be recycled back into the mantle via tectonic processing. Because the mantle is largely inaccessible, Earth scientists rely heavily on the use of primitive magmas to estimate the composition of the mantle, although this requires intimate knowledge of the melting process in order to infer parental compositions. Abyssal peridotites and massif peridotites allow for direct sampling of mantle material, but many primary chemical signatures are obscured during the emplacement of these rocks at the Earth's surface. Mantle xenoliths, which are typically hosted in primitive lavas, provide a snapshot of the local mantle at the time of their eruption, and are incredibly useful for studying Earth's deep interior. Mantle xenoliths retain myriad signatures of melt extraction and re-enrichment that can provide details of the geodynamic evolution of Earth's mantle and crust. Through this we can develop a better understanding of the composition of the Earth.

In this dissertation I address three problems related to the geodynamic evolution of Earth's upper mantle that we solve through geochemical analyses of two different suites of mantle xenoliths. The first study focuses on the modification and convective removal of lithospheric mantle material from a region beneath the central Rio Grande Rift. The second addresses the perceived difference between mantle sampled by mid-ocean ridge basalts (MORB) and mantle with extremely depleted isotopic compositions that are observed in mantle samples from various tectonic settings. Lastly I examine the Lu-Hf system in mantle peridotites, which is a relatively new, but potentially useful, technique for studying lithosphere stabilization. In doing so, I outline the observations and assumptions that are intrinsic to correctly interpreting Lu-Hf data.

USING XENOLITH PROVENANCE TO DETERMINE THE EXTENT OF LITHOSPHERIC MANTLE MODIFICATION AND DESTRUCTION.

The Rio Grande rift (RGR) is a recently deformed tectonic province that borders the relatively stable Colorado Plateau. It provides a great opportunity for understanding the underlying causes of deformation and destabilization of crust and mantle. Tomographic study of the region Gao et al. (2004) revealed a large region of mantle with anomalously slow P- and S-wave velocities. There are two potential causes for this seismically slow mantle: pervasive infiltration of melt/fluids into Proterozoic lithospheric mantle or the presence of hot asthenospheric mantle at shallow (<40km) depths. The latter would require significant destruction/removal of pre-existing lithospheric mantle material because the extent of lithosphere thinning due to rift-related extension is small compared to that required by the tomographic models.

To address this problem and evaluate the structure of the mantle beneath the central Rio Grande rift (RGR), I examined the major element, trace element, and isotopic compositions of a suite of xenoliths to constrain their provenance (Proterozoic lithosphere or asthenosphere). Our results show that a significant portion of the Proterozoic lithosphere has been convectively removed and replaced with asthenospheric mantle. This process of lithosphere destruction has been increasingly recognized in regions of cratonic and non-cratonic mantle and is important both for understanding the processes that destabilize ancient crust and mantle, but also is a potentially significant source of recycled material in the convecting mantle.

DETERMINING THE ROLE THAT ISOTOPICALLY ULTRA-DEPLETED MANTLE DOMAINS PLAY IN MORB PETROGENESIS.

Ultra-depleted mantle domains, which posses unradiogenic Sr, radiogenic Nd and Hf isotopes that extend well beyond the range observed in MORB, have been observed globally in asthenosphere-derived samples (abyssal peridotites and OIB xenoliths). We also observe these characteristics in a suite of fertile asthenosphere-derived samples from the RGR, which, unlike abyssal peridotites have not been potentially subject to high-degrees of recent melt extraction. This presents the question, if MORB are derived from mantle with ultra-depleted isotopic compositions, why aren't these isotopic compositions observed in MORB? I argue that during melting of a compositionally heterogeneous peridotitic mantle, accumulated melts (i.e. MORB) will preferentially sample the most fertile mantle components (which have the least-depleted isotopic compositions). Additionally, small amounts of an isotopically enriched mantle component (e.g. eclogite/pyroxenite derived from recycled MORB) can also contribute to MORB petrogenesis shifting MORB isotopic compositions to more moderate values. An important result of this is that studies that attempt to use MORB compositions to estimate the composition of the depleted mantle (DMM) will over estimate the fertility of DMM. It also reinforces the idea that the convecting mantle is very heterogeneous in major elements, trace elements, and isotopes as a result of on-going melt extraction and addition of recycled lithospheric material.

EVALUATING THE ROLES THAT METASOMATISM AND HFSE/REE PARTITIONING BETWEEN CLINOPYROXENE AND ORTHOPYROXENE HAVE IN THE INTERPRETATION OF SUB-CONTINENTAL LITHOSPHERIC MANTLE (SCLM) LU-HF GEOCHRONOLOGY.

The timing of lithospheric mantle formation is an important piece of information for inferring the conditions that stabilize cratonic and non-cratonic mantle. The oldest crustal material in a given region is typically the same age as the underlying lithospheric mantle (Carlson et al., 2005). This supports the idea that crust and SCLM formation is a complementary process during which the crust is coupled to, and ultimately stabilized by, the lithospheric mantle. The Re-Os system has been the primary means of determining the age of lithospheric mantle material. However there are some inherent problems with that system, such as the possibility of Re mobility during metasomatism, the presence of multiple generations of Os-bearing minerals within a single sample (Harvey et al., 2011), and the large errors associated with Os model ages. The Lu-Hf system has recently been incorporated into studies of SCLM material to complement the Re-Os system to date melt-depletion/SCLM formation. If implemented correctly it can potentially provide additional age constraints on melt depletion events and lithosphere formation.

Lu-Hf ages are typically estimated using clinopyroxene ^{176}Hf/^{177}Hf - Lu/Hf pseudoisochrons. This assumes either that the clinopyroxene Lu/Hf ratio is identical to the whole rock Lu/Hf ratio, or that samples are below the closure temperature of the Lu-Hf system. The Lu-Hf closure temperature, however, is thought to be low relative to average equilibration temperatures of spinel peridotites. Several studies suggest that orthopyroxene, which typically has a higher Lu/Hf ratio than cpx, can be a significant host of Lu and Hf in melt-depleted rocks (Bedini and Bodinier, 1999; Eggins et al., 1998; Witt-Eickschen and O'Neill, 2005), which would result in cpx and the whole rock having different Lu/Hf ratios. Thus, for samples below their Lu-Hf closure temperature it is necessary to understand the whole rock budget and therefore whole rock Lu/Hf ratio in order to correctly evaluate Lu-Hf data.

We measured Lu-Hf isotopes and trace elements on two compositionally diverse suites of mantle xenoliths to constrain the closure temperature of the Lu-Hf system and to constrain whole rock trace element budgets and Lu/Hf ratios. We find that most studies overestimate and misinterpret Lu-Hf ages because most samples are above the closure temperature of the Lu-Hf system because clinopyroxene has lower Lu/Hf than the whole rock. Additionally Hf isotopes do not correlate with indicators of melt depletion, which suggests that Lu/Hf – Hf isotope correlations do not track ancient melt depletion. Instead they may reflect pervasive metasomatism of SCLM.

Chapter 1: Evidence from Mantle Xenoliths for Lithosphere Removal Beneath the Central Rio Grande Rift

ABSTRACT

Seismic tomography beneath the Central Rio Grande Rift (RGR) at ~34° N shows a low P and S wave velocity zone in the mantle that extends up the base of the Moho. This low-velocity region has been interpreted by Gao et al. (2004) to be the result of convective removal of a portion of the once >100km thick Proterozoic lithosphere. The amount of extension in the central RGR is thought to be low (~25%) and thus cannot account for the amount of lithosphere thinning suggested by seismic tomography. We measured whole rock and mineral major element, trace element, and isotopic compositions of spinel-peridotite xenoliths erupted along the central axis of the rift (Elephant Butte) and the eastern margin of the Colorado Plateau (Cerro Chato) to determine their depth of origin and mantle provenance and to test the delamination hypothesis. If lithosphere removal has not occurred and the low P and S wave velocities are instead the result of hydration or melt infiltration in the lithosphere, then xenoliths erupted on the rift axis should have geochemical compositions similar to Proterozoic sub-continental lithospheric mantle (SCLM). At Cerro Chato, on the margin of the Colorado Plateau, xenoliths were derived from ~60km depth and have geochemical signatures similar to Proterozoic sub-continental lithospheric mantle (e.g. refractory major element compositions, LREE-enrichment, enriched Sr and Nd isotopes, unradiogenic Os isotopes). At Elephant Butte, along the central rift axis, two distinct groups of xenoliths are present. The majority of xenoliths from Elephant Butte are LREE-depleted and have fertile major element compositions. Additionally, these xenoliths have isotopic signatures similar to the range for DMM (e.g. $^{87}Sr/^{86}Sr$ ranging from 0.7018-0.7023, ε_{Nd} ranging

from 7-21, and $^{187}Os/^{188}Os$ ranging from 0.122-0.130). We interpret this group of xenoliths to be derived from asthenospheric mantle. A less-abundant group of xenoliths at Elephant Butte are LREE enriched, have refractory major element compositions, enriched Sr, Nd, and Pb isotopes, and unradiogenic Os isotopes. These are characteristic of Proterozoic SCLM. Both groups of xenoliths from Elephant Butte are derived from ~45km depth. We interpret the suite of xenoliths at Elephant Butte to have sampled what was recently the base of the Proterozoic SCLM. We conclude that a portion of the mantle lithosphere has been removed which allowed modern convecting mantle (DMM) to be emplaced at the base of the pre-existing SCLM.[1]

1.1 INTRODUCTION

Lithosphere removal has been called upon to explain numerous geodynamic processes and geophysical anomalies found at active and passive continental rifts. Removal of the lithosphere can cause rapid uplift, increased surface heat flow, lowered shallow mantle seismic velocities, and increased magmatism (Bird, 1979), (Kay and Kay, 1993). Lithosphere removal has been proposed by Gao et al. (2004), Le Pourhiet et al (2006), and Wallner and Schmeling (2010) to have occurred in the Rio Grande Rift, Basin and Range, and East African Rift, respectively, based on observations of rapid uplift and/or shallow mantle wave speed anomalies. It is unclear, however, if removal of the lithosphere triggers rifting, or if rifting causes lithosphere removal. Removal of the lithosphere can trigger magmatism, which may soften the crust resulting in continental break up (Lin and Wang, 2006). Alternatively, reduction of the viscosity and strength of the lower crust during rifting could also induce lithosphere removal through delamination

---

[1] Portions of this chapter were published in 2012 in *Earth and Planetary Science Letters* 355-356, 82-93.

(Wallner and Schmeling, 2010) or convective instability (England and Houseman, 1989). If lithosphere removal has occurred beneath the Rio Grande Rift, a nascent passive rift system, then additional study may further elucidate the timing of removal and the causal association between rifting and lithosphere removal.

Removal of the lithosphere beneath the central Rio Grande rift (RGR) was proposed by Gao et al. (2004) to explain anomalously slow P and S wave velocities in the mantle extending to shallow depths (<45km). They proposed that the slow mantle velocities are due to hot asthenosphere extending up to the Moho. Thinning of the lithosphere is also called upon by McMillan et al. (2000) to explain the shift of basalt compositions in the southern RGR. Oligocene lavas in the southern RGR have enriched Sr and Nd isotopes and have trace element patterns similar to continental arc lavas. Starting around 10 Ma many lavas were erupted which have depleted Sr and Nd isotopes and trace element patterns similar to ocean-island basalts (OIB). This change in erupted compositions is interpreted by McMillan (1998) and McMillan et al. (2000) to reflect a change in magmatic source regions from lithosphere to asthenosphere starting at 10Ma. Keller et al. (1979) and Riter and Smith (1996) suggest that the Rio Grande Rift lithosphere had a thickness of 100-125 km prior to rifting. Given approximate extension of ~25% since mid-Oligocene in the central RGR (Cather et al., 1994) and (Chapin and Cather, 1994) the lithosphere today should have a thickness on the order of 75-90 km if only passive rifting has occurred. This is inconsistent with slow P and S wave velocities extending to less than 45km. These inconsistencies suggest that thinning due to extension alone cannot explain the shallow slow seismic wave velocities beneath the central RGR and that removal of the lithosphere has occurred. An alternative hypothesis is that hydration/melt infiltration in the lithosphere has occurred, which could reduce seismic wave velocities without requiring significant lithosphere thinning or removal.

We have examined spinel peridotite xenoliths contained in recent volcanic eruptions from the central RGR and eastern Colorado Plateau to determine whether they derive from Proterozoic lithosphere or recently emplaced asthenospheric mantle. The depth of origin of the xenoliths is constrained to be less than ~60km based on the presence of spinel and absence of garnet (Green and Ringwood, 1970). If the xenoliths derive from asthenospheric mantle, this would require significant thinning of the lithosphere, beyond the amount due to passive extension alone. Therefore, determining the provenance of mantle xenoliths from the central RGR provides a method for independently testing the delamination hypothesis of Gao et al.

Xenoliths from lithospheric and asthenospheric mantle can be distinguished based on a number of petrologic and geochemical characteristics. Modern convecting asthenosphere (DMM) has a relatively fertile composition (e.g. Al_2O_3 ~3.5-4.5 wt. %) and is LREE depleted (Sun and McDonough, 1989); (Salters and Stracke, 2004); (Workman and Hart, 2005). Depleted-MORB source mantle has unradiogenic strontium isotopes ($^{87}Sr/^{86}Sr$ ranging from 0.7020-7030) and depleted neodymium isotopes ($^{143}Nd/^{144}Nd$ ranging from 0.5131-0.5134) (Hart, 1988). The $^{187}Os/^{188}Os$ of most abyssal peridotites ranges from 0.118-0.130 with an average around 0.125 (Standish et al., 2002). Abyssal peridotites are considered to have similar isotopic compositions to DMM.

SCLM xenoliths, in contrast, often display variable LREE enrichment, unradiogenic $^{187}Os/^{188}Os$ (<0.12), enriched Sr and Nd isotopes, and often have more refractory major element compositions (2.3±1.1 wt. % Al_2O_3) relative to asthenospheric mantle (Frey and Prinz, 1978); (Menzies et al., 1987); (Meisel et al., 2001); (McDonough, 1990). The trend in SCLM xenoliths from fertile lherzolites towards refractory harzburgites is considered to be the result of ancient melt extraction (Frey and Green, 1974). The time-integrated effect of melt depletion results in a trend towards less radiogenic osmium isotopes because rhenium is incompatible whereas osmium is compatible during mantle partial melting (Meisel et al., 2001). The LREE-enrichment and elevated $^{87}Sr/^{86}Sr$ in SCLM are thought to be the result of metasomatism by fluids or melts percolating through the lithosphere at various periods subsequent to its formation (Downes, 2001). Xenoliths from the Colorado Plateau (CP) commonly display the above characteristics (Smith and Riter, 1997), (Alibert, 1994), (Roden and Shimizu, 1993), (Smith, 2000). Mantle xenoliths from the Colorado Plateau provide an approximation for the composition of lithospheric mantle beneath the RGR prior to rifting.

1.2 BACKGROUND AND SAMPLE LOCATION

Formation of the Rio Grande Rift initiated at the end of the Laramide orogeny, most likely in response to the shift from a compressional to extensional regime in western North America in the mid-Cenozoic due to the cessation of low-angle subduction and subsequent rollback of the Farallon plate (Humphreys, 1995); (Lawton and McMillan, 1999). The rift extends from southern Colorado to northern Mexico (Figure 1.1). Rifting and its associated volcanism started in the southern rift about 36 Ma (Mack et al., 1994), whereas rifting in the northernmost portions did not begin until about 27 Ma (Chapin, 1979). Early volcanism and normal faulting associated with the onset of rifting was followed by a long period of volcanic quiescence in the middle Miocene, which some attribute to a change in the source of magmatism from lithosphere to asthenosphere

(Baldridge et al., 1980); (McMillan et al., 2000). This change was marked in the southern rift by a shift in the composition of lavas erupted after ~10Ma from melts with enriched Sr and Nd isotopes and unradiogenic Pb isotopes to melts with depleted Sr and Nd isotopes and radiogenic Pb isotopes.

We collected xenoliths from two localities in central New Mexico: Elephant Butte (central RGR), and Cerro Chato (eastern margin of the Colorado Plateau) (Figure 1.1). Both sites are located close to the LARISTRA array line, which Gao et al. (2004) used in their seismic study of the central RGR. The Elephant Butte locality consists of a series of Pliocene or younger cinder cones and associated lava flows (Bachman and Mehnert, 1978); (Baldridge, 1979b) located on the axis of the central rift, south of the LARISTRA array. The lavas range from basalt to trachy-basalt to tephrite basanite (Chatterjee et al., 2011). Xenoliths from Elephant Butte have been previously studied by (Warren, 1978); (Warren et al., 1979); (Baldridge, 1979a); (Kil and Wendlandt, 2004) and (Kil and Wendlandt, 2007). However, no isotopic data have previously been reported for xenoliths from this location.

Cerro Chato is a cinder cone in the Zuni-Bandera volcanic field, which is on the eastern margin of the Colorado Plateau in the CP/RGR transition zone. The host lava for the Cerro Chato xenoliths is a trachy-basalt (Rowe, pers. comm.) which erupted <700 kya (Laughlin et al., 1993). Cerro Chato is close (<75km) to the LARISTRA array where it crosses the Jemez Lineament near Mt. Taylor. Study of the xenolith suite at Cerro Chato has not been previously published.

These xenolith suites were chosen because they recently (<3 Ma) sampled mantle beneath the Rio Grande rift and the eastern margin of the Colorado Plateau. The sites were also chosen due to their proximity to the LARISTRA line. The xenoliths from Elephant Butte sample portions of the mantle which, presumably, have been disturbed by Rio Grande rifting over the past ~37Ma. The xenoliths from Cerro Chato, on the other hand, potentially provide a proxy for less-disturbed, pre-rift lithospheric mantle. Combined, the xenoliths from Elephant Butte (central RGR axis) and Cerro Chato (eastern CP margin) can help to generate a cross-section of the mantle perpendicular to the rift.

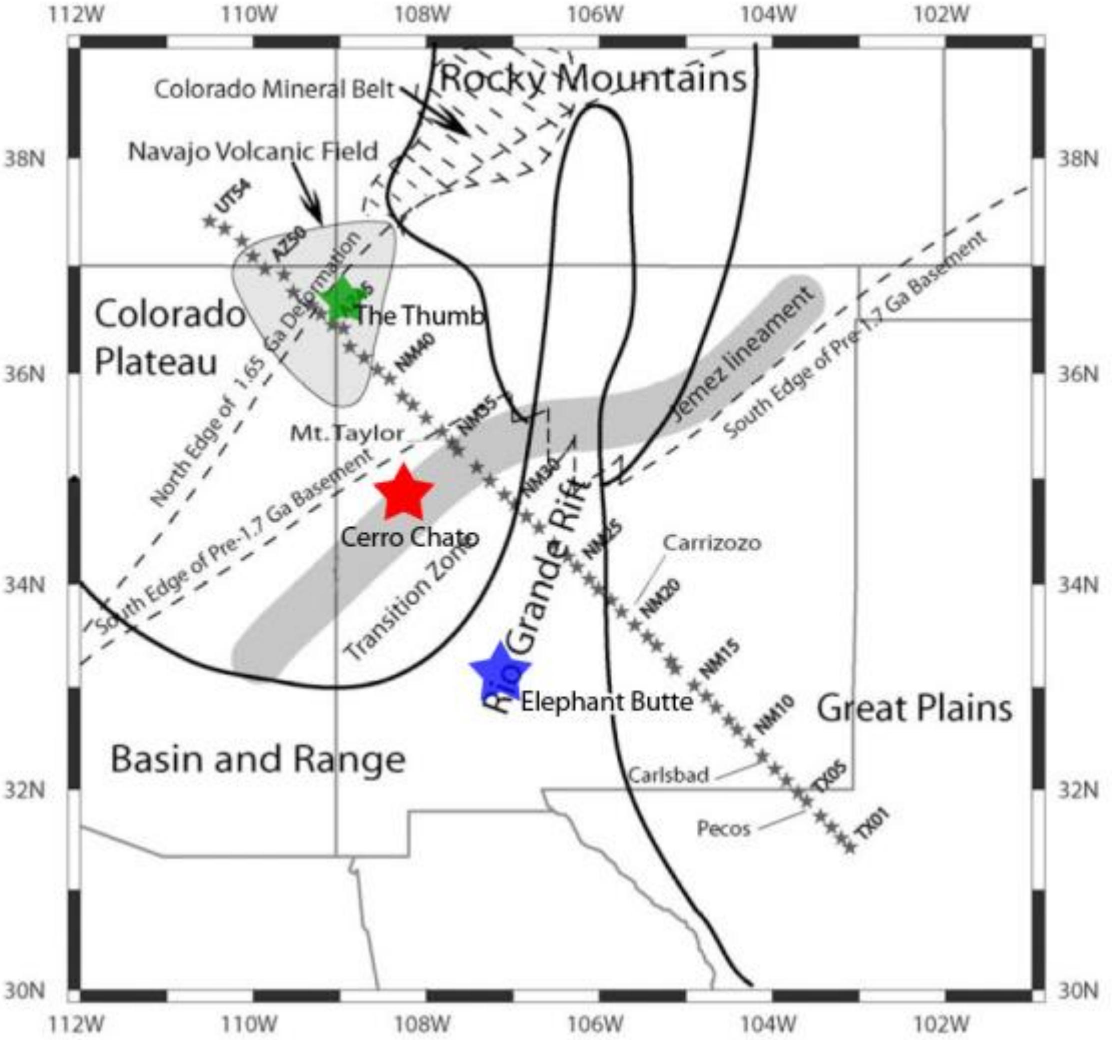

Figure 1.1 Map showing locations of Elephant Butte and Cerro Chato xenolith localities

Elephant Butte (blue star) and Cerro Chato (red star). Also shown: The Thumb (green star), LaRistra seismic survey line (grey stars), and locations of North American geologic provinces. After Gao et al. (2004).

1.3 PETROGRAPHY

Mantle xenoliths from Elephant Butte are spinel peridotites consisting of olivine, orthopyroxene, clinopyroxene and spinel in varying proportions. All are group-I xenoliths according the classification scheme of Frey and Prinz (1978). Most samples are lherzolites, however some harzburgites and dunites are present. The Cerro Chato xenoliths are more diverse, although all are spinel peridotites. Group-I and group-II xenoliths are present. The group-I xenoliths are lherzolites, harzburgites, and dunites. The group-II xenoliths are clinopyroxene-rich lherzolites and wehrlites. More detailed description of the xenolith petrology can be found in the supplementary materials.

1.4 ANALYTICAL METHODS

Major and trace elements were measured for whole rock xenoliths by XRF and ICP-MS at the Washington State University GeoAnalytical Lab. Mineral major element compositions were measured by EPMA. Clinopyroxene trace element compositions were measured by LA-ICP-MS. Strontium, neodymium, lead, and osmium isotopes were measured by TIMS. Rhenium concentrations were measured by isotope dilution using MC-ICP-MS. Additional detail on the analytical methods as well as estimates of precision and accuracy can be found in the in the supplementary materials.

1.5 RESULTS

1.5.1 Whole Rock analysis

Whole rock major and trace element concentrations are presented in appendix A.1. Xenoliths from Elephant Butte with high modal clinopyroxene (cpx) have high Al_2O_3 and CaO (>3.4 and>2.8 wt.% respectively). We will refer to this group of xenoliths as F-type. A less abundant set of xenoliths from Elephant Butte are coarse grained and have much lower modal cpx (harzburgites and dunites). These xenoliths have lower Al_2O_3 (<2.3 wt.%). The coarse grained, low-modal cpx xenoliths from Elephant Butte will be referred to as R-type. Clinopyroxene-poor lherzolites from Cerro Chato tend to be refractory (Al_2O_3 2.2-3.6 wt. %). The one dunite from Cerro Chato has very low Al_2O_3 (0.82 wt. %). A cpx-rich lherzolite (group-II) from Cerro Chato has high Al_2O_3 (4.5 wt. %).

F-type lherzolites from Elephant Butte display moderate LREE depletion with flat M-HREE (Figure 1.2a). R-type xenoliths are LREE-enriched and have lower HREE concentrations than the F-type xenoliths. Samples from Cerro Chato show much more variation in REE concentration (Figure 1.2b). Group-I lherzolites display concave-up REE patterns with LREE more enriched than the HREE. One group-II xenolith from Cerro Chato was measured for bulk-rock composition. This xenolith (CCO7-1-23) has higher REE concentrations than the group-I xenoliths, and a concave-down REE pattern distinct from the concave-up group-I xenoliths patterns. None of the samples from Cerro Chato display the LREE-depleted patterns characteristic of the F-type lherzolites from Elephant Butte.

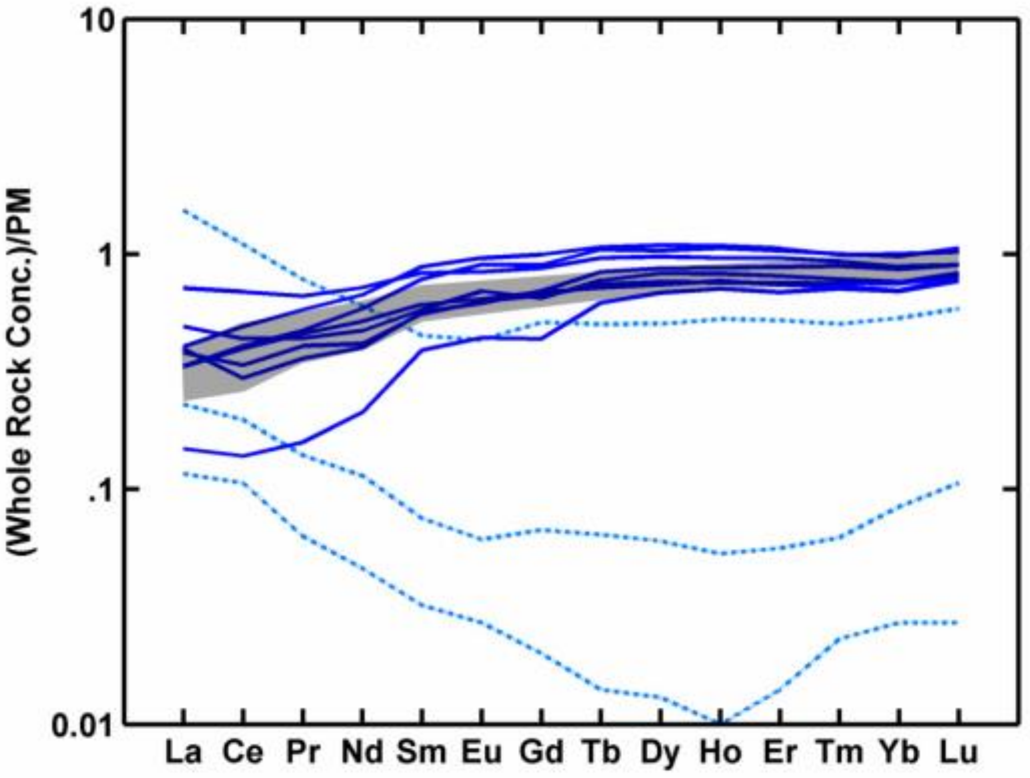

Figure 1.2a Whole-Rock rare earth element concentrations of Elephant Butte xenoliths normalized to primitive mantle.

F-Type xenoliths are shown in solid blue, R-Type xenoliths are dotted blue. Grey field shows estimated range for composition of depleted mantle (values from Workman and Hart (2005) and Salters and Stracke (2004)).

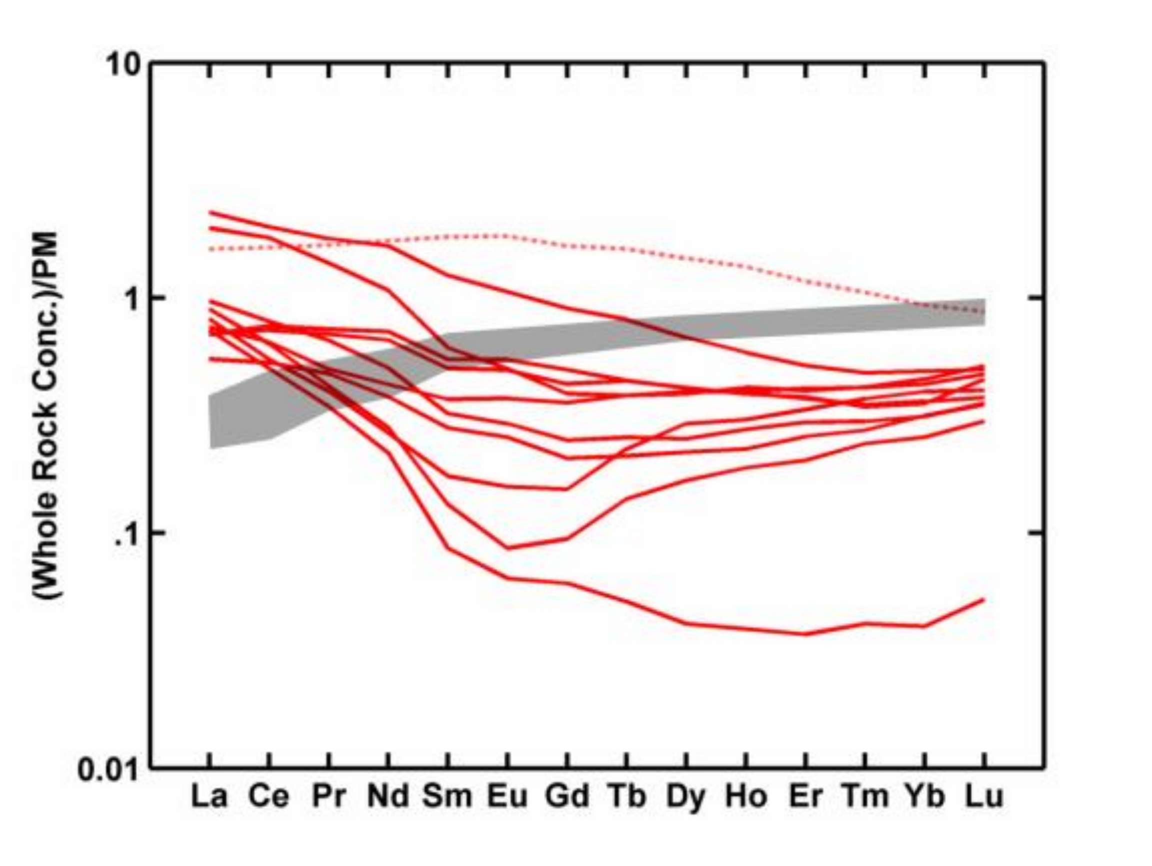

Figure 1.2b Whole-Rock rare earth element concentrations of Cerro Chato xenoliths normalized to primitive mantle.

Group-I xenoliths are shown in solid red, group-II xenoliths are dashed red. Grey field shows estimated range for composition of depleted mantle (values from Workman and Hart (2005) and Salters and Stracke (2004)).

1.5.2 Clinopyroxene, olivine, orthopyroxene, and spinel

Clinopyroxene major and trace element analyses are presented in Appendix A.2. Olivine, orthopyroxene, and spinel major element concentrations are presented in appendix A.3. Variations in clinopyroxene and spinel composition among xenoliths from Cerro Chato and Elephant Butte are consistent with patterns seen from the whole rock data (Figure 1.2c,d). Clinopyroxne and spinel from F-type Elephant Butte xenoliths have low Cr# (molar Cr/(Cr+Al)) (~0.07 and ~0.11, respectively) while R-type xenoliths have high cpx Cr# and spinel Cr# (~0.17 and ~0.36, respectively). Spinel Cr# in Cerro Chato xenoliths ranges from 0.06-0.46, however most samples have Cr# ~0.20. There is a good correlation between cpx Cr# and spinel Cr# among samples from Cerro Chato and Elephant Butte (Figure 1.3).

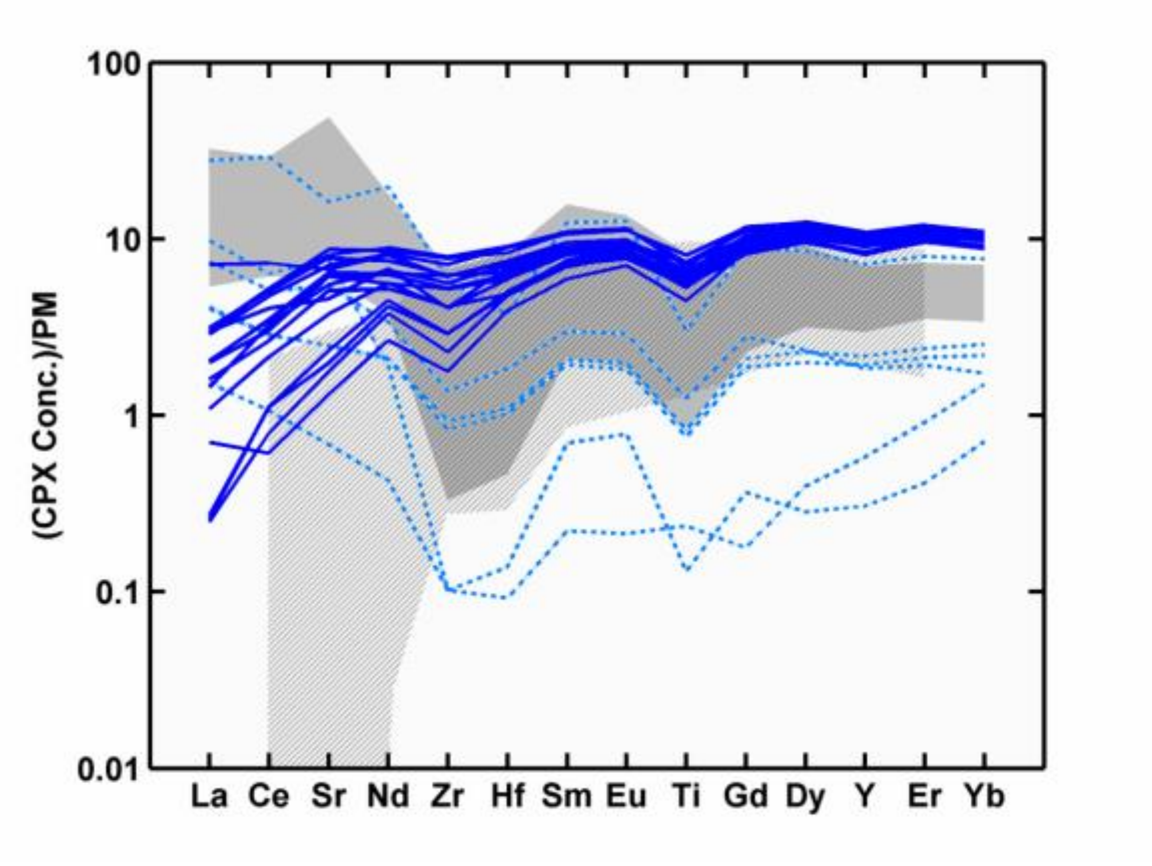

Figure 1.2c Trace element concentrations of clinopyroxenes from Elephant Butte xenoliths normalized to primitive mantle.

F-Type xenoliths are shown in solid blue, R-Type xenoliths are dotted blue. Grey field represents range of Group-I Cerro Chato clinopyroxenes. Diagonal pattern is range of cpx compositions in abyssal peridotites (data from Johnson et al. (1990)). Note the similarity between R-Type Elephant Butte and Group-I Cerro Chato.

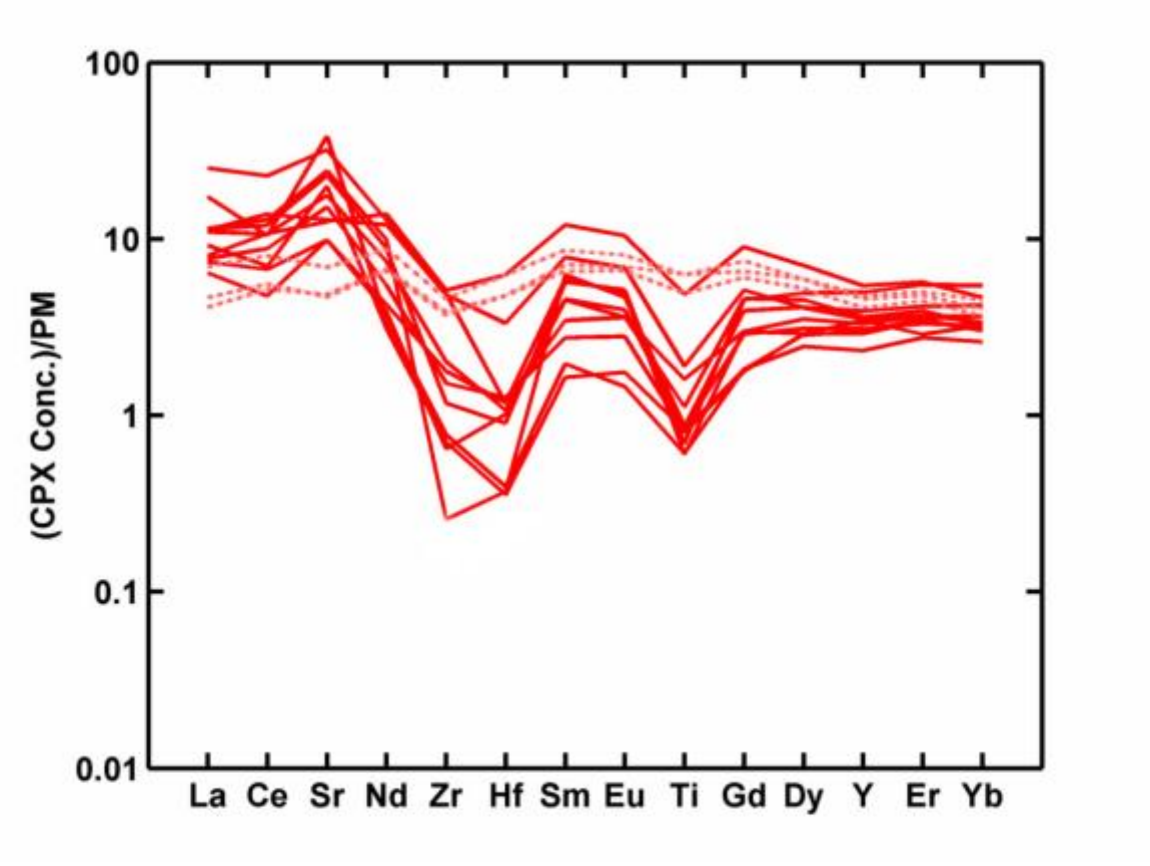

Figure 1.2d Trace element concentrations of clinopyroxenes from Cerro Chato xenoliths normalized to primitive mantle.

Pyroxenes from group-I xenoliths are shown in solid red, group-II xenoliths are dashed red.

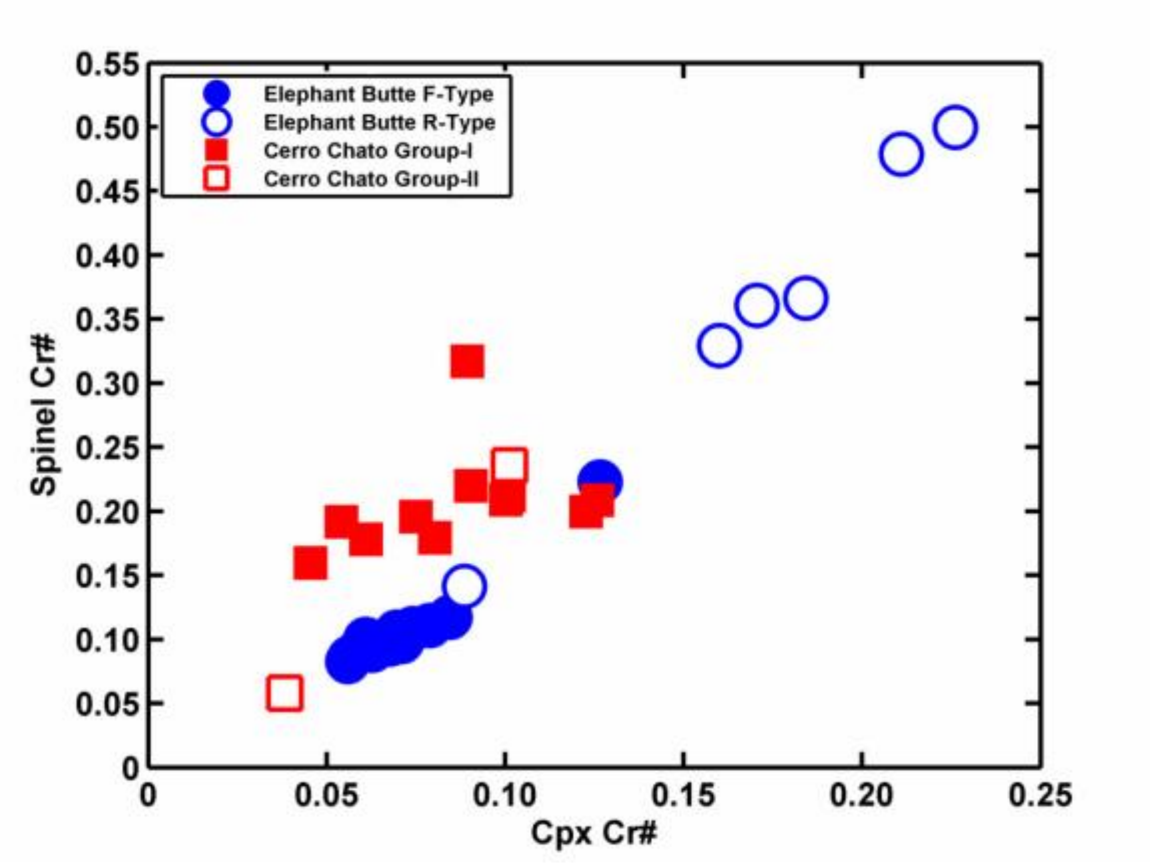

Figure 1.3 Plot of clinopyroxene Cr# versus spinel Cr# for xenoliths from Elephant Butte and Cerro Chato.

Correlation suggests that CPX major element content has not been significantly affected by refertilization.

1.5.3 Isotopic Analyses

Results of isotopic analyses are presented in Table 1.1. F-type Elephant Butte xenoliths have depleted Sr and Nd isotopes (^{87}Sr/^{86}Sr <0.7023 and ε_{Nd} >8) (Figures 1.4a,b). Lead isotopes vary from 18.3-19.1 for ^{206}Pb/^{204}Pb and 37.6-38.5 for ^{208}Pb/^{204}Pb. These xenoliths have ^{187}Os/^{188}Os between 0.124-0.130, except sample BELB 5-8 which has ^{187}Os/^{188}Os = 0.1745 (Figure 1.4c). R-type Elephant Butte xenoliths have more radiogenic ^{87}Sr/^{86}Sr (0.7032-0.7042) and unradiogenic osmium (^{187}Os/^{188}Os 0.114-0.128). Pb isotopes in these xenoliths range from 19.2-19.9 for ^{206}Pb/^{204}Pb and 38.6-39.7 for ^{208}Pb/^{204}Pb. Samples from Cerro Chato are also more enriched than the F-type Elephant Butte xenoliths. ^{87}Sr/^{86}Sr ranges from 0.7029-0.7041, ε_{Nd} ranges from 5.1-7.2 and ^{187}Os/^{188}Os ranges from 0.116-0.126. Lead isotopic compositions for Cerro Chato xenoliths range from 18.8-19.4 for ^{206}Pb/^{204}Pb and 38.6-39.2 for ^{208}Pb/^{204}Pb. Group-I and Group-II xenoliths from Cerro Chato are not isotopically distinct.

Table 1.1 Sr-Nd-Pb-Os isotopic compositions of Rio Grande Rift xenoliths

Elephant Butte

	07EB1.01*	07EB1.05	07EB1.06*	07EB1.09	07EB1.10	07EB1.11*
Re (ppb)	0.246	0.158	0.037			0.046
Os (ppb)	2.95	1.47	2.00		3.91	2.31
^{187}Os/^{188}Os	0.1266	0.1221	0.1171		0.1239	0.1175
^{87}Sr/^{86}Sr	0.701756		0.704251	0.701857		0.704070
^{143}Nd/^{144}Nd	0.514040			0.513223		
εNd	27.3			11.4		
^{206}Pb/^{204}Pb	17.99		19.93	18.22		19.94
^{207}Pb/^{204}Pb	15.39		15.55	15.50		15.57
^{208}Pb/^{204}Pb	37.46		39.62	37.61		39.67

	07EB2.03	07EB4.01*	07EB4.05*	07EB4.06	07EB4.13	07EB4.21*
Re (ppb)	0.078	0.302				0.170
Os (ppb)	0.56	2.21	1.51	1.30	0.98	2.39
^{187}Os/^{188}Os	0.1250	0.1298	0.1272	0.1266	0.1297	0.1253
^{87}Sr/^{86}Sr		0.702518	0.702164			0.701778
^{143}Nd/^{144}Nd		0.513064	0.513168			0.513717
εNd		8.3	10.3			21.2
^{206}Pb/^{204}Pb		18.61	19.06			18.31
^{207}Pb/^{204}Pb		15.53	15.45			15.42
^{208}Pb/^{204}Pb		38.00	38.45			37.88

	07EB4.22	BELB 4-30*	BELB 5-1*	BELB 5-8	BELB 9-8	BELB 9-15
Re (ppb)	0.185	0.062		0.089	0.241	
Os (ppb)	1.91	1.11		0.49	2.70	2.74
^{187}Os/^{188}Os	0.1257	0.1284		0.1745	0.1241	0.1137
^{87}Sr/^{86}Sr		0.703110	0.701877	0.701986	0.702271	
^{143}Nd/^{144}Nd		0.513005	0.513340	0.513273	0.513380	
εNd		7.2	13.7	12.4	14.5	
^{206}Pb/^{204}Pb		19.18	18.42	18.56	18.52	
^{207}Pb/^{204}Pb		15.36	15.44	15.59	15.45	
^{208}Pb/^{204}Pb		38.75	37.69	37.59	37.95	

Osmium isotopic compositions are whole-rock analyses.
Rhenium and osmium concentrations are for whole-rock.
Sr, Nd and Pb were measured from clinopyroxene separates.
* sample-standard bracketing fractionation correction was applied for Pb.
All others were corrected using Pb double-spike

Cerro Chato

	CC07-1-04	CC07-1-06	CC07-1-14	CC07-1-20	CC07-1-22*	CC07-1-23
Re (ppb)			0.015		0.013	
Os (ppb)	1.17		1.75	3.52	3.20	
^{187}Os/^{188}Os	0.1152		0.1259	0.1223	0.1236	
^{87}Sr/^{86}Sr		0.703336		0.704455	0.704024	0.702932
^{143}Nd/^{144}Nd		0.512955		0.512942		0.512914
εNd		6.18		5.93		5.64
^{206}Pb/^{204}Pb		19.11		19.12	18.94	19.23
^{207}Pb/^{204}Pb		15.60		15.61	15.53	15.57
^{208}Pb/^{204}Pb		38.69		38.80	38.50	38.64

	CC07-1-26*	CC07-1-33	CC07-1-35*	CC07-1-51	CC07-2-01	CC07-3-01*
Re (ppb)			0.023	0.012	0.013	0.093
Os (ppb)			3.04	2.09	2.35	1.25
^{187}Os/^{188}Os			0.1259	0.1186	0.1221	0.1210
^{87}Sr/^{86}Sr	0.703837	0.704102	0.703995	0.704036	0.703548	0.703842
^{143}Nd/^{144}Nd	0.512908		0.512899	0.512933	0.512880	0.513007
εNd			5.09	5.75	4.72	7.20
^{206}Pb/^{204}Pb	19.22	19.44	19.42	19.51	19.38	18.84
^{207}Pb/^{204}Pb	15.58	15.70	15.67	15.64	15.61	15.43
^{208}Pb/^{204}Pb	38.79	39.19	39.19	39.08	38.92	38.13

Osmium isotopic compositions are whole-rock analyses.
Rhenium and osmium concentrations are for whole-rock.
Sr, Nd and Pb were measured from clinopyroxene separates.
* sample-standard bracketing fractionation correction was applied for Pb.
All others were corrected using Pb double-spike

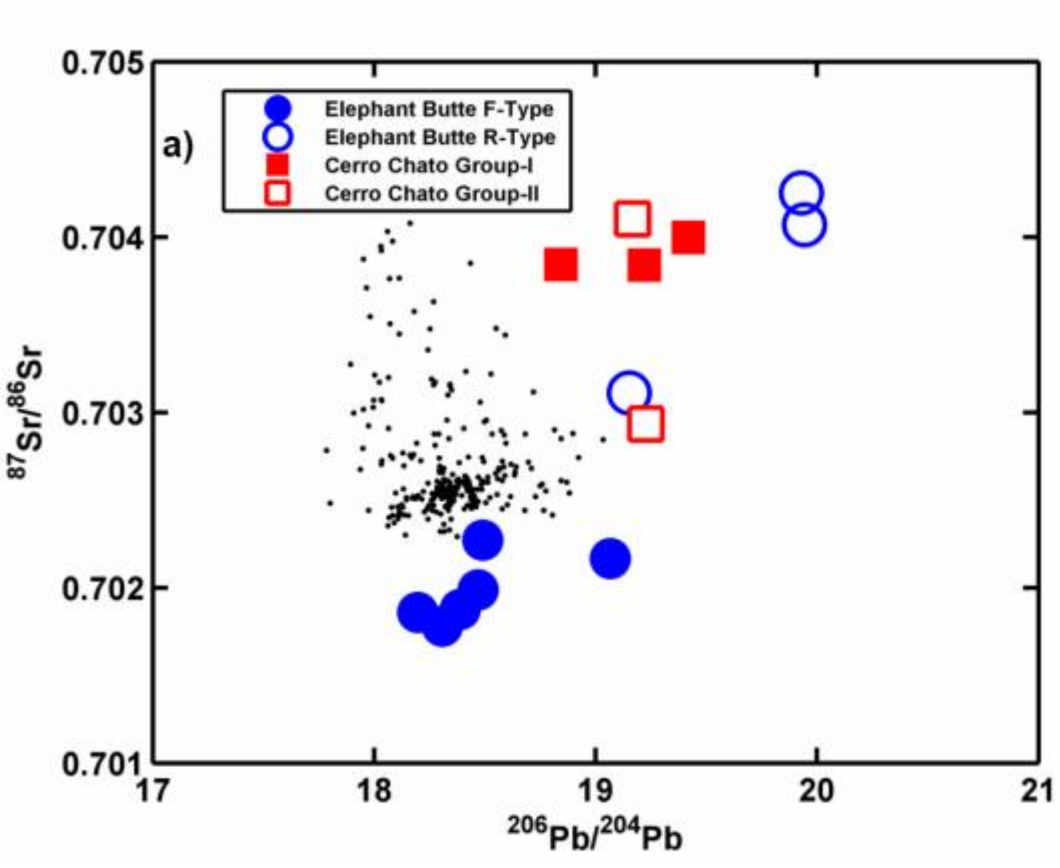

Figure 1.4a ^{87}Sr/^{88}Sr vs. ^{206}Pb/^{204}Pb in cpx separates from Rio Grande Rift and Colorado Plateau xenoliths.

MORB data from http://www.petdb.org/.

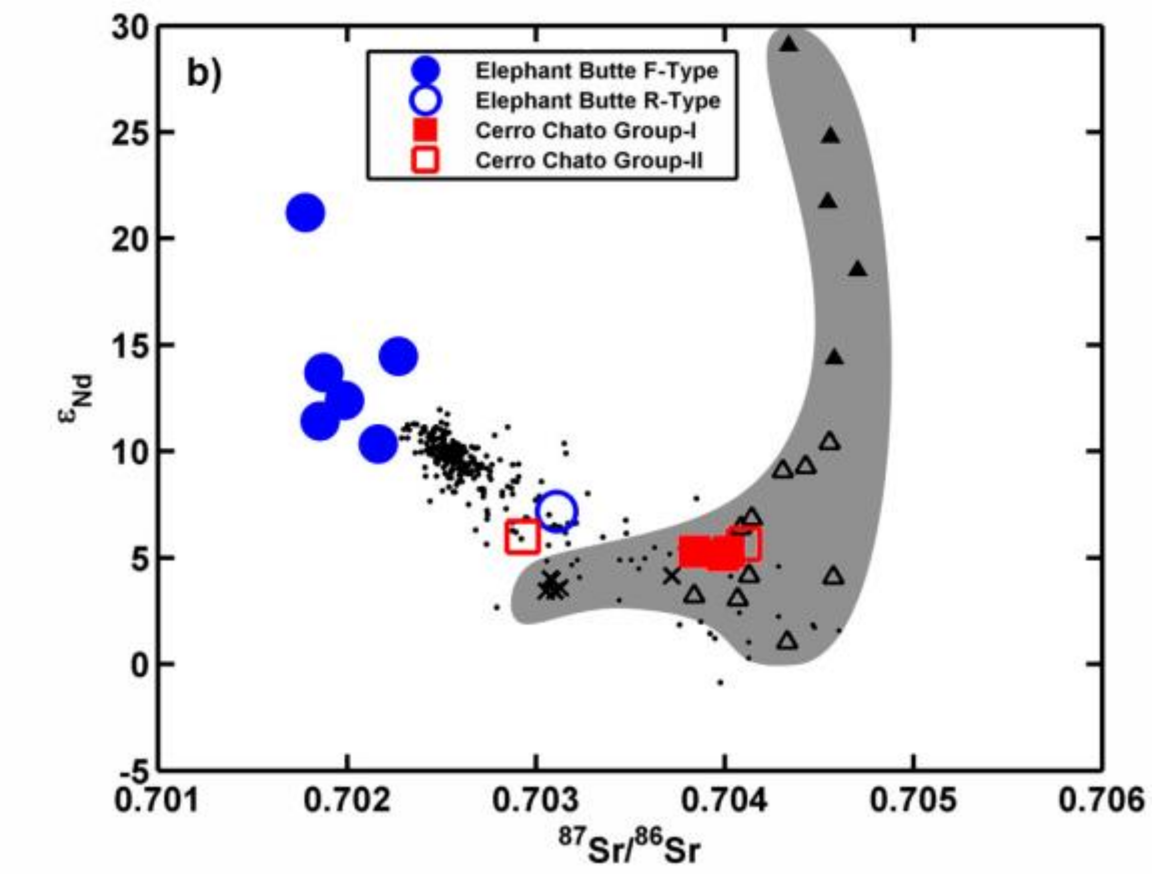

Figure 1.4b ε_{Nd} vs. $^{87}Sr/^{88}Sr$ in cpx separates from Rio Grande Rift and Colorado Plateau xenoliths.

MORB data from http://www.petdb.org/. Black triangles are cpx from the Grand Canyon (data from Alibert (1994)). Open triangles have REE-enriched patterns, filled triangles have concave spoon-shaped REE patterns.

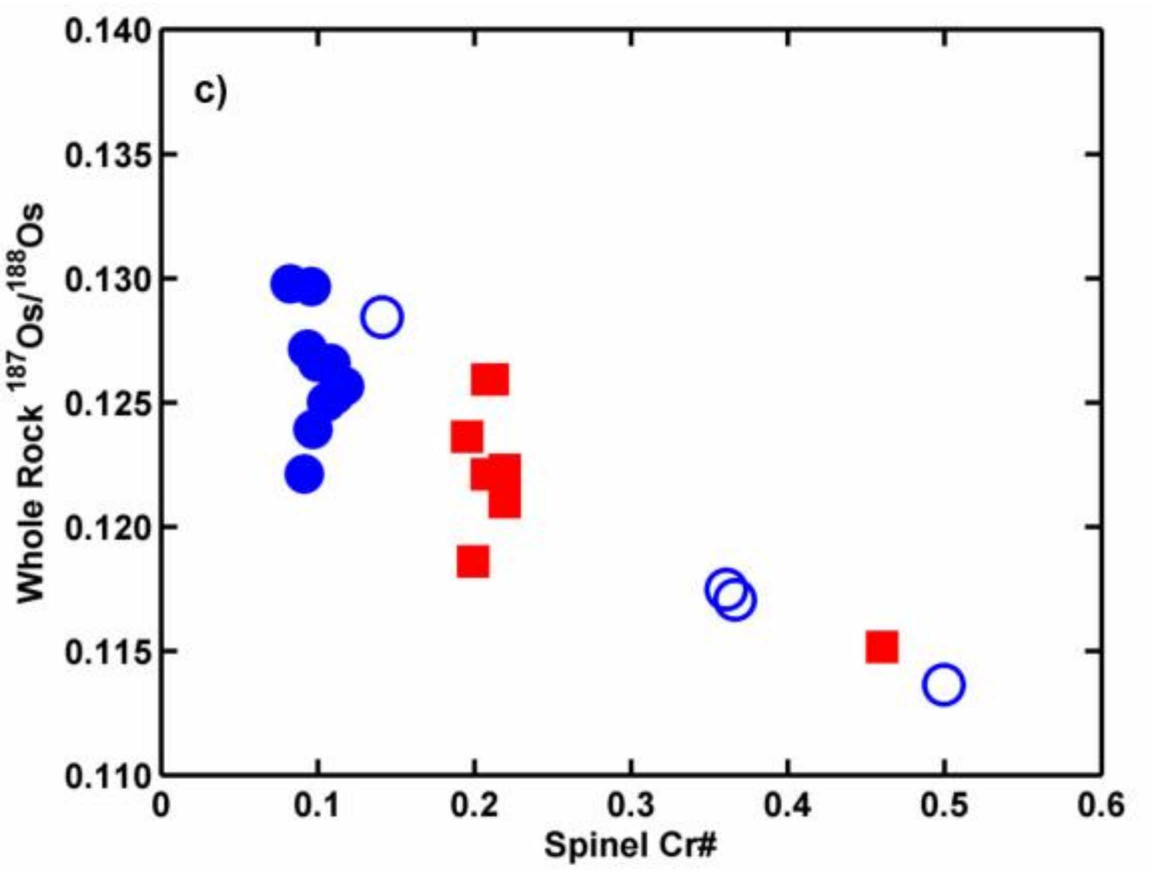

Figure 1.4c Whole rock $^{187}Os/^{188}Os$ vs. Spinel Cr# for RGR and CP xenoliths.

1.5.4 Geothermometry

Xenolith equilibration temperatures were calculated using the two-pyroxene thermometer (T_{BKN}) from Brey and Köhler (1990), which has an estimated error of ±15 °C. We assume a pressure of 15kb for all xenoliths using this thermometer. Equilibration temperatures are presented in Appendix A.4. A ±5kb change in pressure results in a ±10°C difference in T_{BKN}. There is no difference in temperature between core/core or rim/rim measurements on opx-cpx pairs. Temperatures for Elephant Butte and Cerro Chato xenoliths range from 968-1068 °C and 935-1059 °C, respectively. We do not observe any correlations with common fertility indicies (spinel Cr#, Yb in cpx, olivine Fo content) and equilibration temperature. As an example we show in Figure 1.5 spinel Cr# versus equilibration temperature. Unlike Kil and Wendlandt (2004) we do not see a correlation between either textural type or grain size with temperature in samples from Elephant Butte. Group-II xenoliths from Cerro Chato display prominent exsolution lamellae, which suggests they may not be in equilibrium. Therefore, we do not consider temperatures for these xenoliths in the following discussion as the two-pyroxene thermometer is unlikely to be robust.

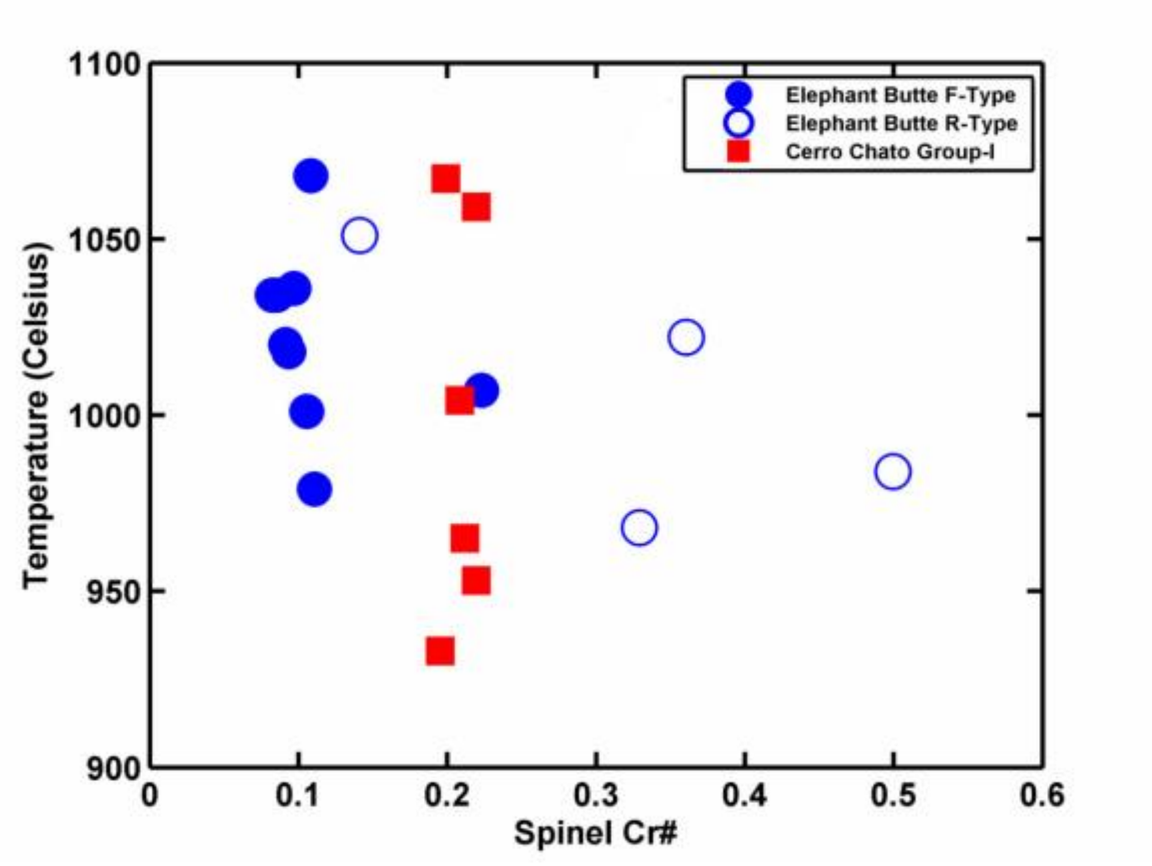

Figure 1.5 Spinel Cr# versus equilibration temperature

Two-pyroxene equilibration temperature after Brey and Köhler (1990). Other common indices of fertility such as Yb in cpx or olivine Fo content also do not correlate with temperature.

1.6 DISCUSSION

1.6.1 Cerro Chato

Mantle xenoliths derived from SCLM typically are depleted in magmaphile elements such as Ca, Al, and Na (McDonough, 1990). Refractory (melt-depleted) xenoliths therefore have low Al_2O_3 contents and high spinel Cr# relative to DMM. Xenoliths derived from Archaean cratons are typically more refractory than those derived from Proterozoic or Phanerozoic SCLM (Menzies, 1990). Therefore, it can be difficult to distinguish young SCLM from depleted mantle based on major-element signatures alone. Xenoliths from the central Colorado Plateau (Navajo volcanic field) have refractory compositions (~1.6±0.9 (1σ) wt. % Al_2O_3) (Smith and Levy, 1976); (Lee et al., 2001b); (Aoki, 1981); (Smith, 2010); (Ehrenberg, 1982). Spinel peridotites from the central Colorado Plateau have more fertile compositions (2.1±1.0 wt. % Al_2O_3) than more deeply derived garnet peridotites (1.4±1.0 wt. % Al_2O_3). Xenoliths from the Basin and Range/Southern Rio Grande rift, on the other hand, are typically more fertile (~3.2±1.2 (1σ) wt. % Al_2O_3) than CP xenoliths (Beard and Glazner, 1995); (Ehrenberg, 1982); (Frey and Prinz, 1978); (Lee et al., 2001a); (Kil and Wendlandt, 2007). Xenoliths (spinel peridotites) from the Grand Canyon (western margin of CP) have intermediate compositions (2.1±0.6 (1σ) wt. % Al_2O_3) (Smith et al., 1999). Group-I xenoliths from Cerro Chato (eastern margin of CP) have similar fertility (2.5±0.7 (1σ) wt. % Al_2O_3) to spinel peridotites from the central CP and western CP margin but are more refractory than Basin and Range xenoliths and less refractory than garnet-bearing xenoliths from the central CP. The fertility of the Cerro Chato xenoliths is far from that which is estimated for depleted mantle (~4.0 wt. % Al_2O_3 and spinel Cr# ~0.11) (Workman and Hart, 2005).

LREE enrichment is another common feature of SCLM that has been metasomatised by fluid or melt components (Kempton, 1987); (Frey and Prinz, 1978). This, however, is not a ubiquitous feature of SCLM (Menzies et al., 1983). For example, although garnet peridotites from the central Colorado Plateau show LREE-enrichment, spinel peridotites from the central Colorado Plateau are LREE-depleted (Alibert, 1994); (Roden and Shimizu, 1993) (Figure 1.6). Xenoliths from the Grand Canyon, CP margin, display both spoon-shaped and LREE-enriched patterns (Figure 1.6), (Alibert, 1994). The spoon-shaped patterns are similar to patterns observed in xenoliths from the Honolulu volcanic vents that Sen et al. (1993) attribute to varying degrees of metasomatic enrichment and equilibration. The Grand Canyon xenoliths may, therefore, reflect different degrees of equilibration with metasomatic melts or fluids. Xenoliths from Cerro Chato display variable LREE-enrichment in both cpx and whole-rock (Figs. 1.2b, 1.6). The REE patterns in group-I xenoliths from Cerro Chato closely overlap with LREE-enriched patterns observed in Grand Canyon xenoliths (Figure 1.6). The LREE-MREE enriched patterns are similar to garnet peridotites from the Navajo V.F., and dissimilar to DMM.

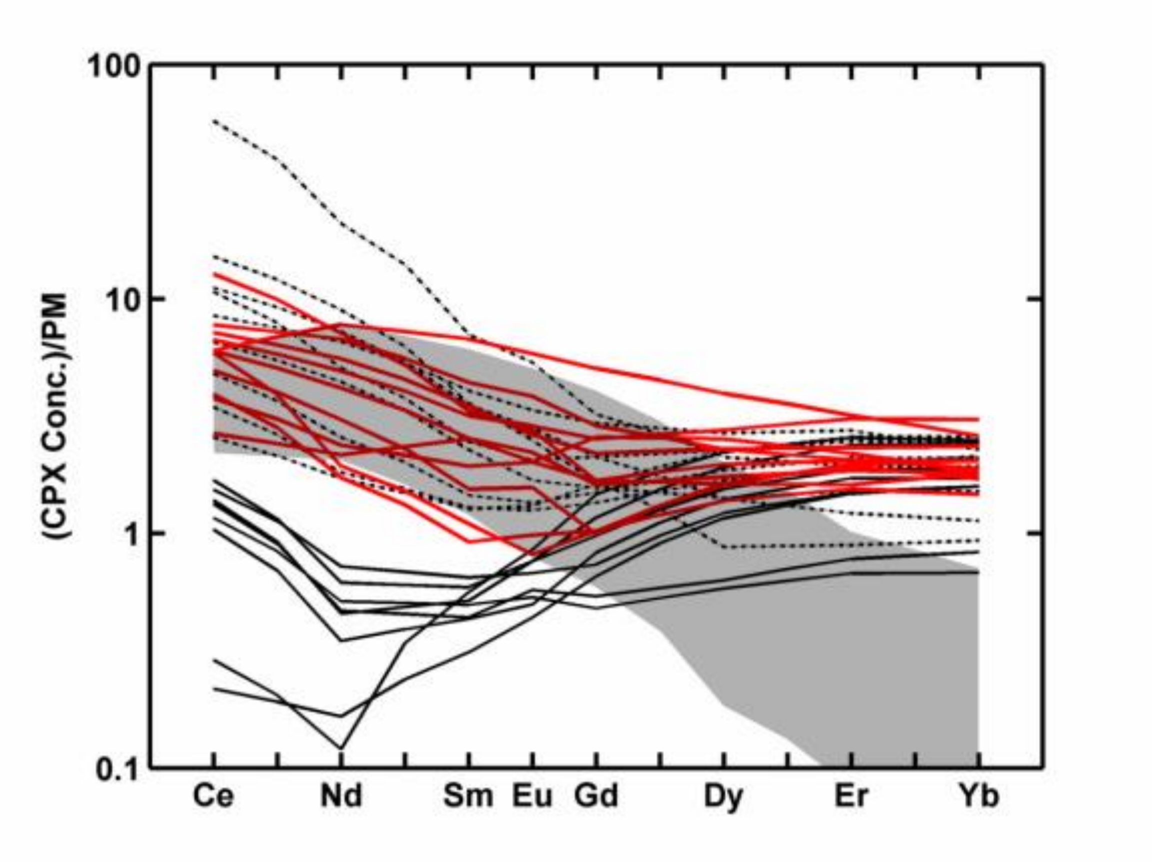

Figure 1.6 Rare earth element patterns for group-I xenoliths from Cerro Chato and other Colorado Plateau xenoliths.

Cerro Chato group-I xenoliths are shown in red. Grey field, range for garnet-bearing xenoliths from the central Colorado Plateau (The Thumb). Solid black lines are spoon-shaped REE patterns in Grand Canyon xenoliths. Dashed black lines are REE-enriched patterns from the Grand Canyon. (Grand Canyon and The Thumb data from Alibert (1994)).

In addition to similarities between REE patterns, the isotopic compositions of the Cerro Chato xenoliths are similar to Colorado Plateau xenoliths and unlike DMM. The Sr and Nd isotopic compositions of the Cerro Chato xenoliths overlap with xenoliths from the Grand Canyon, and are slightly more enriched than xenoliths from the central Plateau (Alibert, 1994); (Riter, 1999), (Figure 1.4b). In contrast, xenoliths from the Basin and Range province have a wide range of isotopic compositions. They trend from depleted Sr and Nd isotopes, similar to depleted mantle, to enriched Sr and Nd isotopes (Galer and Onions, 1989); (Beard and Glazner, 1995); (Mukasa and Wilshire, 1997); (Luffi et al., 2009). Xenoliths from the southern Rio Grande rift have depleted Sr and Nd isotopes, which are unlike the Cerro Chato xenoliths (Roden et al., 1988). The enriched isotopes in B&R xenoliths may reflect metasomatism from the Farallon slab or reflect the persistence of portions of the Proterozoic SCLM within the Basin and Range (Luffi et al., 2009); (Lee et al., 2000). The Pb isotopic compositions of Cerro Chato xenoliths are more radiogenic than the range for MORB (Figure 1.4a). The isotopic compositions of the Cerro Chato xenoliths closely overlap with xenoliths from the Colorado Plateau and are distinct from southern RGR xenoliths and estimates for DMM.

Cerro Chato xenoliths have relatively unradiogenic Os isotopes and low Re concentrations, which likely reflects ancient melt extraction and derivation from SCLM. The range in Os isotopes observed in Cerro Chato xenoliths ($^{187}Os/^{188}Os$ from 0.116-0.126) overlap with the range observed in SCLM xenoliths. There is, however overlap between the compositions of SCLM xenoliths and abyssal peridotites, although SCLM xenoliths trend towards more unradiogenic compositions (Meisel et al., 2001). Thus, the significance of the Os isotopic compositions of most of the Cerro Chato xenoliths is somewhat ambiguous. However, osmium model ages suggest that melt extraction in the Cerro Chato xenoliths occurred as early as ~2 Ga. This is similar to the age of the crust in the region (Bennett and Depaolo, 1987). During melt extraction rhenium is incompatible and becomes depleted in the mantle residue. A total rhenium depletion model age (T_{RD}, after Shirey and Walker (1998)) assumes complete loss of rhenium, thus locking the $^{187}Os/^{188}Os$ in the residue at the time of melt extraction. The T_{RD} for the most unradiogenic (and most refractory) Cerro Chato xenolith is 1.98 Ga. A group of garnet-harzburgites from The Thumb (central CP) are, on average, less radiogenic than most of the Cerro Chato xenoliths (Figure 1.7). However, the most unradiogenic sample yields a similar T_{RD} of 1.75 Ga (Lee et al., 2001a). Cerro Chato xenoliths have melt depletion ages similar to other Colorado Plateau xenoliths and to the timing of crust formation in the region.

There is some degree of vertical variation in fertility present in the Colorado Plateau lithosphere. Spinel peridotites from throughout the CP and CP margin are more fertile than garnet peridotites from the central CP. One possible explanation for this is that the lithosphere is chemically stratified due to refertilization of the upper lithospheric mantle. The presence of LREE-enriched patterns in xenoliths from Cerro Chato and the Grand Canyon is consistent with refertilization (Alibert, 1994). However, spinel-peridotites from the central Colorado Plateau do not display LREE-enrichment, but instead show LREE-depletion (Roden and Shimizu, 1993; Smith, pers. comm.). This is inconsistent with the hypothesis that refertilization is responsible for greater fertility of spinel-bearing xenoliths from the central Colorado Plateau.

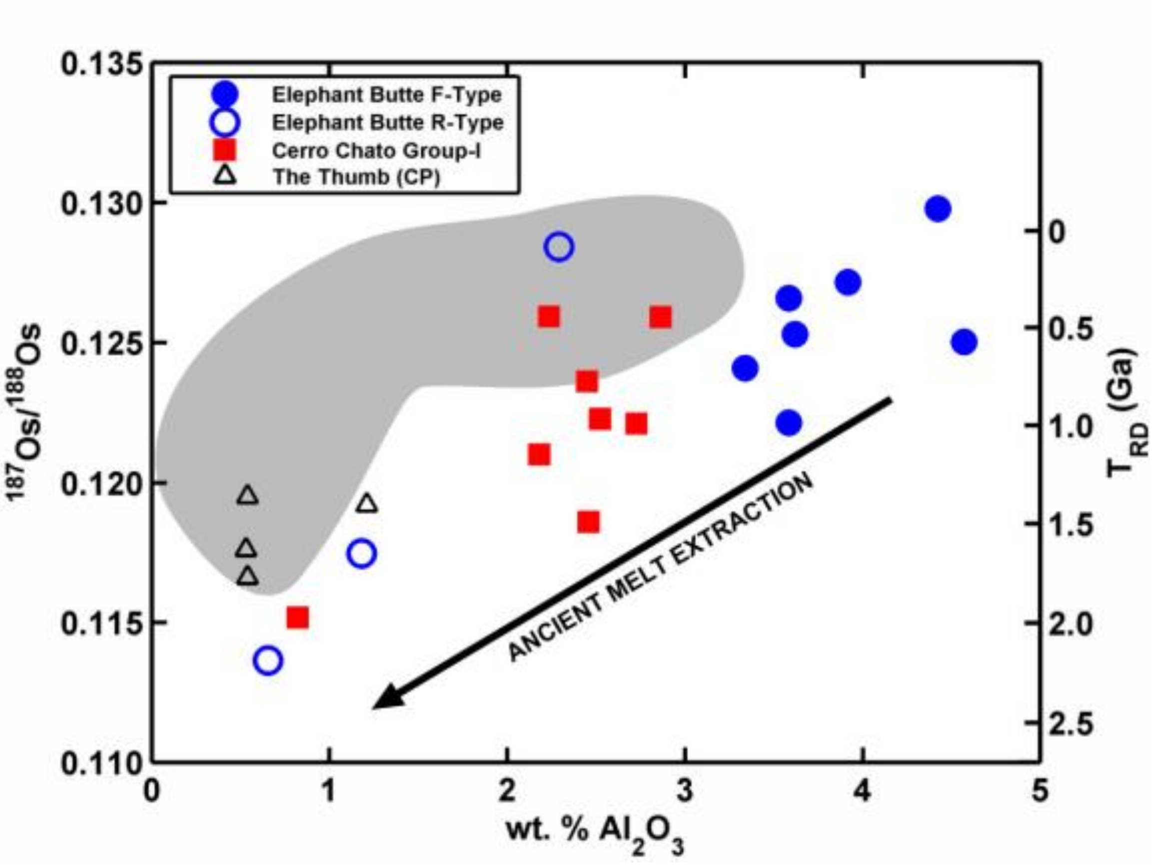

Figure 1.7 Plot of $^{187}Os/^{188}Os$ vs. bulk-rock wt. % Al_2O_3.

Samples from Cerro Chato and R-type samples from Elephant Butte are more refractory and have less radiogenic Os isotopes than F-Type Elephant Butte xenoliths. These are common characteristics of Proterozoic SCLM and are suggestive of ancient melt depletion. Grey field is range of residual abyssal peridotites. Data from Liu et al. (2008), Brandon et al. (2000), and Harvey et al (2006). Black triangles are garnet-bearing xenoliths from The Thumb (central Colorado Plateau) (data from Lee et al. (2001a)). TRD ages are calculated using $^{187}Re/^{188}Os_{CHON}$ of 0.42 and $^{187}Os/^{188}Os_{CHON}$ of 0.129.

An alternative hypothesis for lower fertility in garnet peridotites from the Colorado Plateau is that garnet peridotites have experienced higher degrees of melt depletion than spinel peridotites from the same area. Decompression melting of dry peridotite would generally result in greater fertility at depth, which is not observed in the CP. However, flux melting of the lithospheric mantle could produce the observed variations with depth. There is abundant evidence for the hydration of Colorado Plateau lithosphere in mantle xenoliths (i.e. the presence of hydrous minerals) (Smith et al., 1999). Hydration of the lithosphere would lower the solidus temperature of the peridotitic mantle. In this case, mantle at greater depths (higher temperatures and a large difference between wet and dry solidus) would experience higher degrees of melt extraction than shallow mantle. This is consistent with what is observed in xenoliths from the central Colorado Plateau where garnet peridotites are more refractory than spinel-peridotites.

Group-I xenoliths from Cerro Chato have refractory major element compositions, LREE-enriched trace element patterns, Sr and Nd isotopes outside the range for DMM, and Os depletion ages similar to the age of the crust and other portions of the Colorado Plateau lithosphere. These characteristics are shared with other Colorado Plateau xenoliths derived from similar depths. Therefore we conclude that group-I Cerro Chato xenoliths are derived from Proterozoic SCLM. Vertical variations in fertility within the Colorado Plateau may be explained by flux melting of the lithosphere, which resulted in garnet peridotites experiencing higher degrees of melt depletion than spinel peridotites.

The group-II peridotites from Cerro Chato have geochemical signatures that distinguish them from group-I xenoliths. They have high modal abundances of cpx (>35%) and high cpx Al_2O_3 (> 6.6 wt. %). Additionally they have low olivine Mg# (<86 compared to >90 for group-I xenoliths). One whole-rock trace element pattern shows a concave-down shape. Clinopyroxene trace element patterns lack the strong LREE enrichment and negative HFSE anomalies relative to REE that are ubiquitous among group-I xenoliths. These characteristics suggest that they have a different origin than the group-I xenoliths.

One possible origin for the group-II xenoliths at Cerro Chato is that they are cumulates from melts passing through the lithosphere. The group-II Cerro Chato xenoliths have poikilitic textures and variable modal mineral proportions, characteristics that have been attributed to cumulate origins (Best, 1970); (Best, 1975); (Irving, 1974). The isotopic composition of the host lava ($^{87}Sr/^{86}Sr$ 0.70338 and $^{143}Nd/^{144}Nd$ 0.51290) (Rowe, pers. comm.) is similar to the group-II peridotites (Figures 1.4a,b). Wilkinson (1975) argues that the high Al contents in cpx and low Mg# in olivine, which are common among group-II xenoliths worldwide, are consistent with those minerals precipitating from alkali basalts at 15-20kb. Models using pMELTS (Ghiorso et al., 2002) also show that a magma with the composition of the Cerro Chato host lava is capable of precipitating olivine and clinopyroxene at pressures of 10-15kb with similar Mg# (~85) and Al_2O_3 (>6.0 wt. %) contents to the group-II xenoliths from Cerro Chato. Using trace element partition coefficients (Hart and Dunn, 1993) we calculate melts that would be in equilibrium with the clinopyroxene from group-II xenoliths. These are broadly similar to the Cerro Chato lava (similar La/Yb), although the cpx yield theoretical melts with higher La/Sm and slightly lower overall concentrations of incompatible trace elements.

An alternative origin for the Group-II xenoliths is that they are the result of high degrees of melt-rock interaction within the lithosphere. Pyroxene-rich xenoliths are sometimes interpreted to represent dikes where basaltic magmas passed through the lithosphere (Wilshire and Shervais, 1975); (Irving, 1980). Group-II xenoliths often occur as composites where pyroxene-rich veins cross cut depleted peridotites. Additionally there are reaction zones that are present in the depleted peridotites perpendicular to the veining. None of the group-II xenoliths from Cerro Chato display these relationships, thus it is less likely that they represent dikes. We conclude that the group-II xenoliths are likely cumulates from an alkali-basalt that is similar in composition to the host lava for the Cerro Chato xenoliths.

1.6.2 Nature of the Elephant Butte xenoliths

1.6.2.1 R-type xenoliths

The refractory group (R-type) of xenoliths from Elephant Butte have major element compositions that are indicative of high degrees of melt extraction and are similar to xenoliths from Cerro Chato and the rest of the Colorado Plateau. Clinopyroxene Cr# and spinel Cr#, which both increase with higher degrees of melt extraction (Dick and Bullen, 1984), positively correlate (Figure 1.3) and are higher than those in F-type xenoliths. These samples have low modal abundance of cpx, which is consumed during partial melting of peridotite (Jaques and Green, 1980). On average the R-type xenoliths are more refractory (<2.3 whole-rock wt. % Al_2O_3, spinel Cr# 0.36±0.12 (1σ)) than the Cerro Chato xenoliths (Figure 1.8), and very different from depleted mantle.

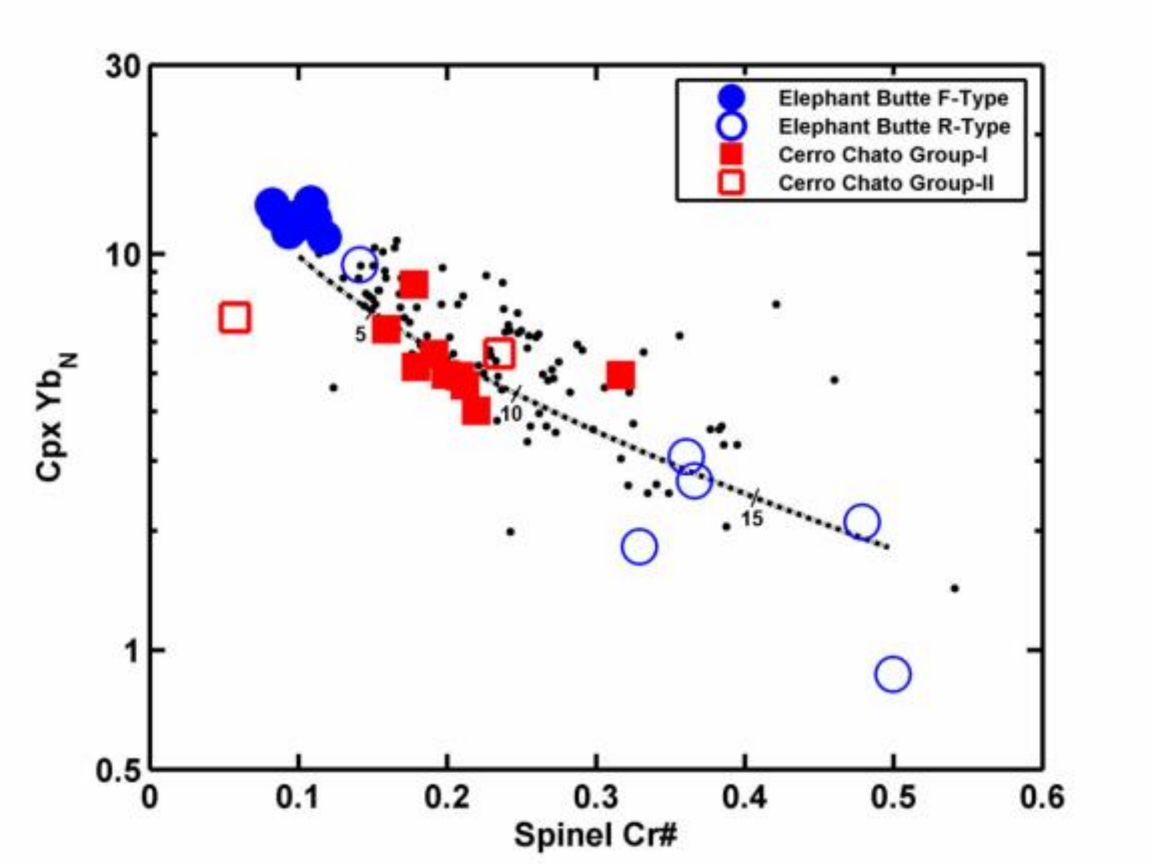

Figure 1.8 Cpx Yb normalized to chondrite vs. spinel Cr#.

Low Cr# [molar Cr/(Cr+Al)]and high Yb are features of xenoliths which have not undergone significant melt depletion. Blacked dashed line represents a melting model (entirely within the spinel stability field) after Hellebrand et al. (2001) where degree of fractional melting is a function of spinel Cr# and Yb content is modeled after Johnson et al., 1990. Tick marks denote percentage of fractional melting. Black triangles are residual abyssal peridotites (data from Brunelli et al. (2006), Hellebrand et al. (2002), Hellebrand et al. (2005), Johnson et al. (1990), and Seyler et al. (2007).

The R-type xenoliths have trace element patterns that resemble those of the xenoliths from Cerro Chato and the Colorado Plateau. The whole-rock REE patterns for R-type xenoliths are concave-up with LREE enrichment. Clinopyroxene trace element patterns of the R-type xenoliths resemble those of the group-I xenoliths from Cerro Chato (Figure 1.2c). The REE concentrations in cpx and whole-rock in the R-type xenoliths are lower than the group-I Cerro Chato xenoliths, which may be due to higher degrees of melt extraction experienced by the R-type xenoliths compared to the Cerro Chato xenoliths.

Strontium, Nd, and Pb isotopes plot close to xenoliths from Cerro Chato and the Colorado Plateau, and deviate considerably from DMM (Figure 1.4a,b). The R-type xenoliths, on average, have unradiogenic Os isotopic compositions and low rhenium concentrations. The range in Os isotopic composition and rhenium concentration is similar to the garnet-bearing xenoliths from The Thumb, central CP (Lee et al., 2000). The unradiogenic osmium isotopic compositions suggest that melt extraction occurred during the Proterozoic (Figure 1.4c, Figure 1.7). The most refractory R-type xenolith has a T_{RD} of ~2.2 Ga.

Refractory major element compositions, enriched Sr, Nd, and Pb isotopes, unradiogenic Os isotopes, and enriched trace element patterns found in R-type xenoliths are similar to Cerro Chato and Colorado Plateau xenoliths. They are unlike depleted mantle. We conclude that the R-type xenoliths from Elephant Butte are derived from Proterozoic lithospheric mantle.

1.6.2.2 F-type xenoliths

The F-type xenoliths have fertile major element compositions (3.9 ± 0.5 wt.% Al_2O_3 in whole-rock) similar to estimates for the composition of the depleted mantle (4.0-4.3 wt. % Al_2O_3) (Salters and Stracke, 2004; Workman and Hart, 2005). They have higher modal abundances of cpx (~16 ± 2%) than Cerro Chato and R-type xenoliths (on average <10% cpx). This suggests that the F-type xenoliths have experienced less melt extraction. F-type xenoliths have low spinel Cr# and high Yb content in cpx (Figure 1.8), which also indicate low-degrees of melt extraction (Hellebrand et al., 2001). An alternative hypothesis to explain the fertile composition of these xenoliths is that they have been refertilized. However the LREE-depleted trace element patterns and lack of evidence for metasomatism argue against this hypothesis. The high degree of fertility in the F-type xenoliths is in sharp contrast to the Cerro Chato, Colorado Plateau, and R-type xenoliths.

The LREE depletions coupled with flat M-HREE seen in cpx and whole rock (Figures 1.2 a,c) are consistent with a source similar to that from which MORB are derived Workman and Hart (2005) and Salters and Stracke (2004). Clinopyroxenes from abyssal peridotites also display LREE depletion similar to that seen in cpx from F-type Elephant Butte xenoliths (Niu, 2004; Johnson et al., 1990) (Figure 1.2c). The degree to which the LREE and MREE are depleted in cpx is commonly less in F-type xenoliths relative to abyssal peridotites. This is likely due to lower degrees of prior melt extraction in the F-type xenoliths than in APs. F-type xenoliths lack the LREE-enrichment that is characteristic of most Colorado Plateau xenoliths.

Osmium isotopic compositions are variable, with $^{187}Os/^{188}Os$ ranging from 0.1221-0.1745. Sample BELB 5-8 has a highly radiogenic Os isotopic composition

($^{187}Os/^{188}Os$ of 0.1745). Although sample BELB 5-8 has a low loss on ignition (0.05%), it does appear to be weathered (iddingsite formed on olivine). Sample BELB 5-8 has a low Os concentration (0.49 ppb), and thus is susceptible to contamination from crustally-derived Os. A large portion of the PGE and Re whole-rock budget in peridotites is often hosted in sulfide phases and alloys (Handler and Bennett, 1999), which are prone to sub-aerial alteration (Lorand, 1990). Their removal may result in lower bulk-rock Os concentrations (Handler and Bennett, 1999). This may explain the low Os concentration of BELB 5-8. Surficial contamination could have resulted in an elevated $^{187}Os/^{188}Os$ (average upper continental crust has a $^{187}Os/^{188}Os$ of ~ 2.0 (Esser and Turekian, 1993)). The Os isotopic composition of sample BELB 5-8 appears to have been altered by secondary processes and thus we exclude it from the remaining discussion.

Excluding BELB 5-8, the range of $^{187}Os/^{188}Os$ in F-type xenoliths is 0.1221-0.1298. This is similar to the range reported for abyssal peridotites and depleted-MORB mantle (Snow and Reisberg, 1995; Standish et al., 2002). The $^{187}Os/^{188}Os$ for F-type xenoliths coincides most with more fertile (>2.0 wt. % Al_2O_3) abyssal peridotites (Figure 1.7). There is no correlation present between indicators of the degree of melt depletion and Os isotopic composition amongst the F-type xenoliths.

The major element, trace element, and osmium isotopic compositions of F-type xenoliths are similar to those of DMM. We interpret these xenoliths to have derived from recently emplaced asthenospheric mantle at the base of the SCLM. This source is now part of the physical lithosphere (as required by the ~1000°C equilibration temperature) but is chemically distinct from the pre-existing Proterozoic SCLM.

1.6.3 Extreme isotopic depletion in Elephant Butte F-type xenoliths

Many recent studies demonstrate that the earth's upper convecting mantle is isotopically heterogeneous. At one end are basalts, abyssal peridotites, and mantle xenoliths with very depleted isotopic signatures (high ε_{Nd} and ε_{Hf}, unradiogenic Sr and Os). Workman and Hart (2005) report some MORB with unradiogenic Sr ($^{87}Sr/^{86}Sr$ ~0.7022) and high ε_{Nd} (~12). Abyssal peridotites and OIB xenoliths are useful for studying these heterogeneities because, unlike basalts, they allow for direct sampling of the upper mantle. The existence of abyssal peridotites from the Gakkel ridge with very depleted $^{187}Os/^{188}Os$ (model ages up to 2 Ga) led Liu et al. (2008) to propose that long-term preservation of refractory domains in the convecting mantle is possible. Extremely radiogenic Hf and Nd (ε_{Hf} up to 104 and ε_{Nd} 20.5, respectively) in cpx from abyssal peridotites from the Gakkel ridge also provide evidence for the presence of extremely depleted mantle domains (Stracke et al., 2011). On the island of O'ahu, Hawaiian Islands, Bizimis et al. (2007) report xenoliths with $^{187}Os/^{188}Os$ as low as 0.1138 and radiogenic Hf isotopes (ε_{Hf} up to 114). Ishikawa et al. (2011) describe a similar refractory domain, which is sampled by mantle xenoliths from the Solomon Islands, Ontong Java plateau. These studies demonstrate the existence of isotopically depleted domains within the convecting mantle that have managed to escape homogenization.

F-type xenoliths from Elephant Butte are sampling mantle that was recently part of the convecting mantle (see previous section). These xenoliths have Sr and Nd isotopes that trend from average DMM towards a more depleted source (lower $^{87}Sr/^{86}Sr$ and higher ε_{Nd}) (Figure 1.4 a,b). We report xenoliths with $^{87}Sr/^{86}Sr$ as low as 0.7018 and ε_{Nd} as high as 21. Some xenoliths from Kilbourne Hole (southern RGR) also have low $^{87}Sr/^{86}Sr$ (< 0.7020) (Roden et al., 1988). These observations are consistent with previous studies that demonstrate the existence of isotopically depleted domains within the convecting mantle.

1.6.4 Xenolith extraction depth

The extraction depth of the Elephant Butte and Cerro Chato xenoliths can be estimated by calculating a local geothermal gradient based on heat flow estimates for the region, accounting for heat generated in the crust from the decay of radioactive elements, and assuming a quasi-steady state with respect to heat flow. The surface heat flows are ~95 mW/m^2 and ~83m W/m^2 for the Elephant Butte and Cerro Chato regions, respectively (Reiter et al., 1986). The thickness of the crust at Elephant Butte is ~29 km and at Cerro Chato it is ~39 km (Keller et al., 1990). We assume the thermal conductivity of the crust and mantle to be 2.7 W/(m·K) and 4.0 W/(m·K) respectively (Turcotte and Schubert, 2002). We also assume the density of the crust to be 2800 kg/m^3 and the mantle to be 3250 kg/m^3. The concentrations of heat producing elements in the crust was modeled after Rudnick and Fountain (1995). If surface heat flow has not equilibrated with high temperatures recently emplaced at shallow depth (e.g. due to lithosphere removal) then our model over-estimates extraction depth.

Kil and Wendlandt (2004) calculate a xenolith extraction depth between 27 and 32km for Elephant Butte xenoliths. However, their estimate neglects crustal heat input. When heat input from the decay of radioactive isotopes within the crust is included in modeling the geothermal gradient the estimated extraction depth increases by ~10km. Figure 1.9 shows our model for the geothermal gradients at Elephant Butte and Cerro Chato. The error of ±15°C in the T_{BKN} geothermometer results in a ±1.5 km error in depth estimate. We estimate that xenoliths from Elephant Butte derived from 39-47 km and xenoliths from Cerro Chato derived from 50-60 km depth. These model depths are consistent with the presence of spinel and the absence of garnet in the xenoliths. Equilibration temperatures for F-type (recently emplaced asthenosphere) and R-type (Proterozoic SCLM) xenoliths overlap, suggesting that the xenoliths from Elephant Butte are sampling the boundary between these two mantle provinces, which lies at ~45km depth.

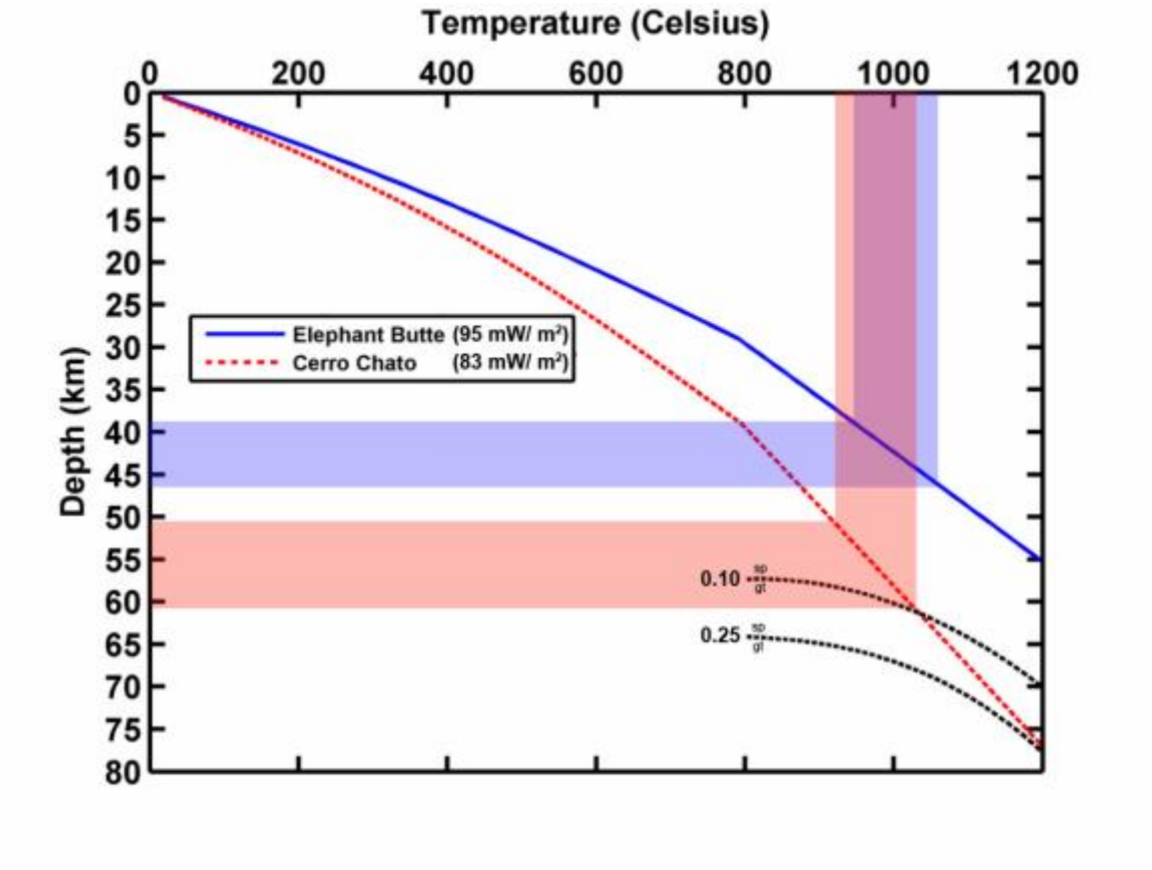

Figure 1.9 Model for geothermal gradients beneath Cerro Chato and Elephant Butte

The model includes heat input from the decay of radioactive elements within the crust. Range in estimated extraction depth is shown for Elephant Butte (blue) and Cerro Chato (red). Estimates for the spinel-garnet transition at different spinel Cr# are shown as dotted black lines after O'Neill (1981) and Klemme and O'Neill (2000). Average spinel Cr# for F-type Elephant Butte xenoliths is ~0.10 and for Cerro Chato xenoliths is ~0.25.

1.6.5 Removal of the lithosphere beneath the central RGR

Our model shows that at the time that the asthenospheric source for F-type xenoliths was emplaced, the base of the lithosphere was at ~45km depth. For asthenospheric mantle to extend to such shallow levels, considerable thinning or removal of the lithosphere must have occurred. Removal of the entire lithosphere has not occurred, because portions of the pre-existing Proterozoic SCLM are sampled by the R-type xenoliths at Elephant Butte. Riter and Smith (1996) demonstrate that at 25 Ma the Colorado Plateau had a thickness of at least 140km. Additionally, Song and Helmberger (2007) and Keller et al., (1979) estimate the Western Great Plains lithosphere to have a thickness of 100-150 km. Thus, prior to rifting it is likely that the Rio Grande rift had a lithosphere thickness on the order of 100 km. Passive rifting is thought to only have resulted in ~25% extension (Cather et al., 1994). The nearby Colorado Plateau and Great Plains provinces have crustal thicknesses on the order of 40-50 km (Wilson et al., 2005). Rio Grande rift crustal thicknesses are on the order of ~30 km. This is also consistent with only moderate (25-40%) extension (Keller et al., 1979; Zandt et al., 1995). Extension of this magnitude would result in lithosphere thickness of 60-75 km. This is inconsistent with our observation of recently emplaced asthenosphere as shallow as 40 km. These observations require that a portion of the lithosphere has been removed and subsequently replaced by asthenospheric mantle. This emplaced asthenosphere subsequently thermally equilibrated at the base of the SCLM and is the source of the F-type xenoliths found at Elephant Butte.

Mechanical delamination is one possible mechanism for lithosphere removal. Delamination models require a mechanical discontinuity at which a portion of the lithosphere decouples (Lee et al., 2001b). Possible zones of mechanical discontinuity include the lithologic boundaries at the base of the upper crust or the base of the lower crust (Moho) (Meissner and Mooney, 1998); (Bird, 1979). Delamination is driven by a large negative density contrast between the lithosphere and underlying asthenosphere. The eclogitization of lower crust could be an important driving mechanism for developing such density instabilities (Kay and Kay, 1991), because eclogite is significantly denser than peridotite (Rudnick and Fountain, 1995). Once converted to eclogite, lower crust may sink into the mantle. Most models show that during delamination the entire original lithospheric mantle is removed along with much of the lower crust (Morency and Doin, 2004) (Schott and Schmeling, 1998). Our data, however, indicate that a portion of the Proterozoic SCLM (represented by R-type xenoliths) remained following removal of some of the lithosphere beneath Elephant Butte. Because most models for mechanical delamination require complete removal of the lithospheric mantle we conclude that this is not the most likely mechanism for thinning the lithosphere beneath the central RGR.

Alternative models for lithosphere removal/thinning call upon removal of the lithosphere through dripping, foundering, or thermal erosion (Lee et al., 2001b); (Houseman et al., 1981); (Conrad and Molnar, 1997). Dripping or foundering occurs as a result of the growth of Rayleigh-Taylor instabilities from the generation of lateral or vertical temperature gradients (Houseman and Molnar, 1997). Although SCLM is typically chemically buoyant due to lower Fe than primitive mantle, if the lithosphere cools sufficiently it may become denser than the underlying asthenosphere despite the chemical contrast between the lithosphere and asthenosphere. A similar model for removal of the lithosphere calls upon anomalously hot asthenosphere to be brought up to the base of the lithosphere causing convective instability that thermally erodes the colder denser lithosphere (Perry et al., 1987; Lee et al., 2001b). These convective removal models do not require a mechanical boundary layer and do not necessarily remove the lower crust or all of the pre-existing SCLM.

Convective erosion lithosphere removal models are more likely for describing the thinning of the RGR lithosphere, because they do not require complete removal of the mantle portion of the lithosphere as most mechanical delamination models do. Sinking of the Farallon slab in the mid-Tertiary (Humphreys et al., 2003) at the end of the Laramide would have brought hot asthenosphere to the base of the lithosphere that initiated convective erosion. Additionally, the upper mantle beneath the Colorado Plateau and throughout the southwestern U.S. has been shown to be wet (~30-100 ppm whole rock H_2O for The Thumb xenoliths) (Li et al., 2008). The viscosity of wet olivine aggregates (a proxy for lithospheric mantle) decreases by a factor of ~500 in the presence of relatively small amounts (~50 ppm) of water (Hirth and Kohlstedt, 1996). Recent subduction-related hydration and weakening of the lithosphere coupled with increased mantle flow due to slab rollback may have triggered removal of the lithosphere beneath the Rio Grande rift.

1.7 CONCLUSION

Xenoliths from Cerro Chato (on the eastern margin of the Colorado Plateau) are derived from Proterozoic SCLM and originated at a depth of ~55-60 km. Xenoliths from Elephant Butte (axis of central RGR) can be divided into two compositional groups. F-type xenoliths have fertile major element compositions, are LREE depleted, and have isotopic signatures similar to MORB and abyssal peridotites. These xenoliths derived from asthenospheric mantle that has been recently emplaced and thermally equilibrated at the base of the thinned pre-existing Proterozoic SCLM. The R-type xenoliths from Elephant Butte have refractory major element compositions, are LREE enriched, have unradiogenic Os isotopes and enriched Sr, Nd, and Pb isotopes. These derived from remnant Proterozoic SCLM. Because both groups have similar equilibration temperatures we conclude that they derived from similar depth, estimated to be ~45 km. The thickness of the Proterozoic SCLM is less than would be expected if passive rifting were the only cause of thinning. Convective removal of the lithosphere has occurred to account for this discrepancy.

ACKNOWLEDGEMENTS

This work was supported in part by NSF grant EAR-0911253 and by the University of Texas at Austin Jackson School of Geosciences. This manuscript benefitted from constructive comments from Cin-Ty Lee and an anonymous reviewer as well as from the editor Bernard Marty.

Chapter 2: Isotopically ultradepleted domains in the convecting upper mantle: Implications for MORB petrogenesis

ABSTRACT

Mid-oceanic ridge basalts (MORB) form by partial melting of material in the convecting upper mantle. The range in isotopic compositions observed in MORB is inconsistent with the ultradepleted isotopic compositions observed in many abyssal peridotites. These results have called into question the prevailing hypothesis that abyssal peridotites (APs) are simple residues of recent MORB melting, which should result in the two reservoirs having the same range in isotopic compositions. We examined xenoliths that, based on their chemical features (e.g., light rare earth element depleted, fertile major element compositions, Sr-Nd-Pb isotopes similar to estimates for depleted MORB mantle), are interpreted to be derived from the convecting upper mantle, in order to evaluate the potential for isotopically ultradepleted domains to contribute significantly to MORB petrogenesis. Our data support the idea that isotopically ultradepleted peridotite is widely distributed in the upper mantle, and we demonstrate that ultradepleted domains are capable of contributing to MORB petrogenesis. An isotopically enriched component, such as recycled oceanic crust, in the MORB source mantle can account for the lack of MORB with ultradepleted isotopic compositions.[2]

2.1 INTRODUCTION

Several recent studies have revealed a mismatch in the isotopic compositions of mid-oceanic ridge basalts (MORBs) and abyssal peridotites (APs), with many APs having extremely depleted isotopic compositions not observed in MORB. Although

---

[2] Portions of this chapter were published in 2014 in *Geology* 42, 203-206.

earlier studies (e.g., Snow et al., 1994) found clinopyroxene hosted in AP to have Sr and Nd isotopic compositions similar to that of MORB, recent results show that Nd and Hf isotopes in AP extend toward more depleted (radiogenic) compositions (Cipriani et al., 2004; Salters and Dick, 2002; Stracke et al., 2011; Warren et al., 2009), well beyond the range observed in MORB (Figure 2.1). Ultradepleted mantle domains are thought to be residues of ancient melt depletion that are not rehomogenized before being brought up again beneath a mid-ocean ridge (Liu et al., 2008; Rampone and Hofmann, 2012; Stracke et al., 2011). Herein ultradepleted refers to isotopic compositions that extend beyond the range observed in MORB (less radiogenic Sr, more radiogenic Nd and Hf) as a result of the time-integrated effect of incompatible trace element depletion. We use the term refractory to refer to peridotites with major element compositions that reflect significant melt removal (i.e., low Al and Ca). The abundance, composition, and distribution of ultradepleted domains in the mantle have major implications for current models for the composition of the convecting mantle and mechanisms for MORB melt generation.

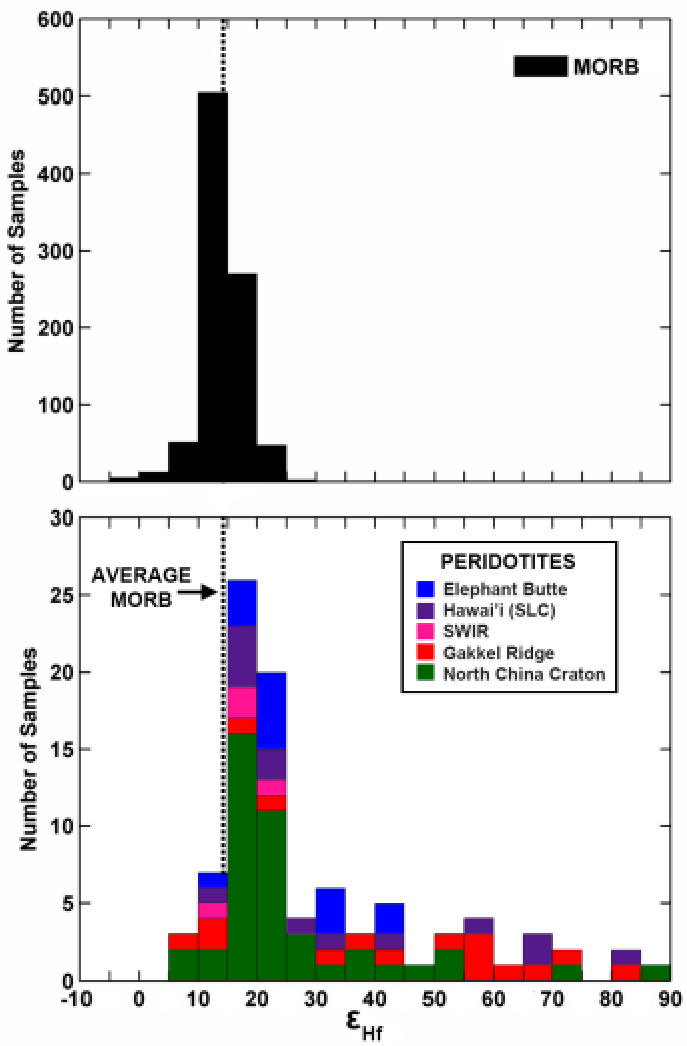

Figure 2.1 Distribution of Hf isotopes in mid-oceanic ridge basalt (MORB) and convecting upper mantle-derived peridotites.

MORB (upper panel) are restricted to εHf <~25. However, abyssal peridotites (lower panel) from Gakkel Ridge (eastern Arctic Ocean; data from Salters et al., 2011; Stracke et al., 2011) have been observed with εHf > 100. Also shown are other peridotites (Elephant Butte, New Mexico, USA, this study; Salt Lake Crater, Hawai'i, data from Bizimis et al., 2007; South West Indian Ridge, SWIR, data from Stracke et al., 2011; North China craton, data from Chu et al., 2009; Wu et al., 2006; Zhang et al., 2012) that sample convecting upper mantle that extend to highly depleted Hf isotopic compositions.

Three hypotheses are immediately apparent to explain the mismatch between MORB and AP isotopic compositions: (1) ultradepleted domains in the upper mantle are volumetrically minor, but are oversampled by AP, possibly due to their low density, and so are not representative of MORB source mantle (the “slag” hypothesis); (2) ultradepleted domains are common in the convecting upper mantle, but have refractory major element compositions, prohibiting these domains from participating significantly in melt generation beneath mid-ocean ridges (the “ghost” hypothesis); or (3) MORBs are generated by mixing of two or more isotopically distinct components. Melts from ultradepleted material mix with melts from isotopically enriched components to generate MORB with intermediate isotopic compositions (the “hybrid” hypothesis).

2.2 SAMPLES

We test these hypotheses using available data from ocean island xenoliths and APs, plus new data from a suite of asthenosphere-derived xenoliths from Elephant Butte, New Mexico (southwestern United States). Because APs may have undergone recent melt depletion, making it difficult to establish their original composition, we examined major element, trace element, and isotopic compositions of a suite of asthenosphere-derived xenoliths from the Rio Grande Rift to constrain the fertility and range in isotopic compositions of convecting upper mantle in an environment not affected by major recent melting and melt extraction. Our previous study of xenoliths from Elephant Butte (Rio Grande Rift) indicated that most of the preexisting Proterozoic lithospheric mantle in this region has been convectively removed and recently replaced with asthenospheric mantle (Byerly and Lassiter, 2012). Two populations of xenoliths are present at Elephant Butte. A small number of xenoliths have refractory major element compositions (bulk Al_2O_3 <

2.3 wt%, spinel Cr# 0.34 ± 0.12, 1σ), light rare earth element (LREE)–enriched trace element compositions [clinopyroxene $(La/Sm)_N > 2$], and enriched Sr-Nd-Pb isotopic compositions ($^{87}Sr/^{86}Sr$ 0.7032–0.7043, $^{206}Pb/^{204}Pb$ 19.2–19.9, ε_{Nd} 3.7–7.0). Along with xenoliths from the eastern Colorado Plateau, the refractory Elephant Butte xenoliths define a strong Lu/Hf-$^{176}Hf/^{177}Hf$ pseudo-isochron with an apparent age of ca. 1.6 Ga, consistent with estimates for the age of the crust in that region (Nelson and DePaolo, 1985). These refractory xenoliths therefore appear to sample surviving remnants of the original Proterozoic lithosphere beneath the Rio Grande Rift (Byerly and Lassiter, 2012). Another, more abundant, group of xenoliths have fertile major element compositions (bulk Al_2O_3 4.0 ± 0.5, 1σ; spinel Cr# 0.10 ± 0.01, 1σ) and LREE-depleted trace element patterns, each of which coincides with estimates for the average composition of the depleted upper mantle (Salters and Stracke, 2004; Workman and Hart, 2005). The major and trace element patterns are consistent with <4% melt extraction from primitive mantle (McDonough and Sun, 1995). This group of xenoliths derives from asthenospheric mantle that recently accreted to the base of the residual lithosphere at depths of 40–45 km (Byerly and Lassiter, 2012). This interpretation is further supported by the existence of anomalously slow V_p and V_s velocities beneath the central Rio Grande Rift that extend up to ~40 km depth, which are interpreted to be the result of significant lithosphere erosion beneath the central Rio Grande Rift (Gao et al., 2004).

The majority of asthenosphere-derived xenoliths from Elephant Butte have ultradepleted isotopic compositions, yet all maintain fertile major element compositions (Table 2.1). Most MORB samples (90%) have $^{87}Sr/^{86}Sr$ between 0.7020 and 0.7038, ε_{Nd} between 5 and 12, and ε_{Hf} between 8 and 20. In contrast, the Elephant Butte peridotites have $^{87}Sr/^{86}Sr$ ranging from 0.7018 to 0.7026, ε_{Nd} ranging from 8 to 27, and ε_{Hf} ranging from 12 to 40. The least-depleted samples have Sr, Nd, and Hf isotopic compositions that overlap with estimates for average depleted mantle (Salters and Stracke, 2004; Workman and Hart, 2005). Sr and Nd isotopic compositions, as well as Hf and Nd isotopes, are correlated and extend the mantle array to highly depleted values that are not observed in MORB (Figures. 2.2a,b). The observed Sr isotopic compositions are consistent with ancient (older than 1 Ga) melt depletion, which would have occurred prior to the recent (likely after 40 Ma, coincident with onset of Rio Grande Rift rifting and/or Farallon slab rollback) convective removal of the Proterozoic lithosphere. The strong correlation between Hf and Nd isotopes in the Elephant Butte xenoliths contrasts with other locales (e.g., Bizimis et al., 2007; Stracke et al., 2011), where decoupling of Hf and Nd isotopes has been interpreted to be the result of recent melt-rock interaction (Bizimis et al., 2004). In addition, the Elephant Butte xenoliths have LREE-depleted compositions, suggesting that their fertile major element compositions are not the result of metasomatism and/or refertilization.

Table 2.1 Sr-Nd-Hf Isotopic compositions of Elephant Butte xenoliths

	07EB1.01[a]	07EB1.05	07EB1.09[a]	07EB2.03	07EB4.01[a]	07EB4.05[a]	07EB4.21[a]
^{87}Sr/^{86}Sr	0.701756	0.702644	0.701857	0.702091	0.702518	0.702164	0.701778
^{143}Nd/^{144}Nd	0.514017	0.513094	0.513223	0.513466	0.513067	0.513168	0.513717
εNd	26.9	8.9	11.4	16.2	8.4	10.3	21.1
Nd (ppm)	2.24	2.72	4.75	3.54	4.55	3.71	1.35
^{147}Sm/^{144}Nd	0.34	0.32	0.26	0.29	0.27	0.26	0.43
^{176}Hf/^{177}Hf	0.283892	0.283267		0.283580	0.283104	0.283223	0.283541
εHf	39.6	17.5		28.6	11.7	15.9	27.2
Hf (ppm)	0.72	1.17		0.98	1.17	1.04	0.52
^{176}Lu/^{177}Hf	0.045	0.034		0.039	0.031	0.037	0.061
Spinel Cr#	0.108	0.091	0.085	0.106	0.082	0.093	0.111

	BELB 4-1	BELB 5-1[a]	BELB 5-5	BELB 5-8[a]	BELB 9-6	BELB 9-8[a]
^{87}Sr/^{86}Sr	0.702403	0.701877	0.702100	0.701986		0.702271
^{143}Nd/^{144}Nd	0.513258	0.513340	0.513688	0.513273	0.513612	0.513380
εNd	12.1	13.7	20.5	12.4	19.0	14.5
Nd (ppm)	4.17	2.50	3.11	3.70	2.90	2.31
^{147}Sm/^{144}Nd	0.24	0.34	0.30	0.27	0.30	0.35
^{176}Hf/^{177}Hf	0.283400		0.283748	0.283213	0.283880	0.283351
εHf	22.2		34.5	15.6	39.2	20.5
Hf (ppm)	0.96		0.87	1.02	0.74	0.72
^{176}Lu/^{177}Hf	0.039		0.048	0.047	0.045	0.054
Spinel Cr#	0.112	0.103	0.096	0.084	0.109	0.110

[a] Sr and Nd isotopic data from Byerly and Lassiter, 2012

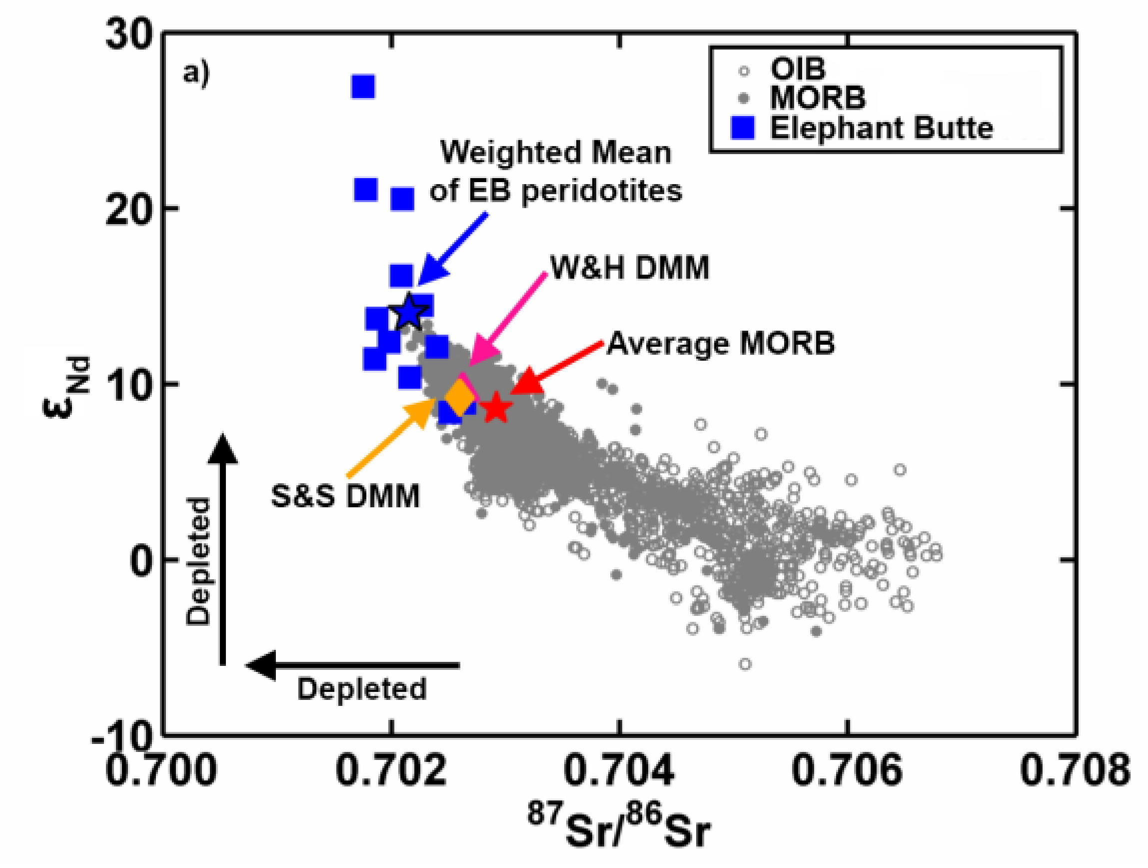

Figure 2.2a Plot of ε_{Nd} versus $^{87}Sr/^{88}Sr$.

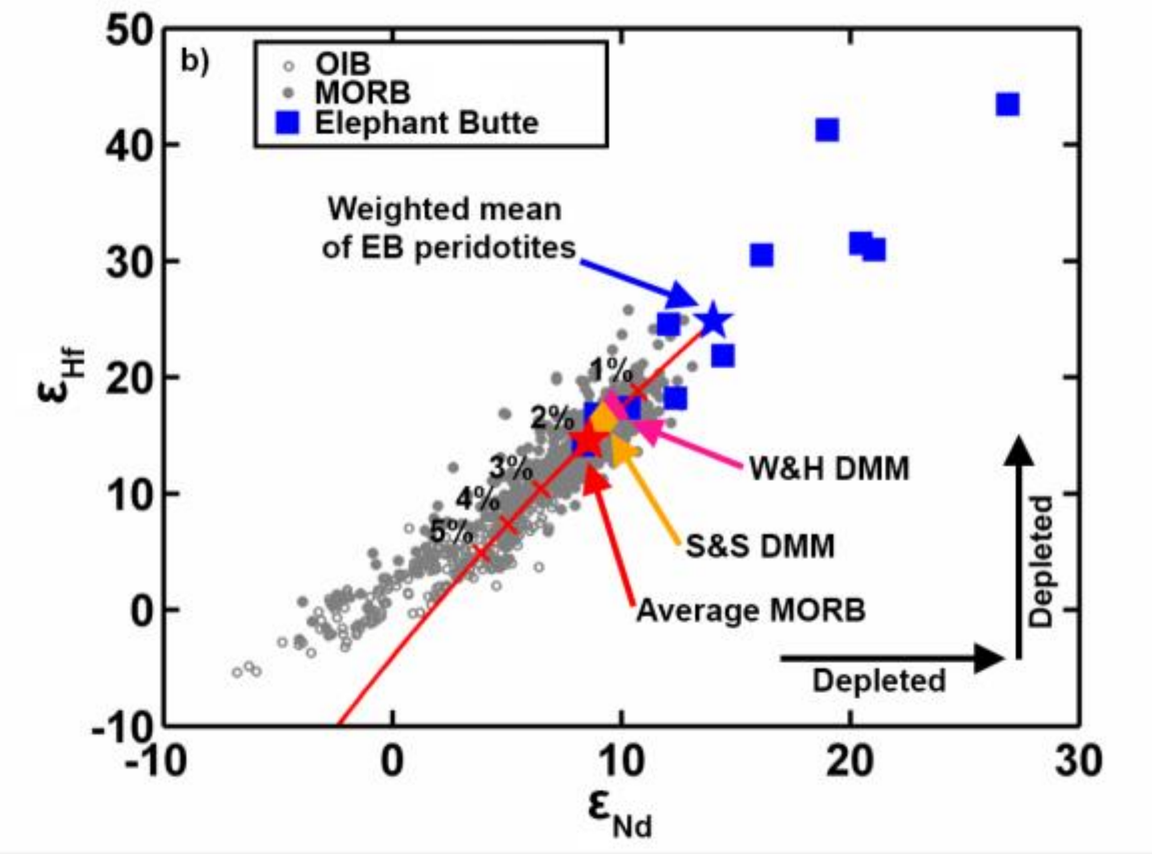

Figure 2.2b Plot of ε_{Hf} versus ε_{Nd}

Data are from clinopyroxene separates from Elephant Butte (EB; New Mexico, USA) xenoliths. Also shown are mid-oceanic-ridge basalts (MORB) ocean island basalts (OIB), and estimates from Salters and Stracke (2004; S&S) and Workman and Hart (2005; W&H) for average depleted MORB mantle (DMM). MORB and OIB data are from www.earthchem.org/petdb. Majority of EB xenoliths extend to highly depleted Sr, Nd, and Hf isotopic compositions, which are not observed in MORB. Solid red line is our model for mixing recycled 2 Ga MORB with weighted mean EB composition to generate range in modern MORB isotopic compositions. Red tick marks are in 1% intervals to 5% recycled material.

2.3 “SLAG” HYPOTHESIS

One hypothesis to explain the isotopic mismatch between average MORB and AP isotopic compositions is that ultradepleted domains are rare in the convecting mantle, but oversampled by AP. If ultradepleted mantle domains are highly refractory, they may be more buoyant than normal mantle (O’Reilly et al., 2009), allowing those domains to float and be oversampled at mid-ocean ridges. If this is the case, MORB and AP may not be directly genetically related. However, the majority of asthenosphere-derived xenoliths from Elephant Butte are relatively fertile, despite having ultradepleted Hf and Nd isotopic compositions similar to values observed in AP. Ultradepleted Hf and Os isotopic compositions have also been observed in ocean island xenoliths from Hawai’i (Salt Lake Crater; Bizimis et al., 2007) and the Ontong Java Plateau (Malaita, Solomon Islands; Ishikawa et al., 2011), as well as in mantle xenoliths from the North China craton that are derived from recently accreted (after 100 Ma) asthenosphere (Chu et al., 2009; Wu et al., 2006; Zhang et al., 2012). The prevalence of ultradepleted domains in myriad tectonic environments is strong evidence that these domains are not rare in the convecting upper mantle. In addition, for the ranges of melt extraction observed in AP (<20%), the density reduction associated with melt depletion at low pressures (<0.5%; Schutt and Lesher, 2006) is not sufficient to offset the density increase due to conductive cooling (>1.5%). Therefore, a lid of highly refractory cold material would not be convectively stable. Even if a slag melted, it would not have the same isotopic composition as MORB and could not explain the offset between MORB and AP isotopic compositions.

2.4 “GHOST” HYPOTHESIS

A second potential explanation for the mismatch between MORB and AP isotopic compositions is that ultradepleted domains are too refractory to contribute significantly to MORB petrogenesis. Ultradepleted domains from Hawai’i (Bizimis et al., 2007) and the Gakkel Ridge (eastern Arctic Ocean; Liu et al., 2008; Stracke et al., 2011) have more refractory major element compositions (e.g., lower Al_2O_3 and higher spinel Cr#) than estimates for average depleted MORB mantle (Figure 2.3). The refractory compositions observed in AP and other ultradepleted domains most likely reflect a mix of recent melt extraction (e.g., at the modern mid-ocean ridge) and ancient melt extraction (evidenced by broad correlations between $^{187}Os/^{188}Os$ and indicators of fertility, such as bulk Al_2O_3 or spinel Cr#, observed in AP and OIB xenoliths Cr#; Bizimis et al., 2007; Ishikawa et al., 2011; Liu et al., 2008).

To examine the effect of fertility on melt production we used pMELTS software (Ghiorso et al., 2002) to model the adiabatic ascent and melting of mantle with different fertilities beneath a mid-ocean ridge. The models start at 25 kbar and a potential temperature of ~1350 °C. The amount of melt generated is strongly controlled by the starting peridotite fertility. A mantle peridotite with 4.0 wt% Al_2O_3 (average composition of Elephant Butte xenoliths) will generate ~24% melt by 2 kbar (approximate base of oceanic crust), whereas a sample with 1.6 wt% Al_2O_3 (average composition of Salt Lake Crater, Hawai’i, xenoliths) will only generate ~8% melt by 2 kbar. Although it is possible that ultradepleted domains within the convecting mantle with low (<~1 wt%) Al_2O_3 exist as “ghosts,” unable to generate appreciable melt beneath mid-ocean ridges, ultradepleted domains with compositions similar to samples from Hawai’i (average $Al_2O_3 = 1.6 \pm 0.7$, 1σ) and the Gakkel Ridge (average $Al_2O_3 = 2.3 \pm 0.4$, 1σ) are sufficiently fertile to generate significant quantities of melt, assuming a typical potential temperature for upper mantle. These domains therefore should be sampled during MORB petrogenesis, leaving unresolved the lack of such isotopic signatures in MORB.

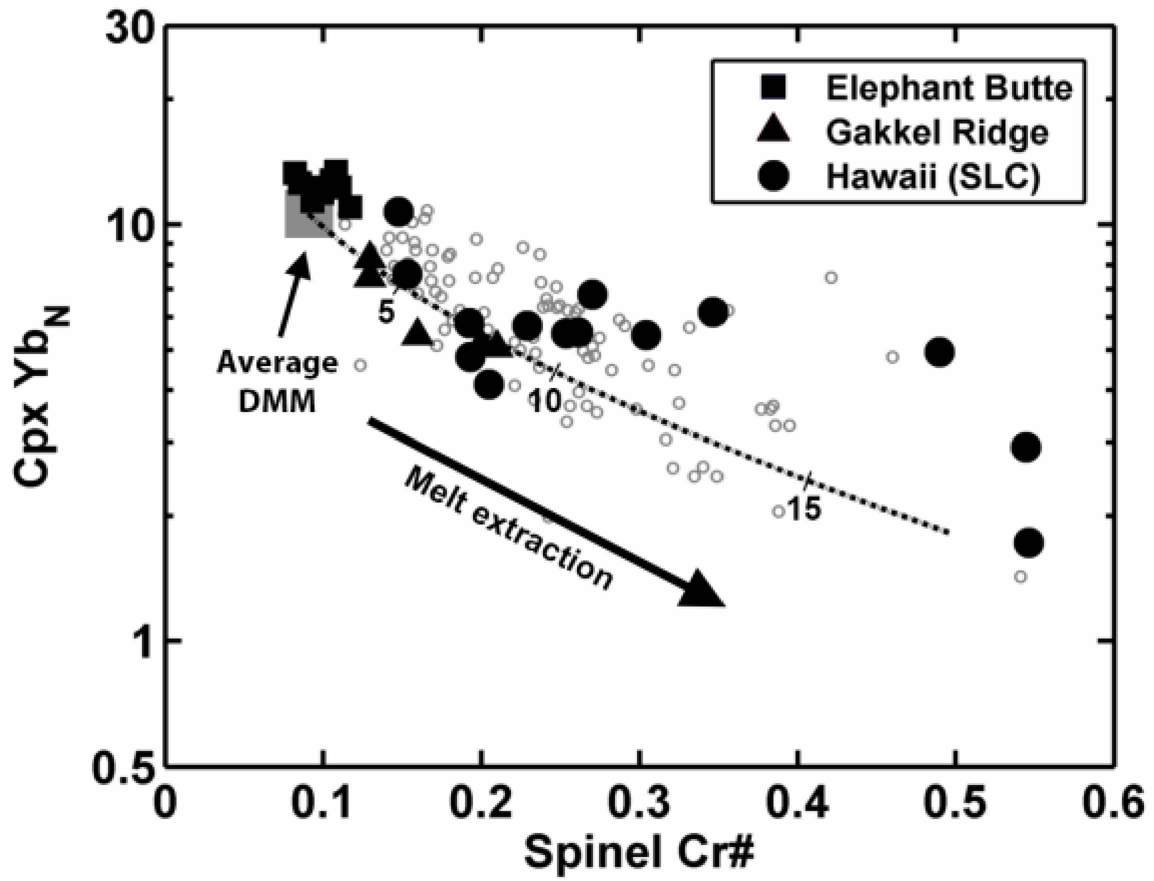

Figure 2.3 Plot of clinopyroxene (cpx) Yb (normalized to chondrite) versus spinel Cr# in ultradepleted domains

Modified after Byerly and Lassiter (2012). Dashed line shows melting model after Hellebrand et al. (2001). Peridotites from Gakkel Ridge (eastern Arctic Ocean) and Salt Lake Crater (SLC, Hawai'i) have refractory compositions that would not contribute significant amount of melt to mid-oceanic ridge basalt (MORB) petrogenesis. However, Elephant Butte (New Mexico, USA) xenoliths have fertile major element compositions and would generate melts with ultradepleted compositions if brought up beneath mid-ocean ridge. Also shown are global abyssal peridotites (gray circles). DMM—depleted MORB mantle.

2.5 "HYBRID" HYPOTHESIS: PREFERENTIAL SAMPLING OF PYROXENITE AND PERIDOTITE DURING MORB PETROGENESIS

Because ultradepleted domains in convecting upper mantle are sufficiently fertile to generate melt when advected, there must be widespread generation of isotopically depleted melts beneath mid-ocean ridges. MORBs with such depleted isotopic compositions are not observed. Therefore, an additional isotopically enriched component must also be ubiquitous in the mantle. Melts from this component mix with melts derived from depleted peridotite to yield the isotopic compositions observed in MORB. Pyroxenite or eclogite derived from ancient recycled oceanic crust have frequently been called upon to explain chemical heterogeneities within the upper mantle (Allègre and Turcotte, 1986), and are candidates for the enriched end member that would mix with ultradepleted melts to generate MORB. Pyroxenites and/or eclogites can have a disproportionately large impact on MORB compositions relative to their abundance in the mantle because these lithologies have higher concentrations of incompatible trace elements and experience higher overall degrees of melting than peridotites. In Figure 2.2b we present a model in which peridotite with the average composition of the Elephant Butte xenoliths is mixed with recycled MORB that was generated at 2 Ga. Mixing between 1% and 5% of the enriched component can account for ~90% of the Hf and Nd isotopic compositions observed in MORB today. The model in Figure 2.2b represents solid-state mixing. The amounts of each component required are likely similar for mixing of melts as a result of a balance between higher Nd and Hf partition coefficients and higher degrees of partial melting in the enriched component. Observations from MORB melt inclusions (Maclennan, 2008; Shimizu, 1998) and MORB oxygen isotopes (Eiler et al., 2000) support the idea that enriched and/or recycled material is present in the mantle.

Mixing of pyroxenite- and peridotite-derived melts has also been proposed as a possible source of the "garnet signature" in MORB (Hirschmann and Stolper, 1996).

The ultradepleted isotopic compositions observed in convecting upper mantle–derived peridotites (Figure 2.1) are consistent with the idea that the range of fertilities observed in AP is, to some extent, an inherent heterogeneity that is unrelated to recent melting beneath mid-ocean ridges. The Elephant Butte xenoliths likely represent a fertile end member of upper mantle peridotite. A consequence of a heterogeneous peridotitic upper mantle is that conventional models that use MORB to estimate average upper mantle composition are biased toward more fertile components. We demonstrate this (see the Data Repository) by modeling adiabatic melt generation from heterogeneous peridotitic mantle that underwent variable ancient depletion. Because the more fertile (and less depleted) components generate more melt and have higher incompatible trace element concentrations than the refractory (and more depleted) components, the resulting melts have isotopic compositions that are less depleted than the average source composition. We show a melt model for mantle with bulk Al_2O_3 of 3.2 ± 0.5 (1σ) and a weighted mean □$_{\mathrm{Hf}}$ of ~45 (see the Data Repository), where weighted melts generated from this mantle have □$_{\mathrm{Hf}}$ of ~30. The MORB source is heterogeneous and MORB compositions are biased due to preferential melting of pyroxenitic and fertile peridotitic source components.

2.6 CONCLUSIONS

Isotopically ultradepleted components are ubiquitous in the upper mantle, and we demonstrate that these components are not necessarily refractory. As evidenced by the wide range of isotopic compositions observed in convecting upper mantle samples, the convecting peridotitic mantle has undergone variable amounts of melt depletion. Because these ultradepleted components are widespread and capable of generating melt, the mismatch between their isotopic compositions and that of MORB indicates that (1) MORBs oversample fertile (less depleted) peridotitic mantle, and/or (2) an enriched component (pyroxenite and/or eclogite) contributes to MORB petrogenesis.

ACKNOWLEDGEMENTS

This work was supported in part by National Science Foundation grants EAR-0648409 and EAR-0911253, and by the University of Texas at Austin Jackson School of Geosciences. Comments from V. Le Roux, G. Pearson, an anonymous reviewer, and editor R. Holdsworth helped to improve this manuscript.

Chapter 3: Reinterpreting the significance of Lu-Hf ages in spinel peridotites

3.1 INTRODUCTION

Many studies have applied the Lu-Hf system in peridotites in order to constrain the timing of melt depletion in lithospheric mantle (Carlson et al., 2004; Choi and Mukasa, 2012; Choi et al., 2008; Choi et al., 2010; Chu et al., 2009; Lazarov et al., 2012; Liu et al., 2012; Schmidberger et al., 2002; Shaw et al., 2007). Ancient melt depletion in lithospheric mantle is commonly associated with crust formation and stabilization of the local SCLM. The assumption is that at the time of lithospheric mantle formation (typically >1 Ga; (Pearson, 1999)), Lu and Hf are variably fractionated by different degrees of melt extraction. Lutetium is more compatible than Hf during partial melting of spinel and garnet peridotites (c.f. (Hart and Dunn, 1993; Hauri et al., 1994)). Therefore, the Lu/Hf ratio will increase as the degree of melt extraction increases. The time-integrated effect of this should result in correlations between Lu/Hf ratios and Hf isotopes amongst xenoliths that sample SCLM that experienced the same melting event.

The most common method of inferring Lu-Hf melt-depletion ages in SCLM samples is to construct a whole rock isochron from a suite of xenoliths using clinopyroxene (cpx) ^{176}Lu/^{177}Hf and cpx ^{176}Hf/^{177}Hf. A whole rock isochron is similar to a traditional mineral isochron except that it includes data from multiple samples that are grouped together under the assumption that they are genetically related. Clinopyroxene ^{176}Lu/^{177}Hf and ^{176}Hf/^{177}Hf are commonly used because these ratios are easy to measure in cpx because it is a major host for Lu and Hf in spinel peridotites and these elements are present in high concentrations relative to other phases. The use of cpx Lu/Hf ratios and Hf isotopes to construct an "isochron" assumes one of two things: either that the samples are below their Lu-Hf closure temperature (i.e. cpx ^{176}Hf/^{177}Hf is a function of the cpx Lu/Hf ratio), or that samples are above their Lu-Hf closure but the cpx Lu/Hf ratio is identical to the whole rock Lu/Hf ratio. Additionally, it is assumed that the Lu-Hf system has remained closed since the initial melt depletion event (i.e. no metasomatic overprinting has occurred). If any of these assumptions are incorrect, then Lu/Hf – Hf isotope correlations could be misinterpreted.

We measured whole rock, orthopyroxene, and clinopyroxene trace element abundances and Hf and Nd isotopic compositions of two suites of well-equilibrated spinel peridotite xenoliths in order to evaluate the factors that affect the Lu-Hf systematics in spinel peridotites. In doing so, it is possible to establish the trace element budget of the samples, infer whole rock Lu/Hf ratios and compare them to cpx Lu/Hf ratios. This is necessary to evaluate the validity of Lu-Hf ages from cpx Lu/Hf – Hf isotope whole rock "isochrons" for samples that have equilibrated above their Lu-Hf closure temperature. Comparison between cpx and opx Hf and Nd isotopes can establish whether samples have achieved isotopic equilibrium (i.e. above or below their closure temperature). Lastly, Hf isotope compositions can be compared with indicators of both melt depletion and metasomatism to elucidate the causes of Lu/Hf – Hf isotope correlations that are commonly observed in suites of spinel peridotite xenoliths and interpreted to be of age significance.

3.2 SAMPLES AND ANALYTICAL METHODS

The samples in this study are spinel peridotites that range from lherzolites to harzburgites. They are from Cerro Chato and Elephant Butte, which are on the Eastern margin of the Colorado Plateau and the Central Rio Grande rift, respectively. Samples are described in detail in Byerly and Lassiter (2012) and Byerly and Lassiter (2014). The samples from Cerro Chato are derived from Proterozoic lithospheric mantle that has been variably melt depleted (spinel Cr# ranges from 0.15-0.45) and metasomatised (cpx $(La/Sm)_N$ ranges from 0.7-11). Two groups of xenoliths are present in Elephant Butte samples. One group samples Proterozoic lithosphere and is broadly similar to the Cerro Chato xenoliths, except they are generally more refractory (spinel Cr# ranges from 0.14-0.50). The other group from Elephant Butte samples asthenospheric mantle that has been recently accreted to the base of the Proterozoic lithosphere (Byerly and Lassiter, 2012). These xenoliths are fertile (average bulk Al_2O_3 ~ 4 wt. %, spinel Cr# ranges from 0.08-0.13) and are LREE-depleted. We observed olivine, opx, cpx, and spinel (± interstitial glass) in the xenoliths. Sulfides are also present, but are only identifiable via electron probe analysis. The asthenosphere- and lithosphere-derived samples have overlapping two-pyroxene (T_{BKN}, (Brey and Köhler, 1990)) equilibration temperatures that range from 943-1065 °C and 848-1104 °C, respectively.

Trace element concentrations in cpx and opx were measured by LA-ICP-MS on an Agilent 7500ce quadrupole, following the methods of Byerly and Lassiter (2012). Chemical separation of Nd from REE was achieved with HDEHP resin following the methods of Byerly and Lassiter (2012). Chemical separation of Lu and Hf followed the methods of Connelly et al. (2006). Neodymium was measured using double rhenium filaments on a Thermo Triton TIMS. Lu and Hf were measured via MC-ICP-MS on a Micromass (GV) Isoprobe, as outlined in Byerly and Lassiter (2014). Whole-rock powders were analyzed for major and trace elements at the GeoAnalytical at Washington

State University. Details of the accuracy, precision, and standards for trace element and isotopic analysis can be found in Appendix 7.

3.3 RESULTS

Major element analyses, Os-isotope analyses, and some Cpx trace element and Nd isotope analyses were previously reported in Byerly and Lassiter (2012). Results of clinopyroxene and orthopyroxene trace element analyses are presented in Appendix 2 and 3. Orthopyroxene and clinopyroxene trace element compositions are generally well correlated (Figure 3.1a,b). The asthenosphere-derived samples are LREE depleted ($(La/Sm)_N$ ranges from 0.04-0.42). The lithosphere-derived samples are LREE enriched. Excluding one sample whose $(La/Sm)_N = 0.7$, the lithosphere-derived samples have $(La/Sm)_N$ that range from 1.4-10. Clinopyroxenes from both suites of xenoliths display negative high field strength element (HFSE) anomalies relative to REE (e.g. $Hf/Hf^* < 1$, where $Hf^* = (Nd+Sm)_N/2)$). Orthopyroxenes display a complementary enrichment in HFSE (e.g. $Hf/Hf^* > 1$) relative to REE.

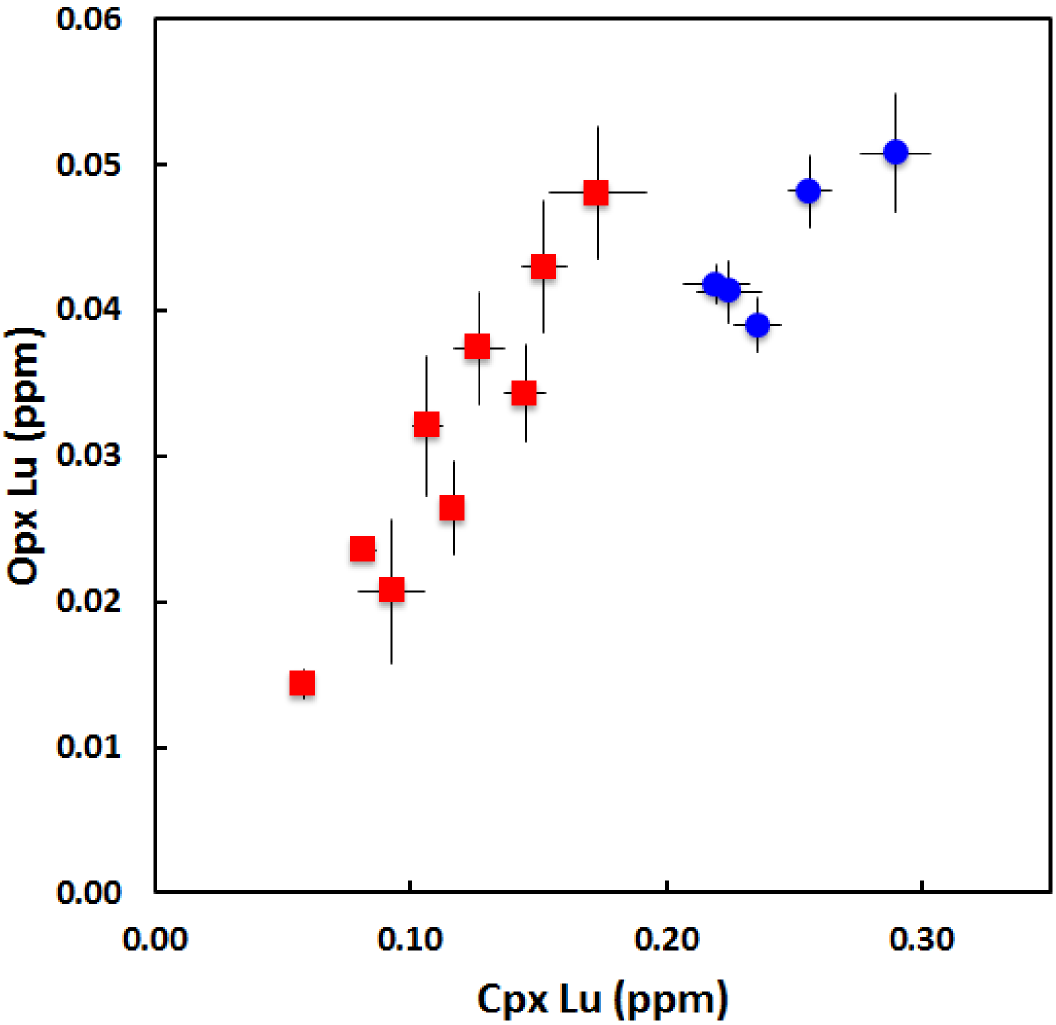

Figure 3.1a Plot of Lu in orthopyroxene versus Lu in clinopyroxene

Blue circles, asthenosphere-derived samples; red squares, lithosphere-derived samples

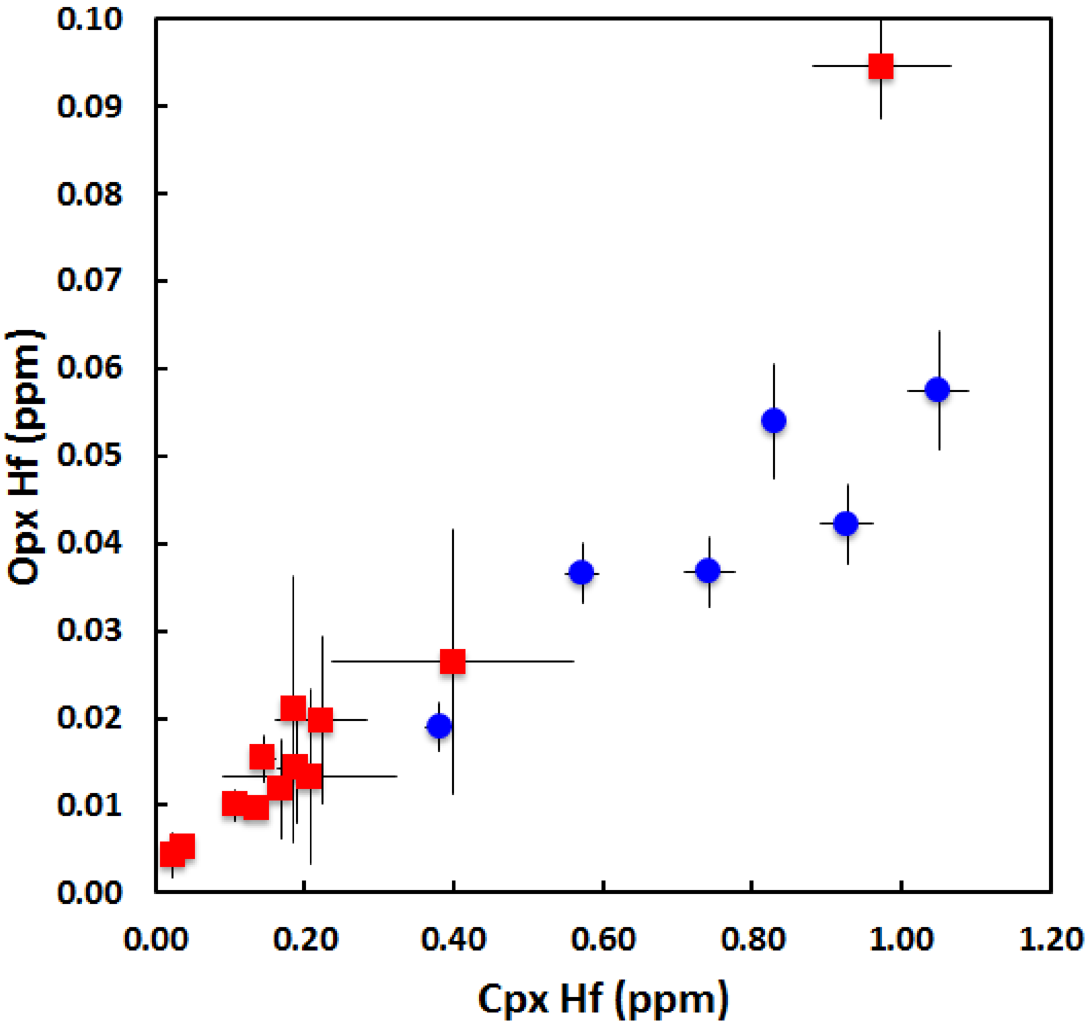

Figure 3.1b Plot of Hf in orthopyroxene versus Hf in clinopyroxene

Symbols as in Figure 3.1a

Clinopyroxene, opx, and whole-rock Hf and Nd isotopic analyses are presented in Tables 3.1 and 3.2. The Nd and Hf isotope systematics of the asthenosphere-derived samples from Elephant Butte are discussed in Byerly and Lassiter (2014). The asthenosphere-derived samples have cpx ε_{Nd} that range from +8 to +27. The lithosphere-derived samples have a narrower range of cpx Nd isotopes (ε_{Nd} from +4 to +10). Orthopyroxenes and bulk xenoliths have Nd isotopes that are identical to or less radiogenic than cpx Nd isotopes from the same sample. Clinopyroxene Hf isotopes in the asthenosphere-derived Elephant Butte samples range from ε_{Hf} of +12 to +40, and are positively correlated with ε_{Nd}. Lithosphere-derived samples from Elephant Butte have cpx ε_{Hf} ranging from +17 to +78 and do not correlate with ε_{Nd}. Clinopyroxenes from Cerro Chato have ε_{Hf} that range from +18 to +304. Bulk-xenolith and opx Hf isotopes are similar to or less radiogenic than cpx Hf isotopes from the same sample.

	Clinopyroxene			Orthopyroxene			Whole Rock		
	$^{176}Hf/^{177}Hf$	2se	εHf	$^{176}Hf/^{177}Hf$	2se	εHf	$^{176}Hf/^{177}Hf$	2se	εHf
07EB1.01[a]	0.283892	0.000015	39.6	0.283808	0.000067	36.6	0.283640	0.000049	30.7
07EB1.05[a]	0.283267	0.000007	17.5	-	-	-	-	-	-
07EB2.03[a]	0.283580	0.000029	28.6	-	-	-	-	-	-
07EB4.01[a]	0.283104	0.000007	11.7	0.283116	0.000037	12.2	-	-	-
07EB4.05[a]	0.283223	0.000005	15.9	-	-	-	0.283199	0.000036	15.1
07EB4.21[a]	0.283541	0.000006	27.2	-	-	-	0.283559	0.000047	27.8
07EB1.06	0.284944	0.000026	76.8	-	-	-	-	-	-
07EB1.11	0.284969	0.000034	77.7	-	-	-	-	-	-
BELB 4-30	0.283487	0.000008	25.3	0.283487	0.000008	25.3	-	-	-
BELB 4-5	0.283244	0.000007	16.7	-	-	-	-	-	-
CC07-1-06	0.283564	0.000013	28.0	-	-	-	0.283152	0.000034	13.4
CC07-1-09	0.285274	0.000012	88.5	-	-	-	-	-	-
CC07-1-14	0.284548	0.000015	62.8	-	-	-	-	-	-
CC07-1-22	0.291387	0.000044	304.7	-	-	-	-	-	-
CC07-1-24	0.285031	0.000021	79.9	-	-	-	-	-	-
CC07-1-35	0.284439	0.000013	59.0	-	-	-	-	-	-
CC07-1-51	0.284385	0.000015	57.0	-	-	-	-	-	-
CC07-2-01	0.283273	0.000007	17.7	0.283115	0.000015	12.1	0.283007	0.000026	8.3
CC07-3-01	0.284804	0.000006	71.9	0.283898	0.000075	39.8	0.283329	0.000022	19.7

[a] Cpx Hf isotopes originally reported in Byerly and Lassiter, 2014

Table 3.1 Clinopyroxene, orthopyroxene, and whole rock hafnium isotopes

	Clinopyroxene			**Orthopyroxene**			**Whole Rock**		
	^{143}Nd/^{144}Nd	**2se**	**εNd**	**^{143}Nd/^{144}Nd**	**2se**	**εNd**	**^{143}Nd/^{144}Nd**	**2se**	**εNd**
07EB1.01[a]	0.514017	0.000006	26.9	0.513911	0.000102	24.8	0.513704	0.000006	20.8
07EB1.05[b]	0.513094	0.000004	8.9						
07EB1.09[a]	0.513223	0.000005	11.4						
07EB2.03[b]	0.513466	0.000005	16.2						
07EB4.01[a]	0.513067	0.000006	8.4	0.512946	0.000068	6.0	0.513031	0.000005	7.7
07EB4.05[a]	0.513168	0.000005	10.3				0.513087	0.000027	8.8
07EB4.21[a]	0.513717	0.000010	21.1				0.513543	0.000007	17.7
07EB1.11	0.512830	0.000008	3.7						
BELB 4-30[a]	0.513005	0.000010	7.2	0.512996	0.000017	7.0	0.512847	0.000016	4.1
BELB 4-5	0.512958	0.000004	6.2						
CC07-1-06[a]	0.512955	0.000003	6.2				0.512930	0.000004	5.7
CC07-1-09	0.512962	0.000004	6.3						
CC07-1-14	0.512978	0.000006	6.6						
CC07-1-20[a]	0.512942	0.000003	5.9				0.512821	0.000026	3.6
CC07-1-22	0.513140	0.000005	9.8						
CC07-1-35[a]	0.512899	0.000007	5.1						
CC07-1-41	0.512902	0.000005	5.1						
CC07-1-51[a]	0.512933	0.000004	5.8						
CC07-2-01[a]	0.512880	0.000004	4.7	0.512910	0.000013	5.3	0.512899	0.000005	5.1
CC07-3-01[a]	0.513007	0.000022	7.2	0.513059	0.000048	8.2	0.512933	0.000006	5.8

[a] Cpx Nd isotopes originially reported in Byerly and Lassiter, 2012

[b] Cpx Nd isotopes originially reported in Byerly and Lassiter, 2014

Table 3.2 Clinopyroxene, orthopyroxene, and whole rock neodymium isotopes

3.4 DISCUSSION

3.4.1 Trace element partitioning between clinopyroxene and orthopyroxene

There are many models that define the variable effects of pressure, temperature, and composition on trace element partitioning between two mantle phases. A common practice is to employ lattice strain models fitted to experimental data to estimate pyroxene-melt partition coefficients (Sun and Liang, 2012; Wood and Blundy, 1997; Yao et al., 2012). These models use the Brice (1975) equation for lattice strain energy to estimate partition coefficients as a function of temperature and ionic radius (a function of crystal composition). A useful review of lattice strain theory can be found in Wood and Blundy (2003). Witt-Eickschen and O'Neill (2005) used data from chemically well-equilibrated natural samples to construct a model for the effects of temperature and composition on cpx-opx-olivine-spinel partitioning. They found temperature to be the most significant factor for determining cpx-opx partition coefficients. On a thermodynamic basis they suggest that cpx Na content and spinel Cr# should also impart small effects. Yao et al. (2012) showed their opx-melt model combined with the cpx-melt model of Sun and Liang (2012) to be in good agreement with the Witt-Eickschen and O'Neill model.

We used the measured trace element compositions of clinopyroxene and orthopyroxene from our samples to estimate cpx/opx partition coefficients. The predominance of 120° triple junctions suggests that most of the samples are in textural equilibrium. Orthopyroxene and clinopyroxene REE and HFSE are generally well correlated (Figure 3.1a,b) which is consistent with cpx-opx equilibrium. Cpx-opx equilibria of REE can also be quantified using the methods of Agranier and Lee (2007) and Lee et al. (2007). Following lattice strain theory, REE partition coefficients (i.e.

C_{opx}/C_{cpx}) should correlate negatively with ionic radius. This is due to the fact that the optimum site radius (r_0) is larger in clinopyroxene than in orthopyroxene and most REE have ionic radii that are larger than r_0 in cpx (Lee et al., 2007). Therefore, the strain energy associated with accommodating a given REE will be larger in opx than in cpx, and the difference between the strain energies will increase with increasing cationic radius (i.e. $D^{cpx/opx}$ decreases as ionic radius decreases). Examples of our estimated opx-cpx partition coefficients plotted versus cationic radius are shown in Figure A7.1. For most of our samples we see trends in partition coefficients that fit those predicted by lattice strain theory. However, for some samples there is disequilibria between cpx and opx for the LREE.

Average $D^{cpx/opx}$ for the asthenosphere-derived and lithosphere-derived samples are shown in Figure 3.2. The lithosphere-derived samples, which have more refractory compositions than the asthenosphere-derived samples, have lower average $D^{cpx/opx}$ for REE and HFSE. For both suites of samples, the $D^{cpx/opx}$ that we estimate are consistent with those predicted by the formulation of Witt-Eickschen and O'Neill (2005) (Figure 3.3a,b). That study primarily focused on moderately refractory xenoliths whose spinel Cr# range from 0.13-0.47. Our samples overlap with and extend the range to more fertile compositions (spinel Cr# ranges from 0.08-0.37). Partitioning between cpx and opx (e.g. $D^{cpx/opx}$) will be controlled by temperature and composition. However, the relative impact of each of these variables differs from element to element. If we consider temperature to be the only control on $D^{cpx/opx}$ we observe, for the HREE, Zr, and Hf, that variations in temperature alone do not account for the scatter in the data (Figure 3.4a). Light to middle REE $D^{cpx/opx}$ (e.g. Nd, Figure 3.4b) display a better correlation with temperature. For a narrow range in temperature (950 -1050°C) at a fixed composition the Witt-Eickschen and O'Neill (2005) model predicts a 50% variation for $D_{Nd}^{cpx/opx}$, but only a 15% $D_{Lu}^{cpx/opx}$. In contrast, we see that, for the HREE, Zr, and Hf, variations in composition over a narrow temperature range impart a large effect on $D^{cpx/opx}$ (Figure 3.4c). This is not seen for the L-MREE (Figure 3.4d). The large effect of composition on HREE, Zr, and Hf distribution coefficients is manifested as a strong correlation between $D^{cpx/opx}$ and cpx MgO content (Figure 3.5a,b) and other indices of peridotite fertility (e.g. spinel Cr#) in our samples. This is due to the fact that, for the limited range in temperature covered by our samples, variations in composition impart a larger effect on HREE, Zr, and Hf cpx-opx partitioning than variations in temperature, as predicted by the Witt-Eickschen and O'Neill (2005) model. One result of this compositional effect over narrow temperature ranges is that cpx-opx partition coefficients for HREE, Zr, and Hf will decrease with increased melt removal (cpx MgO content generally increases and cpx Na content decreases with melt extraction).

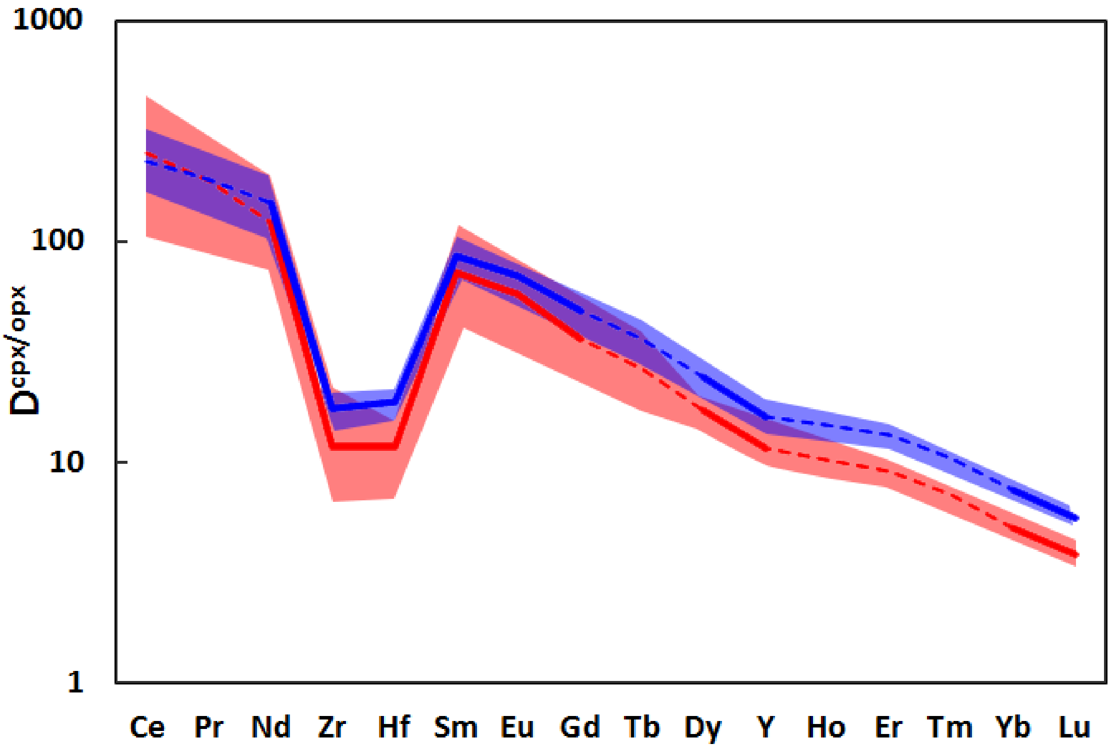

Figure 3.2 Comparison of average partition coefficients between asthenosphere and lithosphere-derived samples.

Shown are average $D^{cpx/opx}$ for asthenosphere-derived samples (solid blue line, dashed where inferred) and lithosphere-derived samples (solid red line, dashed where inferred) and the ranges for each group of samples (blue and red fields).

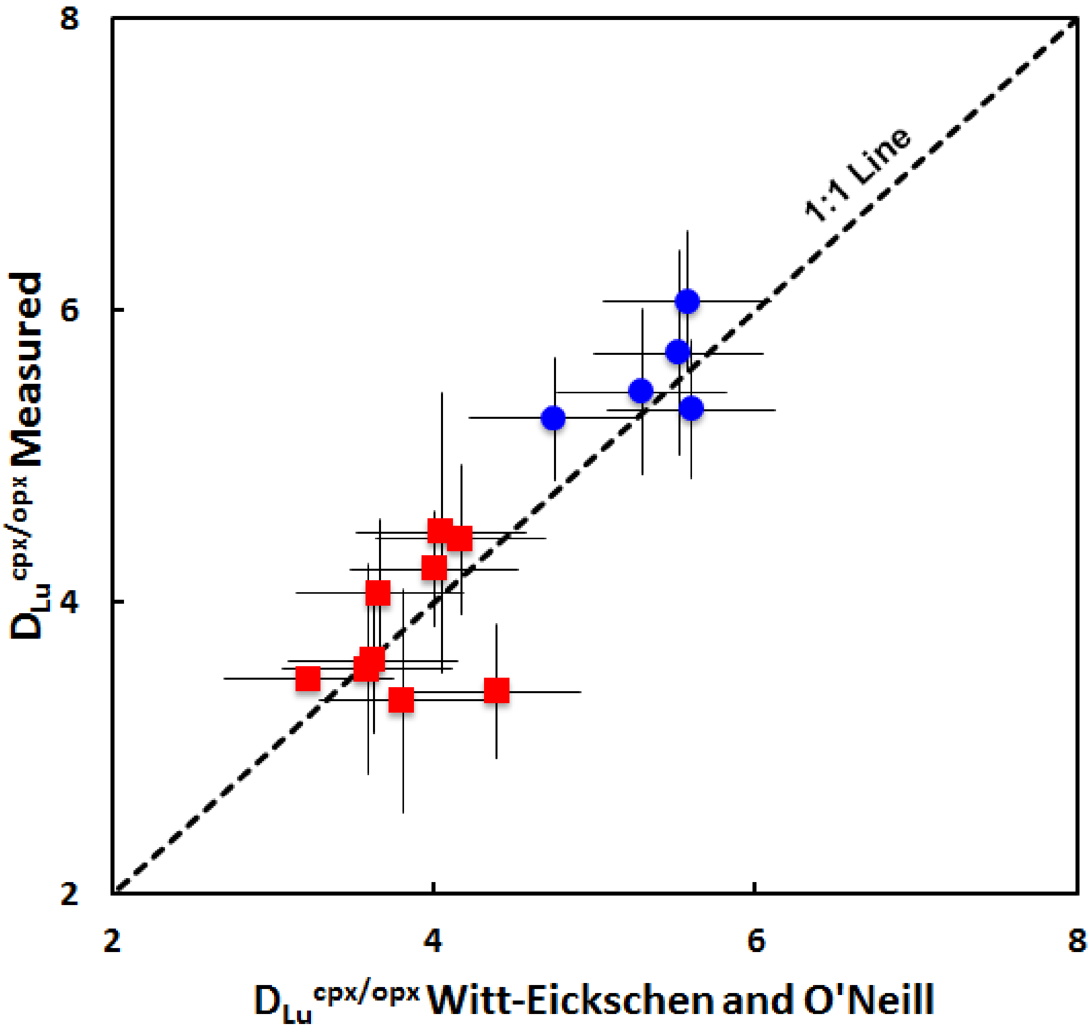

Figure 3.3a Comparison of measured $D_{Lu}^{cpx/opx}$ vs. modeled $D_{Lu}^{cpx/opx}$

Symbols as in Figure 3.1a

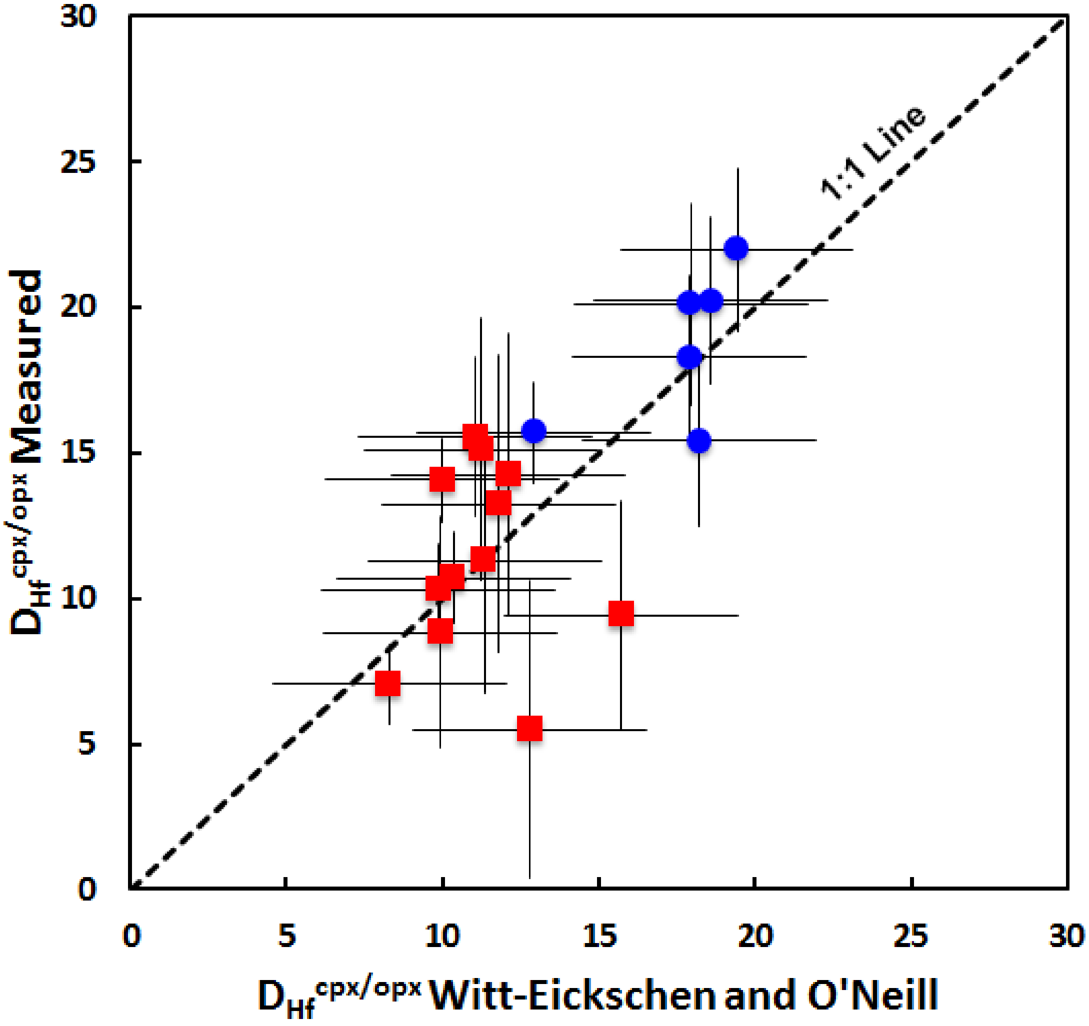

Figure 3.3b Comparison of measured $D_{Hf}^{cpx/opx}$ vs. modeled $D_{Hf}^{cpx/opx}$

Symbols as in Figure 3.1a

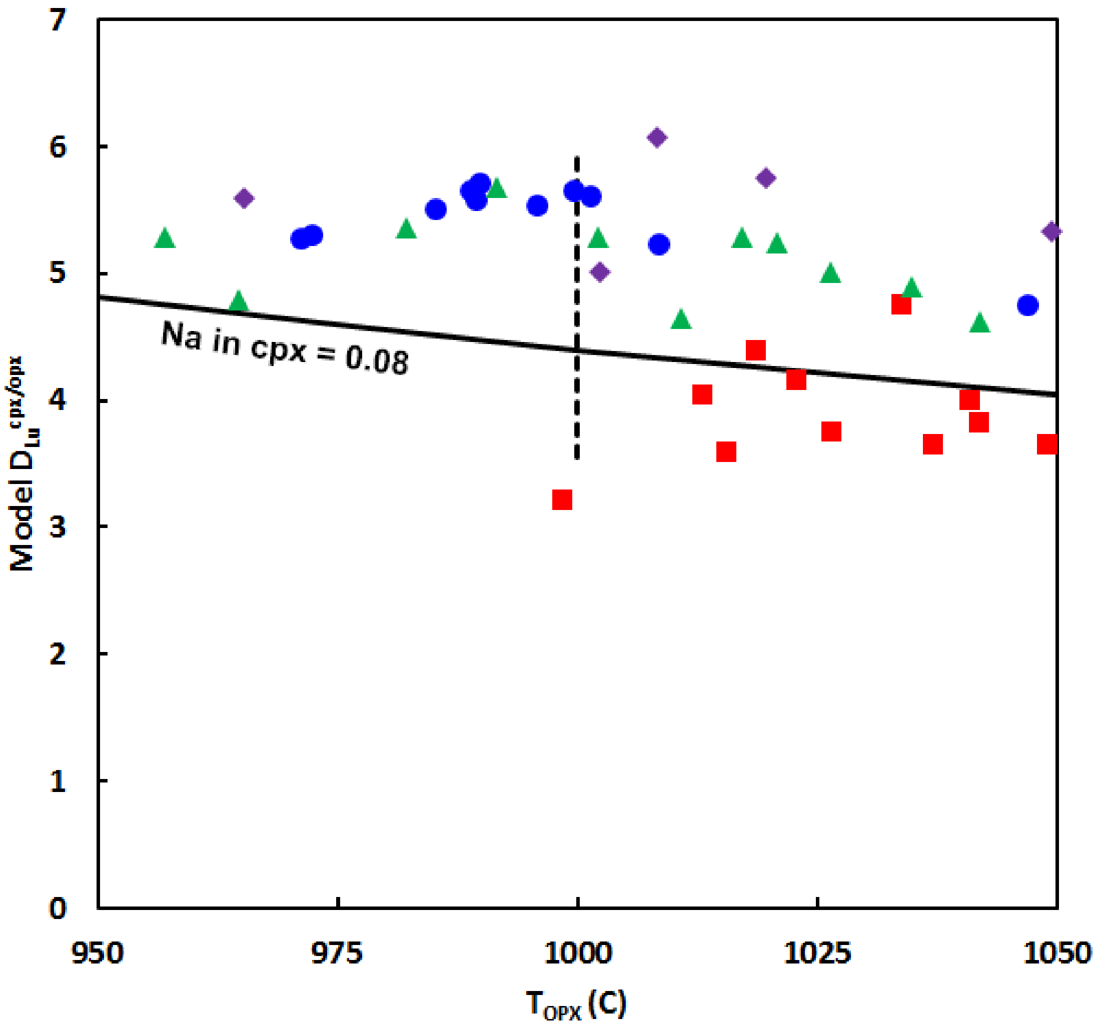

Figure 3.4a Plot of model $D_{Lu}^{cpx.opx}$ versus equilibration temperature.

$D_{Lu}^{cpx.opx}$ is modeled following the formulation of Witt-Eickschen and O'Neill (2005). Solid black line shows the variation in $D_{Lu}^{cpx.opx}$ with temperature at a fixed composition (Na in cpx = 0.08). Dashed line shows the variation in $D_{Lu}^{cpx.opx}$ with composition (Na in cpx range from 0.04-0.14) at a constant temperature. Data from this study (same as Figure 3.1a), Harvey et al. (2012), triangles, and Witt-Eickschen et al. (2009) diamonds.

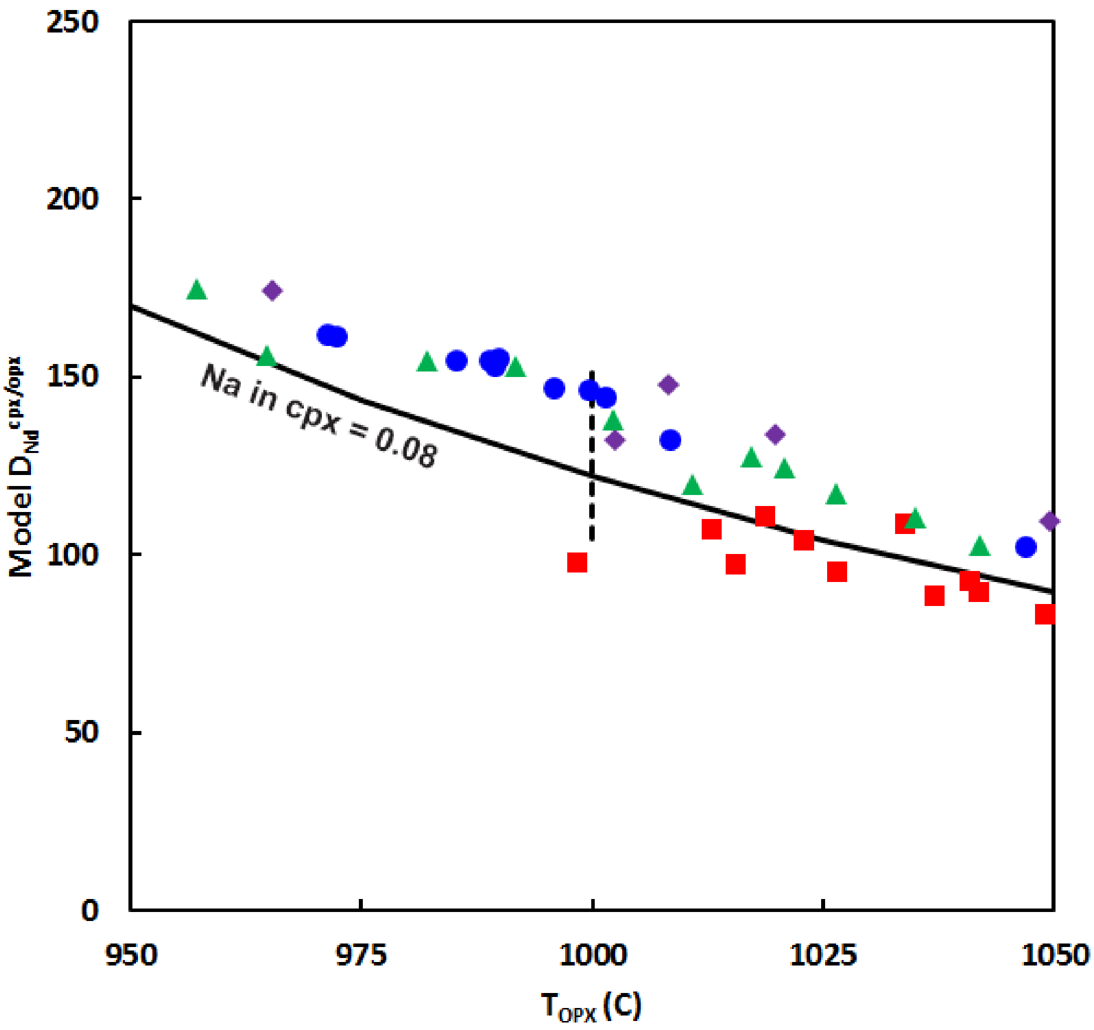

Figure 3.4b Plot of model $D_{Nd}^{cpx.opx}$ versus equilibration temperature.

$D_{Nd}^{cpx.opx}$ is modeled following the formulation of Witt-Eickschen and O'Neill (2005). Solid black line shows the variation in $D_{Nd}^{cpx.opx}$ with temperature at a fixed composition (Na in cpx = 0.08). Dashed line shows the variation in $D_{Nd}^{cpx.opx}$ with composition (Na in cpx range from 0.04-0.14) at a constant temperature. Symbols as in Figure 3.4a.

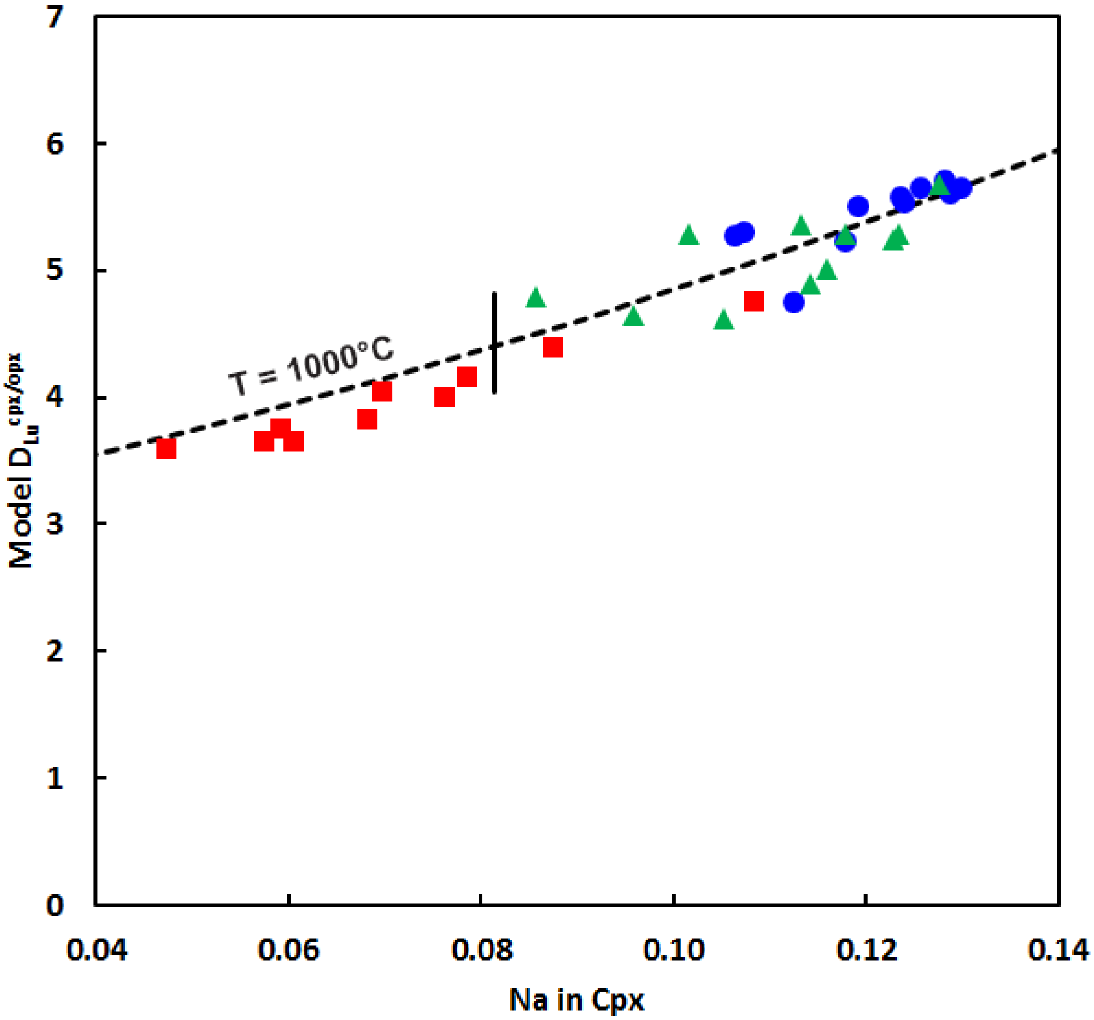

Figure 3.4c Plot of model $D_{Lu}^{cpx/opx}$ versus molar Na content in cpx

> $D_{Lu}^{cpx.opx}$ is modeled following the formulation of Witt-Eickschen and O'Neill (2005). Solid black line shows the variation in $D_{Lu}^{cpx.opx}$ with temperature (950-1050°C) at a fixed composition. Dashed line shows the variation in $D_{Lu}^{cpx.opx}$ with composition at a constant temperature (1000°C). Symbols as in Figure 3.4a.

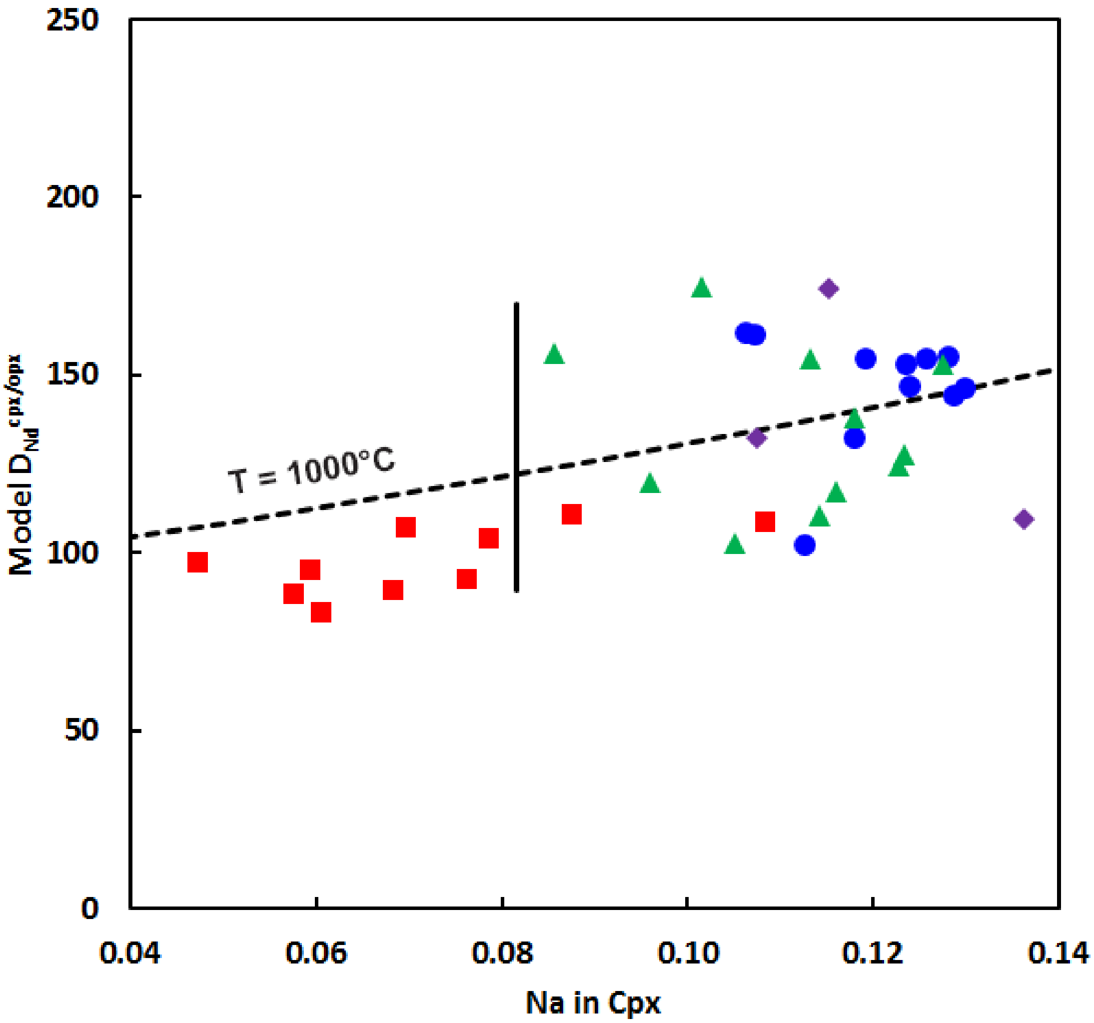

Figure 3.4d Plot of model $D_{Nd}^{cpx/opx}$ versus molar Na content in cpx

> $D_{Nd}^{cpx.opx}$ is modeled following the formulation of Witt-Eickschen and O'Neill (2005). Solid black line shows the variation in $D_{Nd}^{cpx.opx}$ with temperature (950-1050°C) at a fixed composition. Dashed line shows the variation in $D_{Nd}^{cpx.opx}$ with composition at a constant temperature (1000°C). Symbols as in Figure 3.4a.

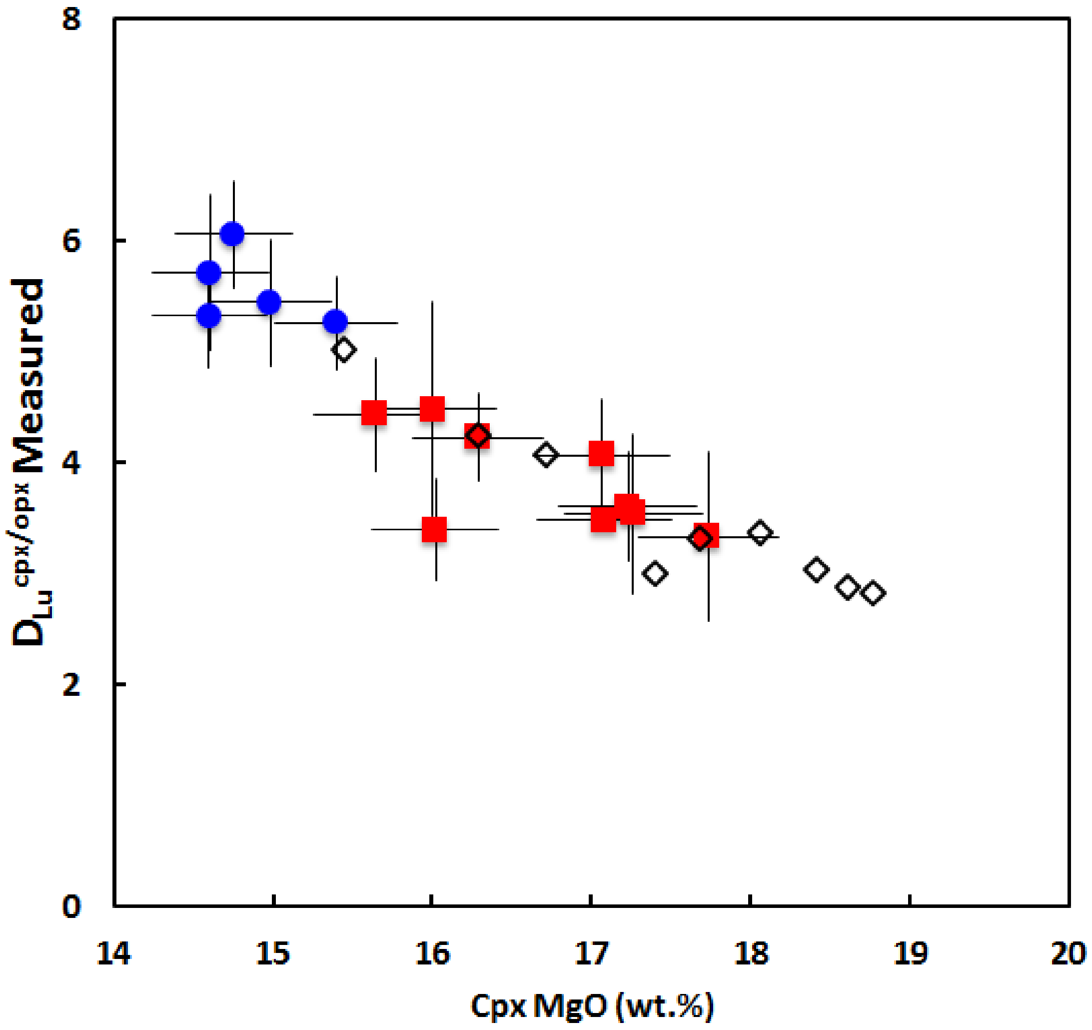

Figure 3.5a Plot of $D_{Lu}^{cpx/opx}$ versus MgO (wt. %) in cpx.

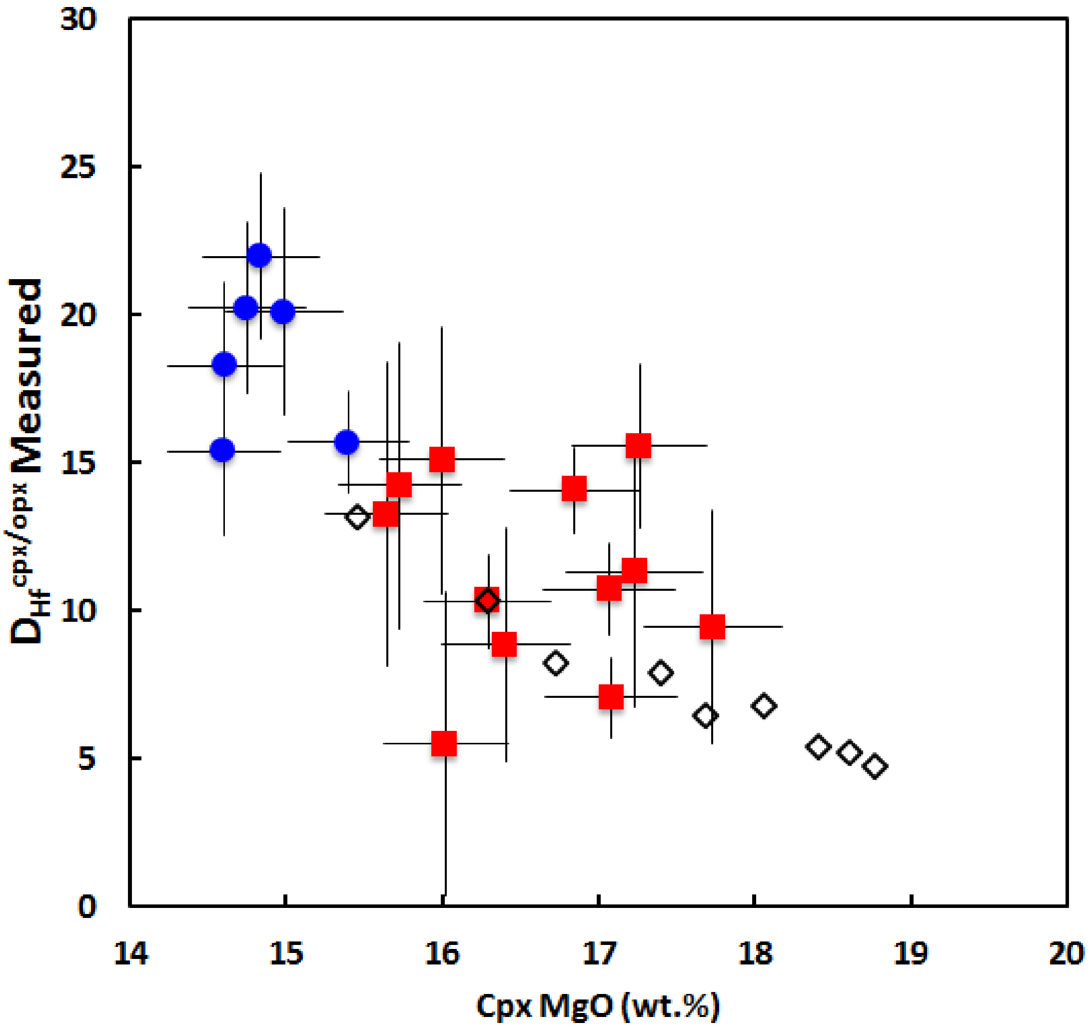

Figure 3.5b Plot of $D_{Nd}^{cpx/opx}$ versus MgO (wt. %) in cpx.

3.4.2 Incompatible trace element budget in spinel peridotites

The incompatible trace element budget of our samples can be constrained by comparing the trace element composition of the bulk xenoliths with those of their constituent minerals relative to their modal abundances. Mineral modes were estimated using a least squares regression of olivine, orthopyroxene, clinopyroxene and spinel major element compositions to the bulk xenolith compositions. These are shown in Table 3.3. In some xenoliths from Elephant Butte, there is a small amount (<1%) of interstitial glass present. The interstitial glass is not included in the modal analysis. Other than the interstitial glass and trace sulfides that are present in the samples, we did not identify any phases via petrographic analysis other than olivine, orthopyroxene, clinopyroxene, and spinel. Clinopyroxene and orthopyroxene trace element abundances were measured by LA-ICP-MS whereas olivine trace element compositions were estimated using the $D^{cpx/olivine}$ model of Witt-Eickschen and O'Neill (2005). Although $D^{cpx/olivine}$ are typically high ($D_{Lu}^{cpx/olivine}$ ranges from 30-50, $D_{Yb}^{cpx/olivine}$ ranges from 50-90), olivine/cpx ratios are sufficiently high that olivine hosts several percent of the total HREE. Spinel is not included because it is not likely to contribute significant amounts of REE, Zr, or Hf due to its low modal abundance (1-3% in our samples) coupled with the extremely low concentrations (typically <10 ppb) of these elements in spinel (Bedini et al., 1997; Eggins et al., 1998; Harvey et al., 2012). From this point forward we refer to the sum of the cpx, opx, and olivine trace element compositions weighted to their modal abundances as the "model whole rock" composition.

	Olivine	OPX	CPX	Spinel	Sum	ssq residuals
07EB1.01	60.3	20.6	17.7	2.1	100.6	0.09
07EB1.05	63.4	14.1	19.2	2.4	99.0	0.05
07EB2.03	54.6	30.7	12.4	3.7	101.4	0.15
07EB4.01	51.9	29.8	16.9	2.8	101.4	0.03
07EB4.05	53.5	28.1	16.7	2.2	100.5	0.17
07EB4.21	57.3	29.3	13.2	2.4	102.3	0.08
07EB1.11	71.6	22.8	3.0	0.9	98.3	0.07
CC07-1-06	56.7	32.2	6.8	4.0	99.6	0.87
CC07-1-09	67.3	12.8	15.9	3.9	99.9	0.10
CC07-1-14	65.9	25.9	7.8	1.2	100.9	0.01
CC07-1-20	56.2	36.5	6.7	1.5	100.9	0.02
CC07-1-22	66.3	20.8	11.9	1.6	100.7	0.59
CC07-1-35	59.1	25.2	11.9	2.2	98.4	0.15
CC07-1-51	65.3	24.8	9.4	0.9	100.5	2.15
CC07-2-01	62.0	26.3	10.1	1.8	100.2	0.13
CC07-3-01	69.4	16.1	12.9	1.6	100.1	0.03

Table 3.3 Mineral modal abundances of samples from this study

Figures 3.6a and 3.6b show clinopyroxene, orthopyroxene, bulk-xenolith, and model whole-rock compositions for two different samples. In the asthenosphere-derived samples (e.g. 07EB4.01, Figure 3.6a) the measured bulk composition is commonly within error of the model whole rock for the MREE-HREE. However, for the LREE, HFSE (Zr, Hf), and LILE (Sr) the model whole-rock concentration is less than the bulk-xenolith concentration. In the lithosphere-derived samples (e.g. CC07-2-01, Figure 3.6b) the model whole rock composition typically accounts for only 60-75% of the REE and only 20-40% of Zr and Hf. These large deficits in REE and HFSE require an additional phase (or phases) to host a significant quantity of these elements in the bulk xenolith. High field strength element deficits are greater than deficits in similarly compatible REE and LREE deficits are larger than M-HREE deficits. This indicates that the residual component is LREE enriched but also enriched in HFSE relative to REE.

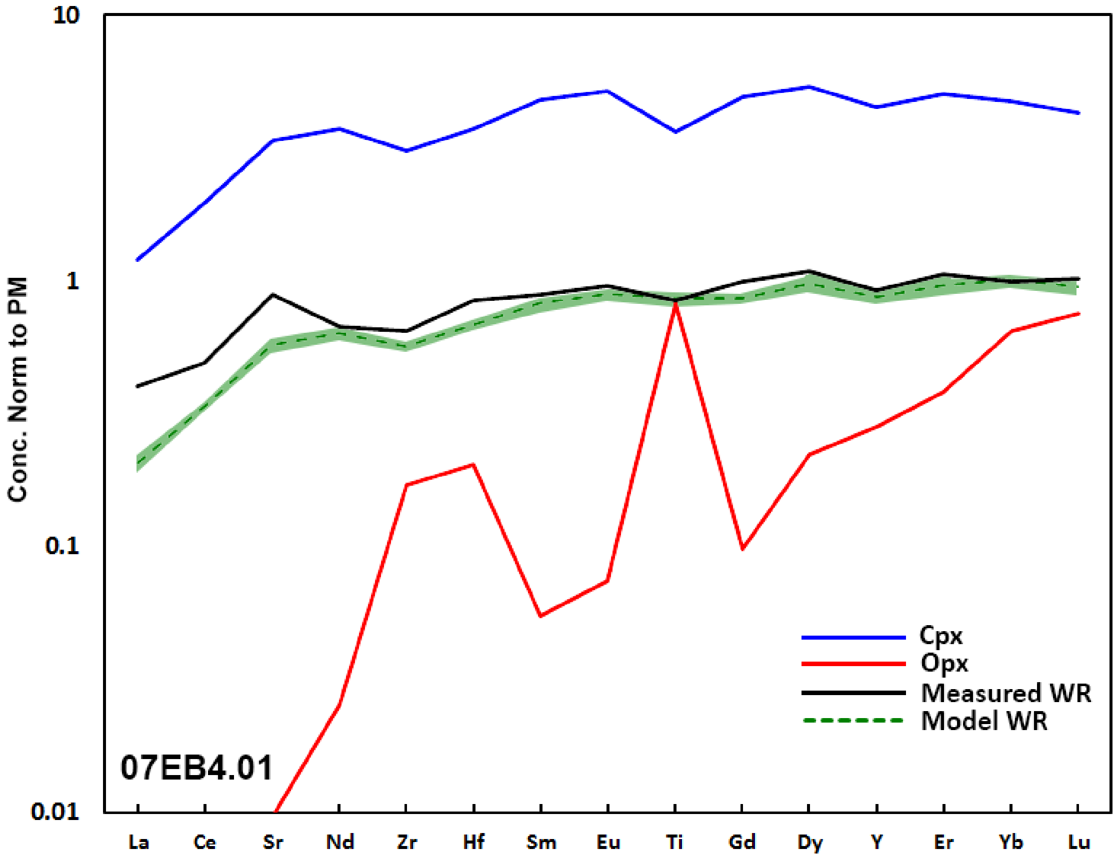

Figure 3.6a Comparison of clinopyroxene, orthopyroxene, whole rock, and model whole rock trace element concentrations for sample 07EB4.01

Concentrations normalized to primitive mantle (McDonough and Sun, 1995). Blue line, cpx; red line, opx; black line, measured whole rock; dashed green line, model whole rock. Green field shows error in model whole rock composition.

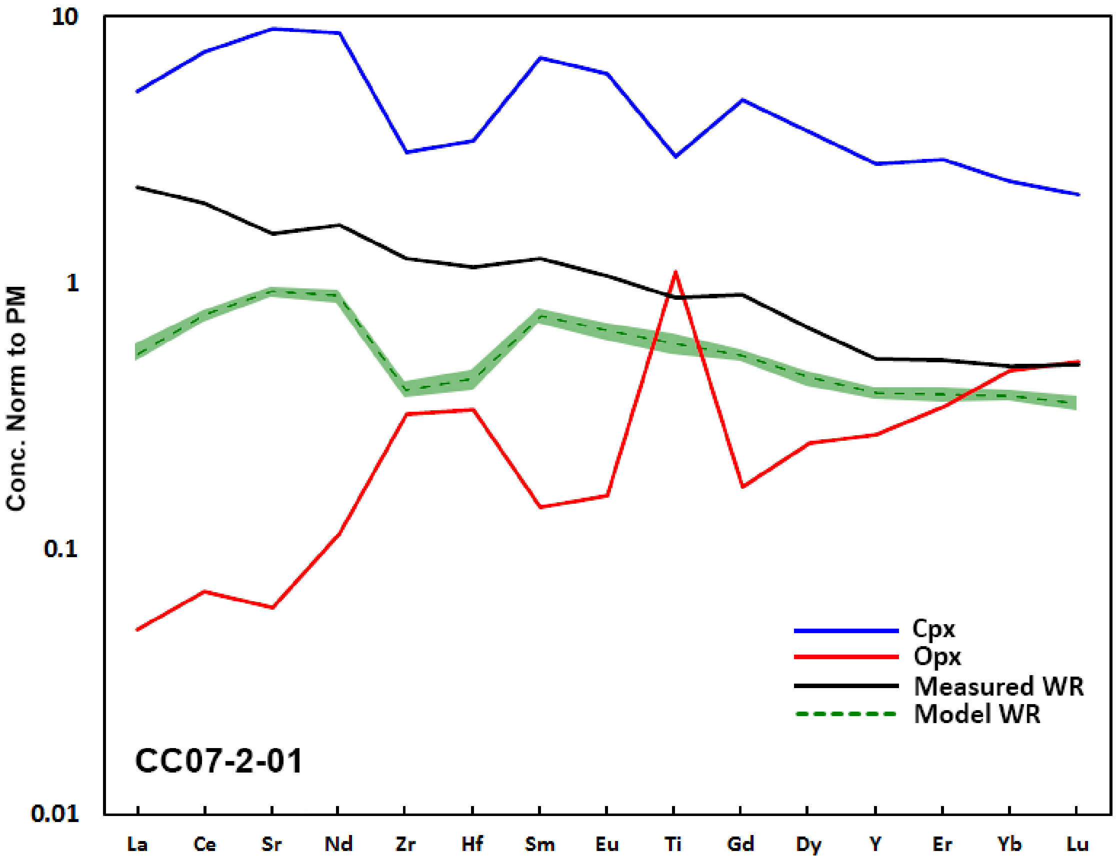

Figure 3.6b Comparison of clinopyroxene, orthopyroxene, whole rock, and model whole rock trace element concentrations for sample CC07-2-01

Concentrations normalized to primitive mantle (McDonough and Sun, 1995). Blue line, cpx; red line, opx; black line, measured whole rock; dashed green line, model whole rock. Green field shows error in model whole rock composition.

Deficits between model whole rock trace element compositions and bulk-xenolith trace element compositions are commonly observed in peridotite xenoliths and generally attributed to a catch-all "grain-boundary component" (Bedini and Bodinier, 1999; Condie et al., 2004; Garrido et al., 2000; Harvey et al., 2012; Kalfoun et al., 2002). The fact that the residual component in the lithosphere-derived samples is enriched in HFSE relative to REE is problematic because typical metasomatic melts/fluids are either depleted in HFSE relative to REE or show "normal" HFSE/LILE ratios (e.g. not HFSE enriched). Apatite (O'Reilly and Griffin, 2000) and amphibole (Eggins et al., 1998) are LREE-enriched and are often observed as secondary phases in peridotite xenoliths. The large deficits in Hf and Zr relative to the REE cannot, however, be explained by presence of apatite/amphibole alone. Instead, a phase that is strongly enriched in HFSE relative to REE must be present. Bodinier et al. (1996) observed reaction layers on spinel consisting of phlogopite and Ti-oxides that host a large (>50%) proportion of the bulk xenolith's HFSE despite the extremely low abundance of these phases. Kalfoun et al. (2002) found rutile and Ti-oxides in off-craton xenoliths from SE Siberia with very high concentrations of Zr and Hf (> 10,000ppm and >200ppm, respectively). Rutile that is found in spinel peridotites, however, typically occurs in fine grained aggregates associated with feldspar and secondary olivine (Ionov et al., 1999), which we do not observe in our samples.

Samples that have been metasomatised ($[La/Sm]_N > 1$) generally have greater deficits in the modeled vs. observed HFSE compared to unmetasomatised samples ($[La/Sm]_N < 1$), consistent with a metasomatic origin for the HFSE deficits (Figure 3.7). The measured whole rock trace element patterns are generally smooth and lack the pronounced depletions in HFSE relative to REE that are present in the model whole rock trace element patterns. This suggests that the observed deficits in HFSE are not related the addition of an exotic component. Instead, the enrichments in HFSE relative to REE in the grain boundary component could be the result of the introduction of a relatively "normal" metasomatic component at the grain boundary followed by diffusion of REE and HFSE at different rates into the mineral structure. Several studies suggest that HFSE diffusion rates are at least an order of magnitude lower than REE diffusions rates (Cherniak et al., 1997a, b; Van Orman et al., 2001). A recent study by Cherniak and Liang (2012), however, suggests that Ti diffuses in Cr-diopside at a rate similar to HREE, but at least one to two orders of magnitude slower than divalent major elements such as Fe, Mg, and Ca. Zirconium and Hf likely diffuse at a slower rate than Ti because they have larger ionic radii than Ti. If an enriched metasomatic component is introduced to the grain boundary and allowed to sufficient time to diffuse, the more slowly diffusing elements (e.g. Zr and Hf) will be preferentially enriched closer to the grain boundary relative to the more rapidly diffusing REE.

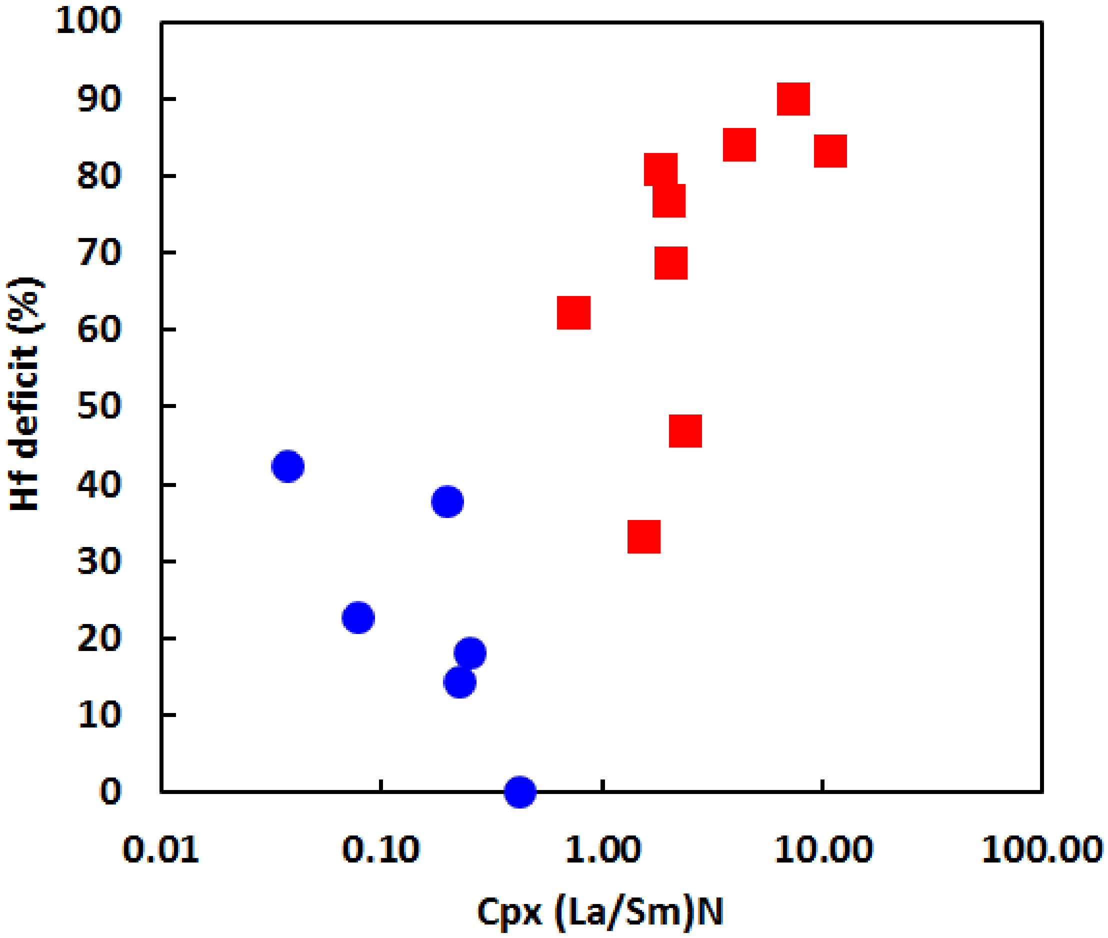

Figure 3.7 Plot of the deficit in Hf model whole rock compositions versus $(La/Sm)_N$ in cpx

X-ray maps of samples with large HFSE deficits in the model trace element compositions show high concentrations of Ti along grain boundaries, consistent with the presence of a HFSE-rich grain boundary component (Figure A7.2a). This Ti-rich grain boundary is not present in samples with good agreement between modeled and measured HFSE compositions (Figure A7.2b). The sample CC07-2-01, which shows high concentrations of Ti along its grain boundaries, also displays a gradient of high Ti concentrations in cpx near grain boundaries with decreasing Ti concentrations moving towards the core (Figures 3.8a,b). Using the length of the diffusion profile and an estimate diffusivity of Ti it is possible to estimate the time since the introduction of the HFSE-rich grain boundary component (i.e. the timing of metasomatism). Using the relationship $t = x^2/D$, with a diffusion distance of 125µm, and diffusivity of 3.82×10^{-22} m^2/s we estimate a diffusion time of ~1 million years. The diffusivity of Ti was estimated at 1080°C (the equilibration temperature of the sample) following Cherniak and Liang (2012). The error from the estimate of the diffusivity ($\log D_0 = -10.53 \pm 1.55$) results in a range of possibly diffusion times from 40,000 years to 45 million years. The diffusion time would be shorter if the diffusion profile does not represent a radial transect of the cpx grain. The short diffusion time indicates that the introduction of the HFSE-bearing grain boundary component that caused the mismatches between measured whole rock and model whole rock trace element compositions is recent and not related to the long-term evolution of the sample.

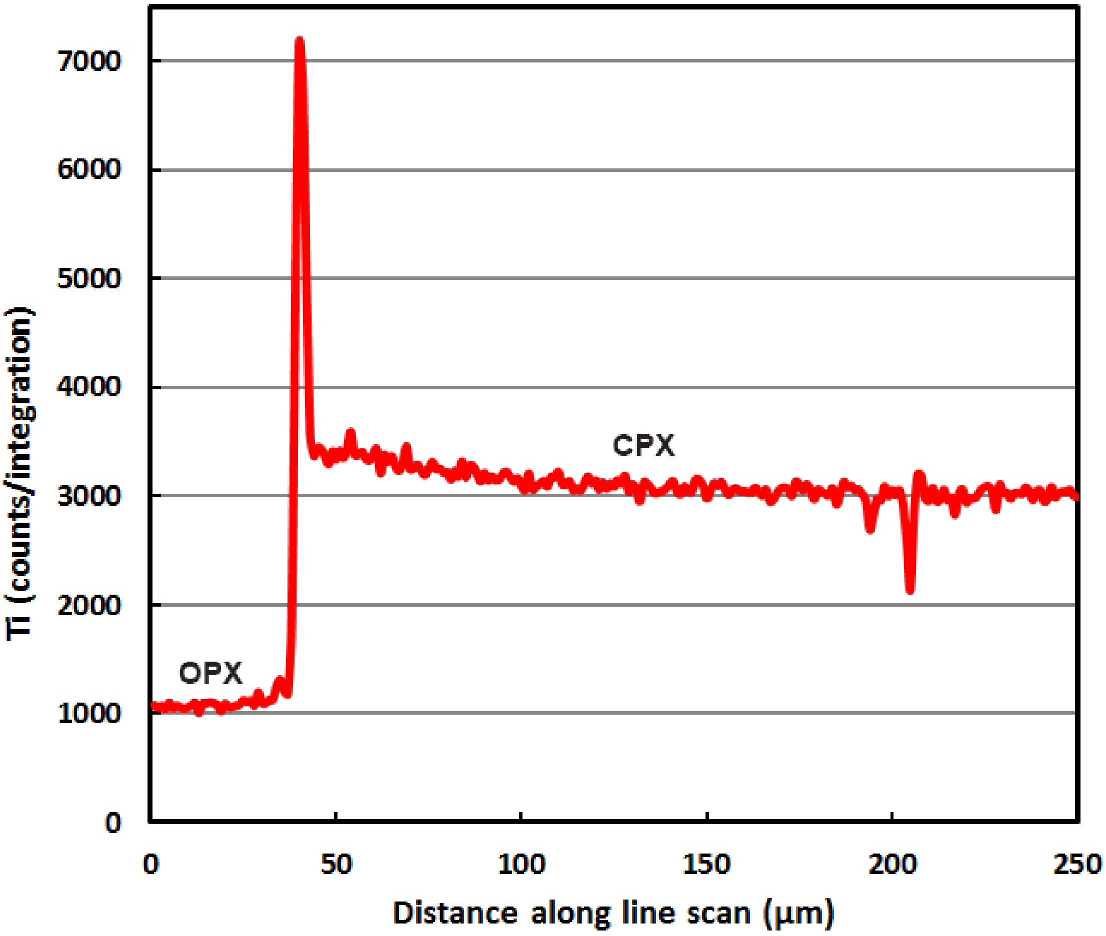

Figure 3.8a X-ray line scan of Ti across cpx-opx grain boundary

Note the high concentrations of Ti in the grain boundary.

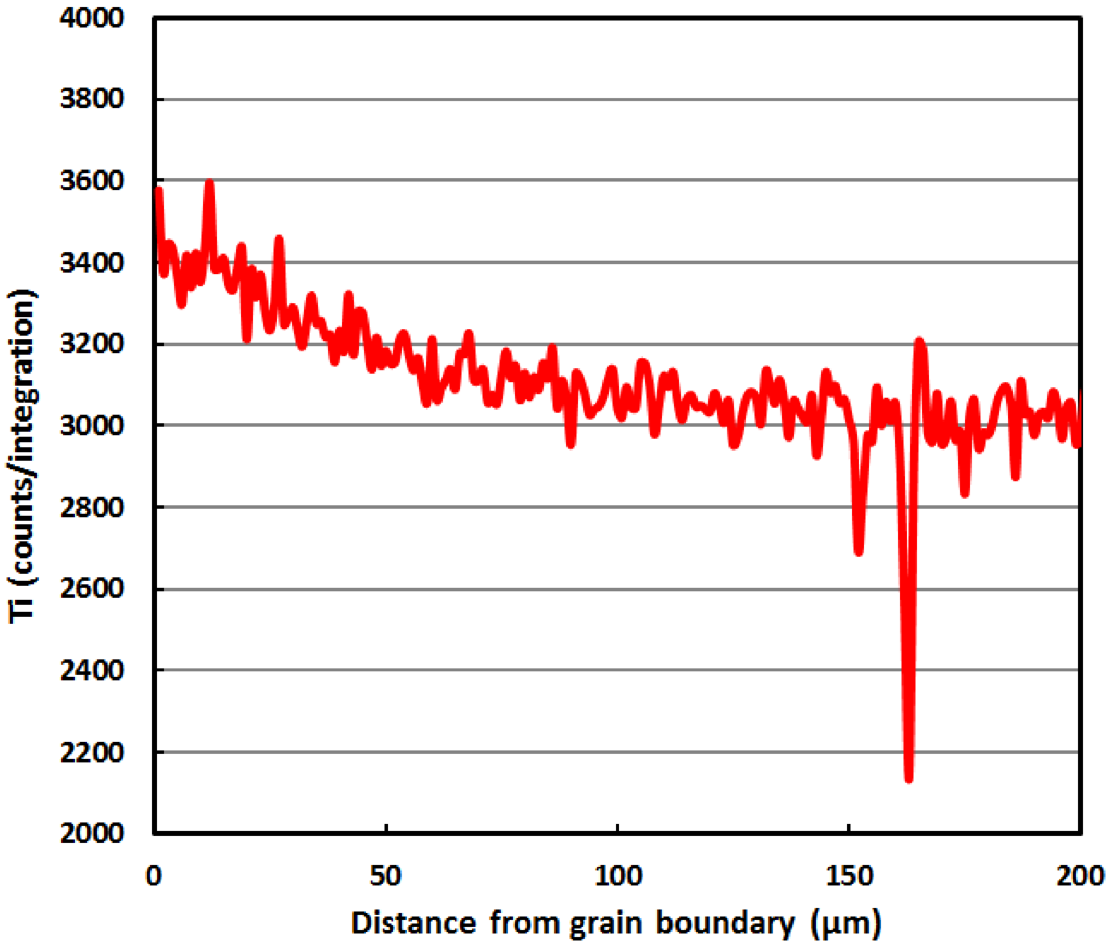

Figure 3.8b X-ray line scan of Ti in a cpx grain

Note the diffusion profile of Ti into the cpx grain from the Ti-rich grain boundary

3.4.3 Comparisons between cpx, opx, and bulk xenolith Nd and Hf isotopes

A general feature of spinel peridotites is that cpx Lu/Hf ratios are lower than opx (and therefore whole rock) Lu/Hf ratios. If a sample has equilibrated below its Lu-Hf closure temperature for an extended period of time then the opx and whole rock ^{176}Hf/^{177}Hf should be systematically more radiogenic than cpx due to their higher Lu/Hf ratios. The same would be expected for ^{143}Nd/^{144}Nd in opx and whole rock because opx (and therefore whole rock) Sm/Nd ratios are higher in cpx. By comparing cpx, opx, and whole rock Nd and Hf isotopes from a single sample, it is therefore possible to determine whether it has equilibrated above or below its closure temperature for these systems.

Figures 3.9a and 3.9b compare Hf and Nd isotopes in the lithosphere- and asthenosphere-derived samples. Orthopyroxene and whole rock Hf and Nd isotopes are consistently either equal to or less radiogenic than cpx Hf and Nd from the same sample. For all samples, $\varepsilon_{Nd,Hf}$ (cpx) is greater than or equal to $\varepsilon_{Nd,Hf}$ (opx) which is greater than or equal to $\varepsilon_{Nd,Hf}$ (WR). Despite the fact that opx and WR values commonly fall below the 1:1 line with cpx, there is a general positive correlation so that samples with more radiogenic cpx Nd and Hf also have more radiogenic opx and WR Nd and Hf. These features suggest that the samples evolved above their closure temperature for Nd and Hf.

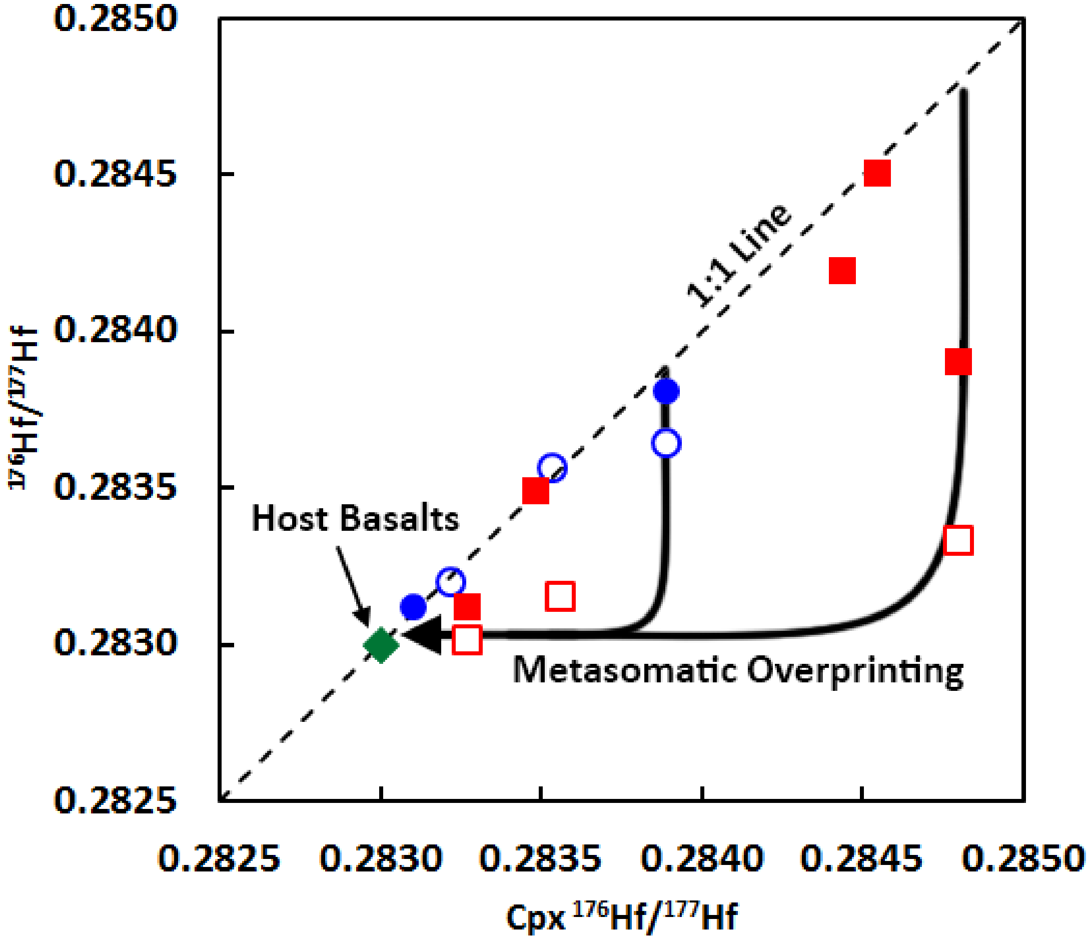

Figure 3.9a Plot of orthopyroxene and whole rock Hf isotopes versus clinopyroxene Hf isotopes

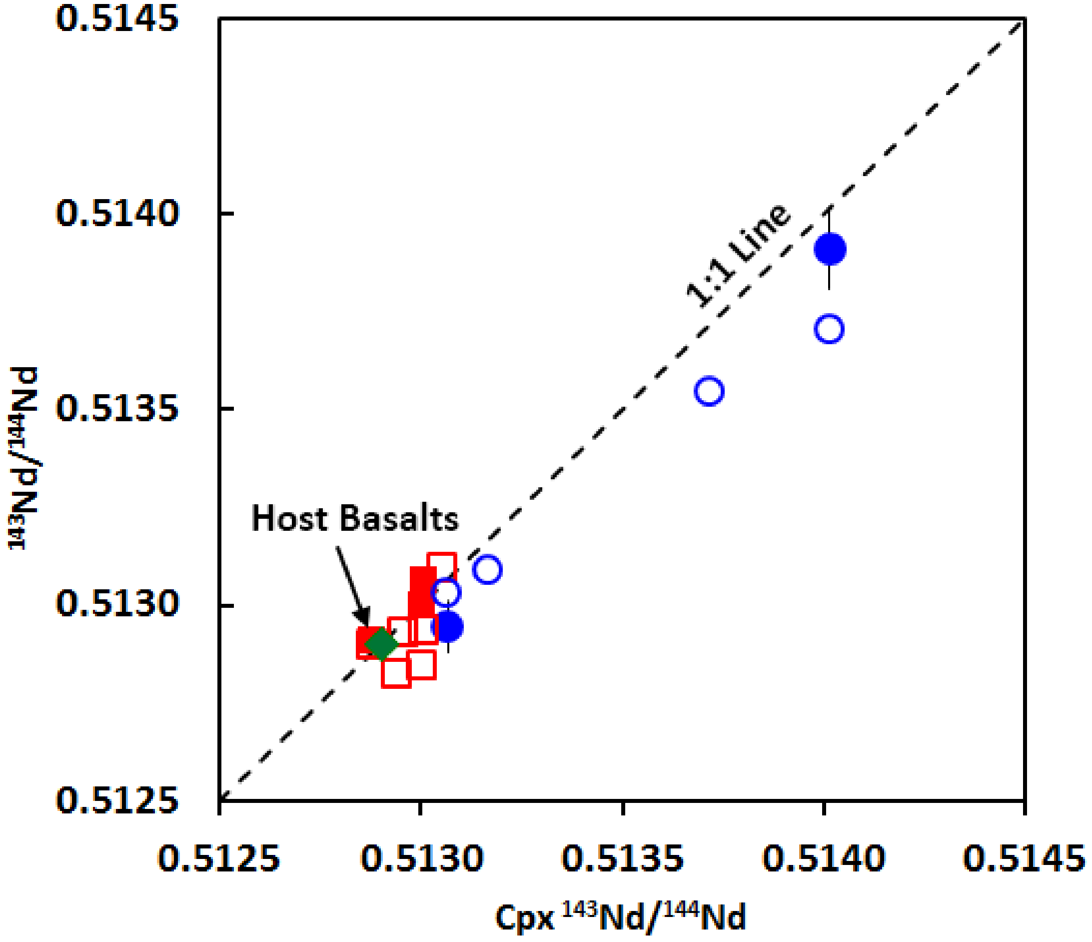

Figure 3.9b Plot of orthopyroxene and whole rock Nd isotopes versus clinopyroxene Nd isotopes

The observation that opx and WR Hf are less radiogenic than cpx Hf is inconsistent with radiogenic ingrowth either above or below the mineral closure temperature. Orthopyroxene has Hf concentrations that are typically 10-20 times lower than in cpx. Therefore, opx is more susceptible to secondary overprinting than cpx. Choi and Mukasa (2012) also observed opx with less radiogenic Hf isotopes than cpx, which they attributed to a late-stage metasomatic agent that primarily over-printed opx Hf isotopes. Asthenosphere-derived samples have similar cpx and opx ε_{Hf} and ε_{Nd}, consistent with the lack of metasomatism recorded in these samples. Two of the lithosphere-derived samples, which have trace element patterns indicative of metasomatic overprinting, have opx Hf isotopes that are less radiogenic than cpx. This indicates that opx Hf isotopes often reflect metasomatic overprinting that is not (or less) apparent in cpx Hf isotopes.

Hafnium isotopes measured on bulk xenolith powders are generally less radiogenic than cpx and opx from the same sample, and trend towards the host basalts (Figure 3.9a). The isotopic compositions of the host basalts overlap with the compositions of other primitive lavas from the region (Johnson and Beard, 1993; McMillan et al., 2000), and can be used as proxies for metasomatising melts that percolate through the lithosphere. The less-radiogenic Hf and Nd compositions that are observed in the whole rocks are likely the result of metasomatic grain boundary components.

There is typically less offset between cpx and opx/WR Nd isotopes than Hf isotopes. This is not expected because $D_{Nd}^{cpx/opx}$ is much greater than $D_{Hf}^{cpx/opx}$ (observed ranges for $D_{Nd}^{cpx/opx}$ and $D_{Hf}^{cpx/opx}$ are 90-260 and 7-22, respectively). Therefore it is expected that opx (and also WR) Nd isotopes would be more susceptible to overprinting than Hf isotopes due to the lower concentrations relative to cpx of Nd in opx compared to Hf. It is possible that the opx and WR Nd isotope composition closely resemble cpx Nd isotopes (i.e. composition prior to metasomatism) due to the efficient removal of Nd grain boundary components from leaching during sample preparation. Hafnium, which is less soluble than Nd, is less likely to be leached during sample preparation that Nd. Therefore opx/WR Hf isotopes may display greater offsets from cpx relative to Nd isotopes due to the persistence of the grain boundary component throughout the sample preparation.

The lithosphere-derived samples originate from mantle that is pervasively metasomatised as evidenced by LREE-enrichment observed in xenoliths from throughout the Rio Grande Rift/Colorado Plateau region (Alibert, 1994; Byerly and Lassiter, 2012; Kil and Wendlandt, 2007; Roden and Shimizu, 1993). Flat-slab subduction of the Farallon plate strongly influenced western North American tectonics during the Laramide orogeny (80-35 Ma; (Humphreys et al., 2003)). Fluids and melts associated with flat-slab subduction are a potential source of the SCLM metasomatism. The lithosphere-derived xenoliths display LREE/LILE enriched metasomatic signatures that are typical of Colorado Plateau xenoliths (Byerly and Lassiter, 2012). The lithosphere-derived Cerro Chato samples samples generally have young (typically < 350 Ma) Nd depleted mantle model ages (Figure A7.3). The depleted mantle model ages represent a maximum estimate for the time of metasomatism, which could be more recent if Nd isotopes reflect mixing instead of radiogenic ingrowth. The young model ages are consistent with the metasomatic signatures that are observed in the lithosphere-derived cpx being related to young (<100 Ma) flat-slab Farallon subduction. The Ti diffusion profile that is observed in a lithosphere-derived Cerro Chato sample (Figure 3.8) requires very recent (<45 Ma) introduction of the metasomatic grain boundary component.

The observed cpx-opx-WR Hf and Nd isotope systematics of our samples results from evolution above their respective Hf and Nd closure temperatures followed by variable resetting of these isotopes by recent metasomatic overprinting. Clinopyroxene is less susceptible to metasomatic overprinting of Hf and Nd than opx (and WR) due to the higher relative concentrations of these elements in cpx. Therefore opx and WR isotopes are less reliable than cpx isotopes for studying the long-term history of a sample. Thus for the remainder of the discussion we focus only on cpx isotopes.

3.4.4 Significance of Lu/Hf – Hf isotope correlations

3.4.4.1 Use of clinopyroxene versus whole rock Lu/Hf ratios

Clinopyroxene Hf isotopes are strongly correlated with both cpx Lu/Hf ratios and model whole rock Lu/Hf ratios (Figure 3.10). Measured whole rock Lu/Hf ratios do not correlate well with cpx Hf isotopes (Figure A7.4). Several studies observe cpx Lu/Hf – cpx Hf isotope correlations in suites of xenoliths and interpret these correlations to be the result variable fractionation of Lu and Hf during ancient melt extraction from the mantle and/or formation of overlying crust (e.g., Choi and Mukasa, 2012; Choi et al., 2008; Choi et al., 2010; Liu et al., 2012). These interpretations are commonly supported by the apparent overlap between whole rock isochron ages (using cpx Lu/Hf) with crust formation ages and/or osmium model ages. However, as illustrated below, it is necessary to reevaluate the way that Lu/Hf – Hf isotope correlations are interpreted and used to estimate ages.

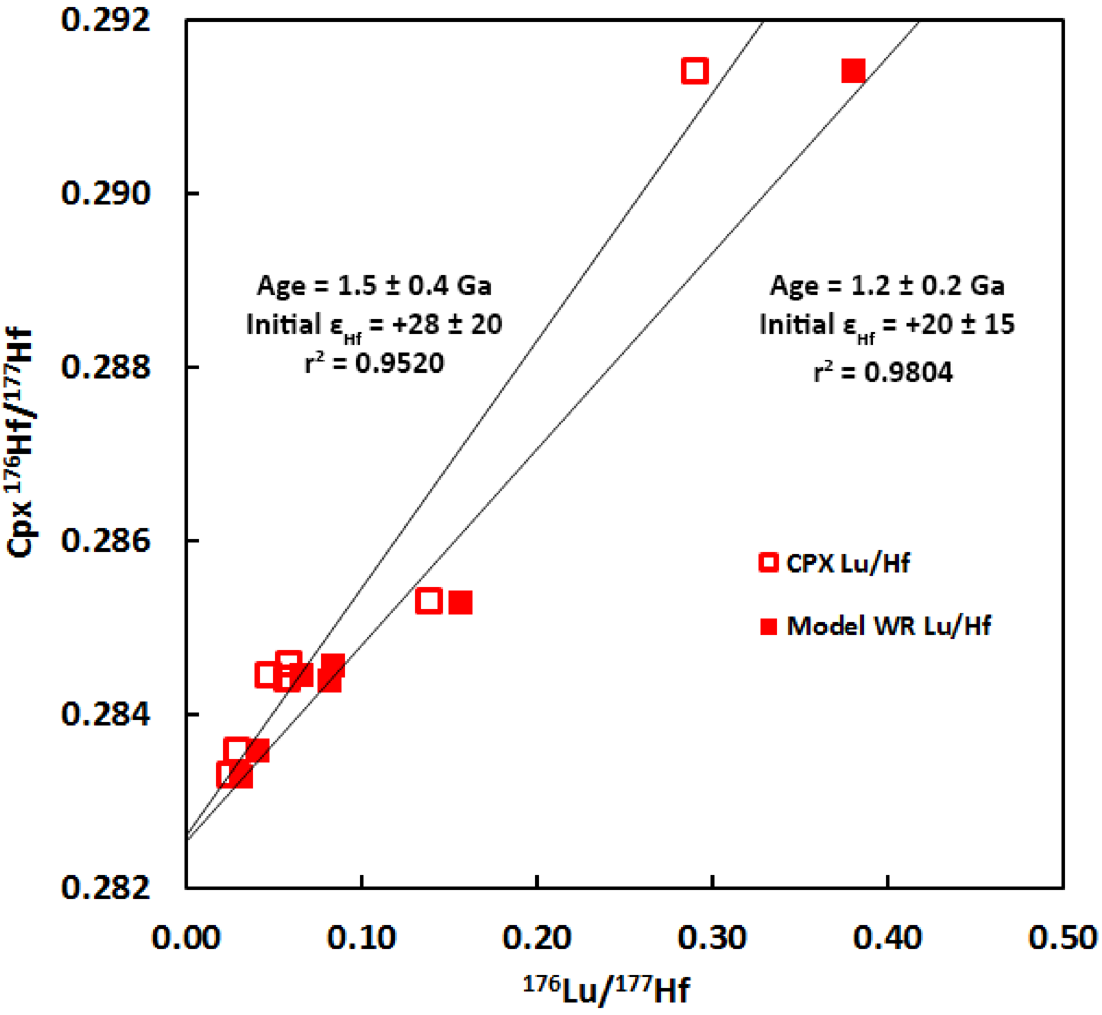

Figure 3.10 Plot of clinopyroxene Hf isotopes versus clinopyroxene Lu/Hf and model whole rock Lu/Hf

Most commonly, cpx Lu/Hf and cpx Hf isotopes are used to infer ages from whole rock isochrons. It is necessary, however, to know the closure temperature for the Lu-Hf system in peridotites in order to know whether the bulk Lu/Hf or the cpx Lu/Hf is controlling cpx ^{176}Hf ingrowth. The Lu-Hf closure temperature has not been tightly constrained but it is likely below the equilibration temperature of most peridotite xenoliths (Bedini et al., 2004). Scherer et al. (2000) found the Lu-Hf closure temperature to be >700°C in large (>1mm) garnets and that the Lu-Hf closure temperature is generally higher than the Sm-Nd closure temperature. Recently, Shu et al. (2014) suggested that closure temperatures for the Sm-Nd and Lu-Hf systems are <850°C and <920°C, respectively, based on comparisons between equilibration temperatures and the difference between eruption age and garnet-cpx isochron ages in eclogite and garnet pyroxenite xenoliths. Our xenoliths which, based on cpx-opx-WR isotope systematics we interpret to have evolved above their closure temperatures, have equilibration temperatures of 950-1100°C. Spinel peridotite xenoliths from other Lu-Hf studies typically have equilibration temperatures that range from 750-1150°C (average ~950±100°C (1 s.d.); (Choi and Mukasa, 2012; Choi et al., 2008; Choi et al., 2010; Chu et al., 2009; Liu et al., 2012; Yu et al., 2009). If the Lu-Hf closure temperature in spinel peridotites is below 950°C as suggested by our data, then a large portion of xenoliths utilized in previous Lu-Hf studies also equilibrated above their Lu-Hf closure temperature.

For samples that have equilibrated above their Lu-Hf closure temperature it is necessary to use whole-rock Lu/Hf ratios when attempting to interpret the age significance of Lu/Hf – Hf isotope correlations in cpx. The model whole rock Lu/Hf ratios correlate much better ($r^2 = 0.980$) with cpx Hf isotopes than the measured whole rock Lu/Hf ratios ($r^2 = 0.384$, Figure A7.4). This is likely due to metasomatic emplacement of grain boundary components, which are responsible for the observed mismatches between measured and model whole rock trace element compositions. Young (<300Ma) Nd depleted mantle model ages coupled with short (<45Ma) Ti diffusion times indicate that the metasomatism that is responsible for the disturbance of measured whole rock Lu/Hf ratios is recent. Because the measured whole rock Lu/Hf is influenced by recent input metasomatic grain boundary components it is not representative of the long-term evolution of samples. Therefore the model whole rock Lu/Hf is preferred over the measured whole rock because it is more robust against secondary overprinting the measured whole rock Lu/Hf.

Model whole rock Lu/Hf ratios are higher than cpx Lu/Hf ratios. This difference tends to be large (40-60%) in very refractory samples (Figure 3.11). This is due the combined effect of the decrease in $D^{cpx/opx}$ as fertility decreases (Figure 3.5) paired with the overall decrease in cpx modal abundance and cpx/opx ratio with increased melt removal (Niu, 1997). Because whole rock Lu/Hf ratios are higher than cpx Lu/Hf ratios, any age determination using cpx Lu/Hf ratios for samples that have equilibrated above their Lu-Hf closure temperature will produce erroneously old ages.

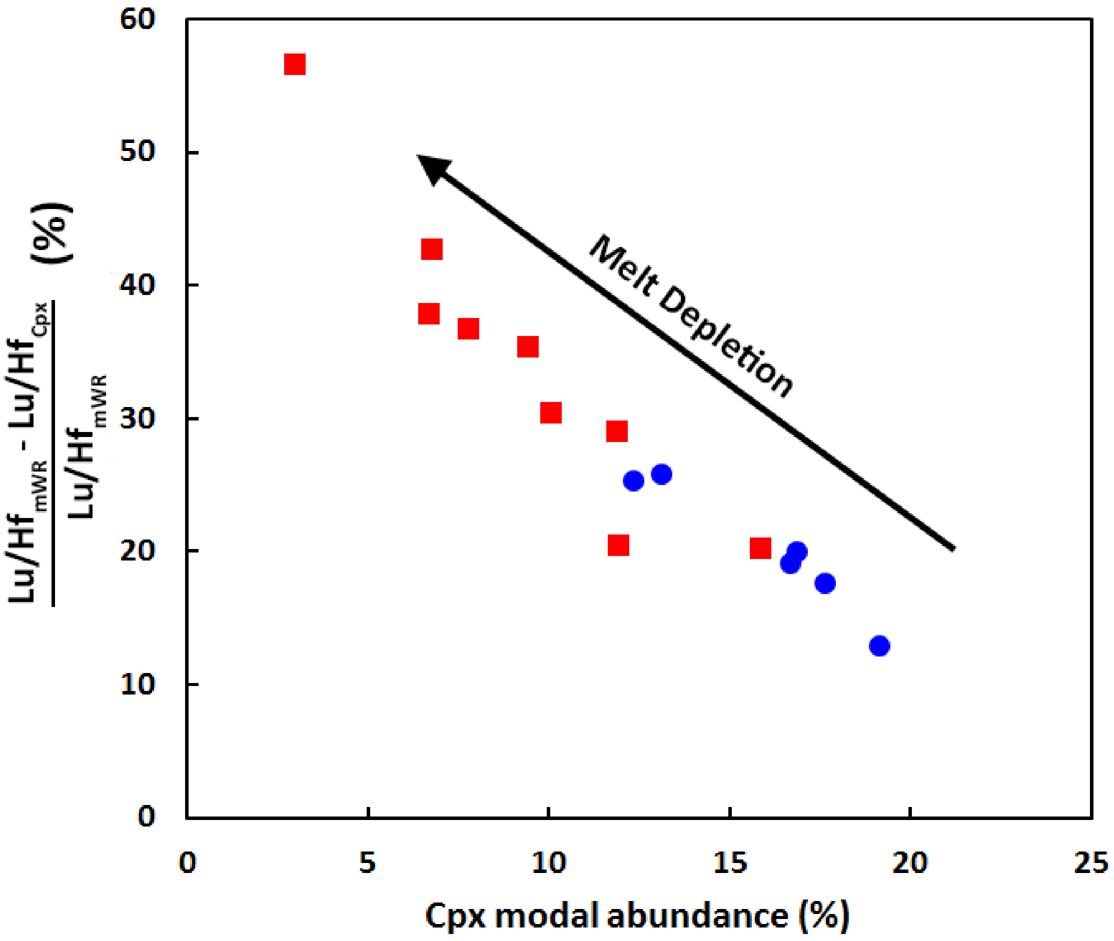

Figure 3.11 Plot of the difference (%) between the model whole rock Lu/Hf ratio and the clinopyroxene Lu/Hf ratio versus clinopyroxene modal abundance

A comparison between the Lu-Hf ages estimated using cpx Lu/Hf versus model whole rock Lu/Hf for the lithosphere-derived samples from Cerro Chato, which are derived from Proterozoic SCLM, is shown in Figure 3.11. The whole rock isochron using cpx Lu/Hf yields an apparent age of ~1.5 Ga whereas the model whole rock Lu/Hf isochron yields an apparent age of ~1.2 Ga. Most studies derive apparent Lu-Hf ages from whole rock isochrons using cpx $^{176}Lu/^{177}Hf$ and $^{176}Hf/^{177}Hf$. Figure A7.5 shows two examples of the comparison between apparent Lu-Hf ages using cpx Lu/Hf versus model whole rock Lu/Hf. Recalculating Lu-Hf ages using the model whole-rock Lu/Hf results in ages that are significantly younger than ages using cpx Lu/Hf.

3.4.4.2 Cause of Lu/Hf – Hf isotope correlations

If Lu-Hf whole rock isochrons reflect the timing of melt extraction from the mantle, then Lu/Hf ratios and Hf isotopes should correlate with indicators of melt depletion, such as whole-rock Al_2O_3, spinel Cr#, or cpx Yb (Dick and Bullen, 1984; Hellebrand et al., 2001). This, however, is not observed for the lithosphere-derived xenoliths from Cerro Chato (Figure 3.12) or for many other suites of xenoliths where whole rock isochrons are interpreted to reflect the timing of mantle melting (Figure A7.6). Thus, in many cases, correlations between Lu/Hf and Hf isotopes do not appear to be the result of variable Lu/Hf fractionation (and subsequent radiogenic Hf ingrowth) during mantle melting.

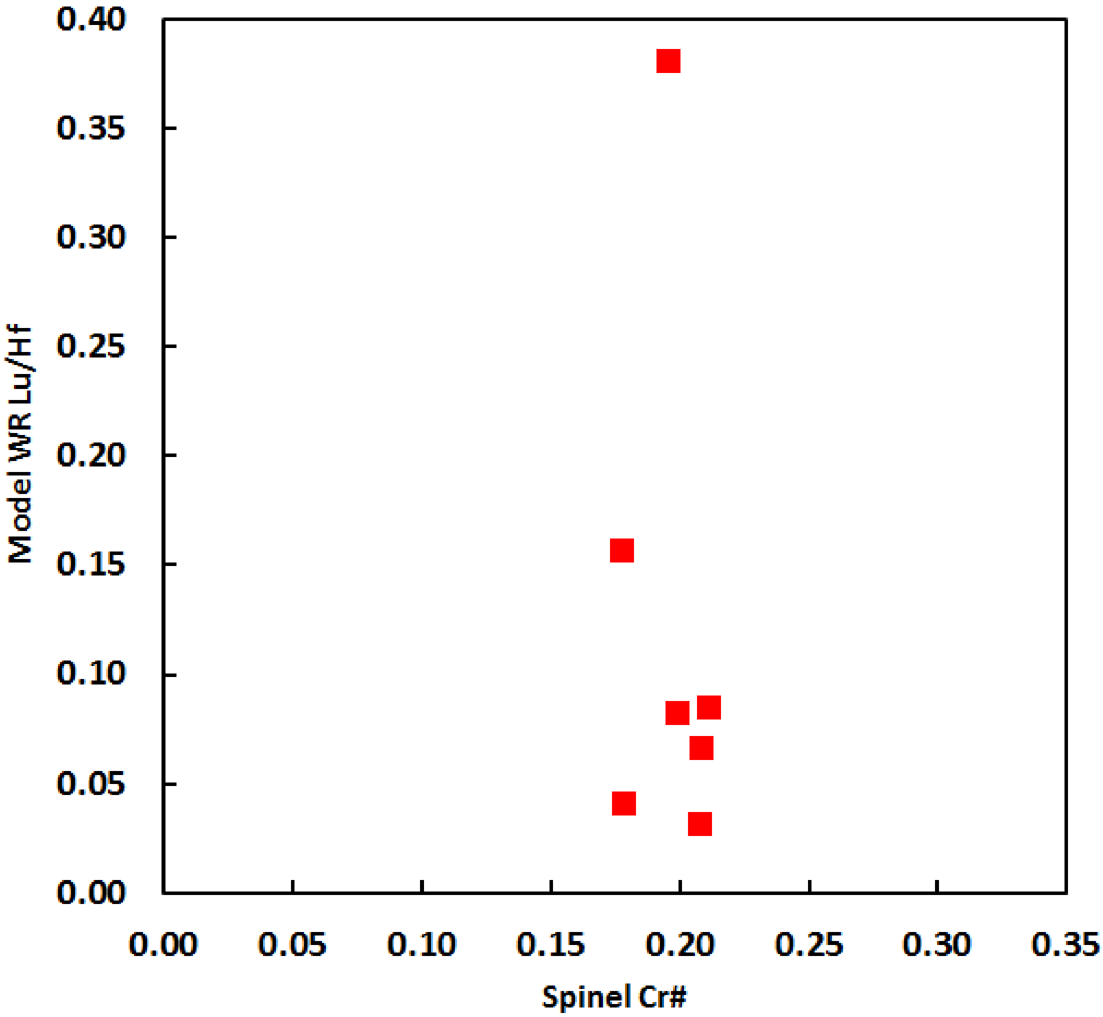

Figure 3.12 Plot of model whole rock Lu/Hf versus spinel Cr#

Spinel Cr# is molar (Cr+Al)/Al.

If Lu/Hf – Hf isotope correlations are not produced by variable mantle melting and subsequent ingrowth, then other mantle processes must be introducing Hf isotope variations that correlate with Lu/Hf ratios. The Cerro Chato samples have cpx Hf isotopes that are strongly correlated with $1/[\mathrm{Hf}]_{\mathrm{Model\ WR}}$ (Figure 3.13a). This could result from radiogenic ingrowth whereby the samples with the lowest initial Hf concentrations inherit the greatest relative proportion of radiogenic Hf from the decay of Lu (i.e. have the most radiogenic Hf isotopes today). However, the correlation could also reflect mixing between depleted and enriched components (i.e. variable metasomatic overprinting of depleted lithospheric mantle). This is consistent with the fact that Cerro Chato cpx have variably LREE/LILE-enriched trace elements that are indicative of metasomatic overprinting. Additionally, the evidence suggests that bulk-xenolith and opx Hf isotopes, which are commonly shifted to less radiogenic values than cpx, are influenced by metasomatic processes as well. This is apparent in correlations between whole rock Hf isotopes and $1/[\mathrm{Hf}]_{\mathrm{Measured\ WR}}$ (Figure 3.13b) as well as opx Hf isotopes and $1/[\mathrm{Hf}]_{\mathrm{Opx}}$ (Figure 3.13c). Thus, the observed correlation between Lu/Hf and Hf isotopes in the Cerro Chato samples may be primarily influenced by variations in Hf that result from variable metasomatic overprinting. The correlation between Lu/Hf and Hf isotopes would therefore have no age significance.

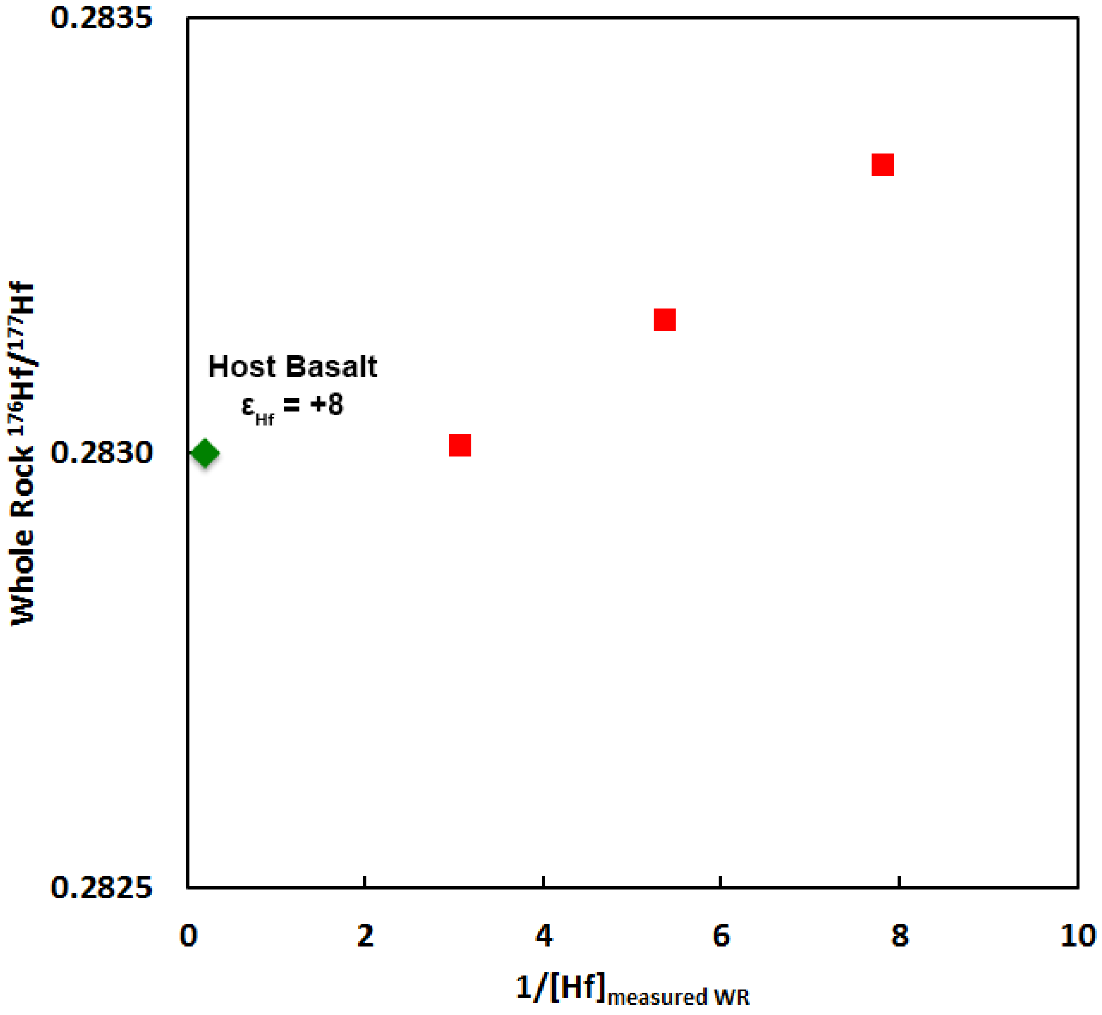

Figure 3.13a Plot of whole rock Hf isotopes versus $1/[Hf]_{whole\ rock}$

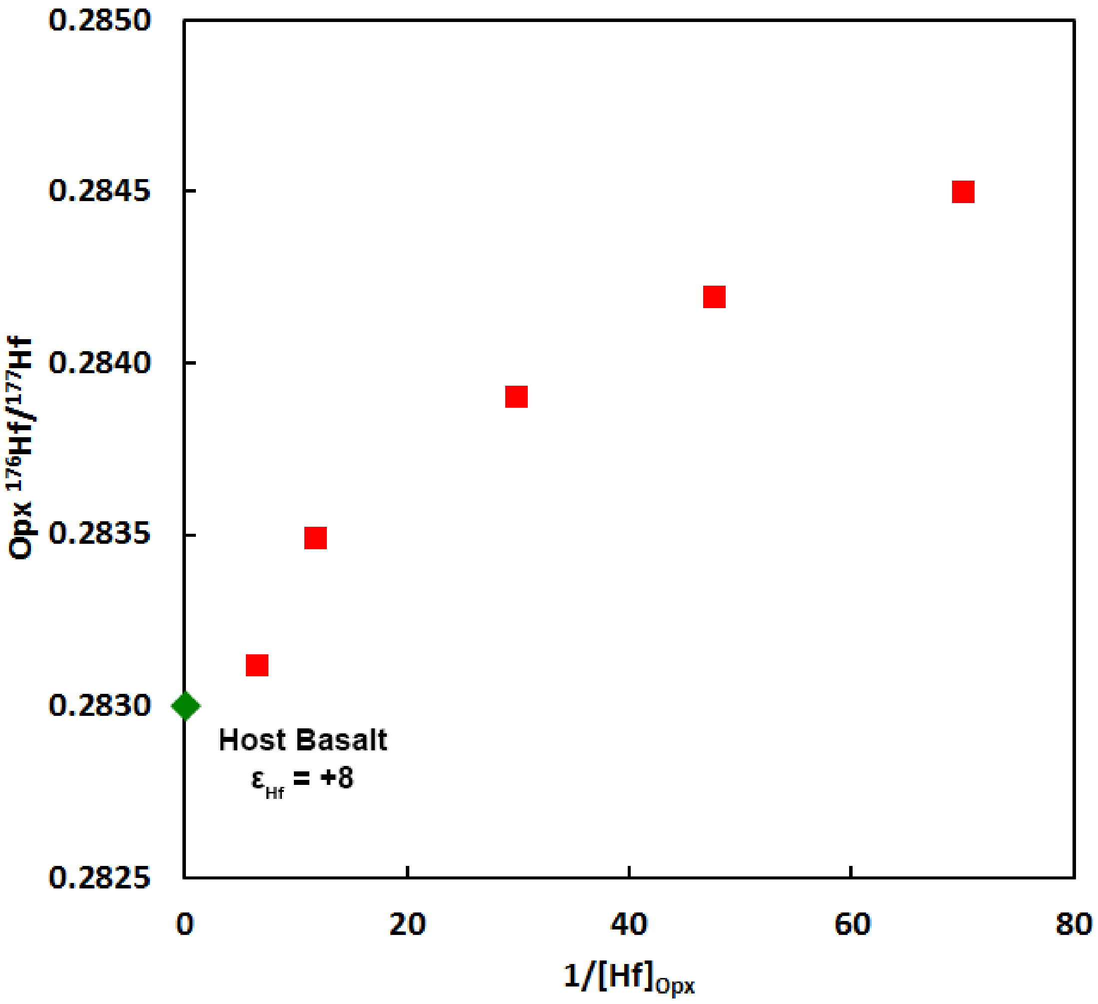

Figure 3.13b Plot of orthopyroxene Hf isotopes versus 1/[Hf]$_{opx}$

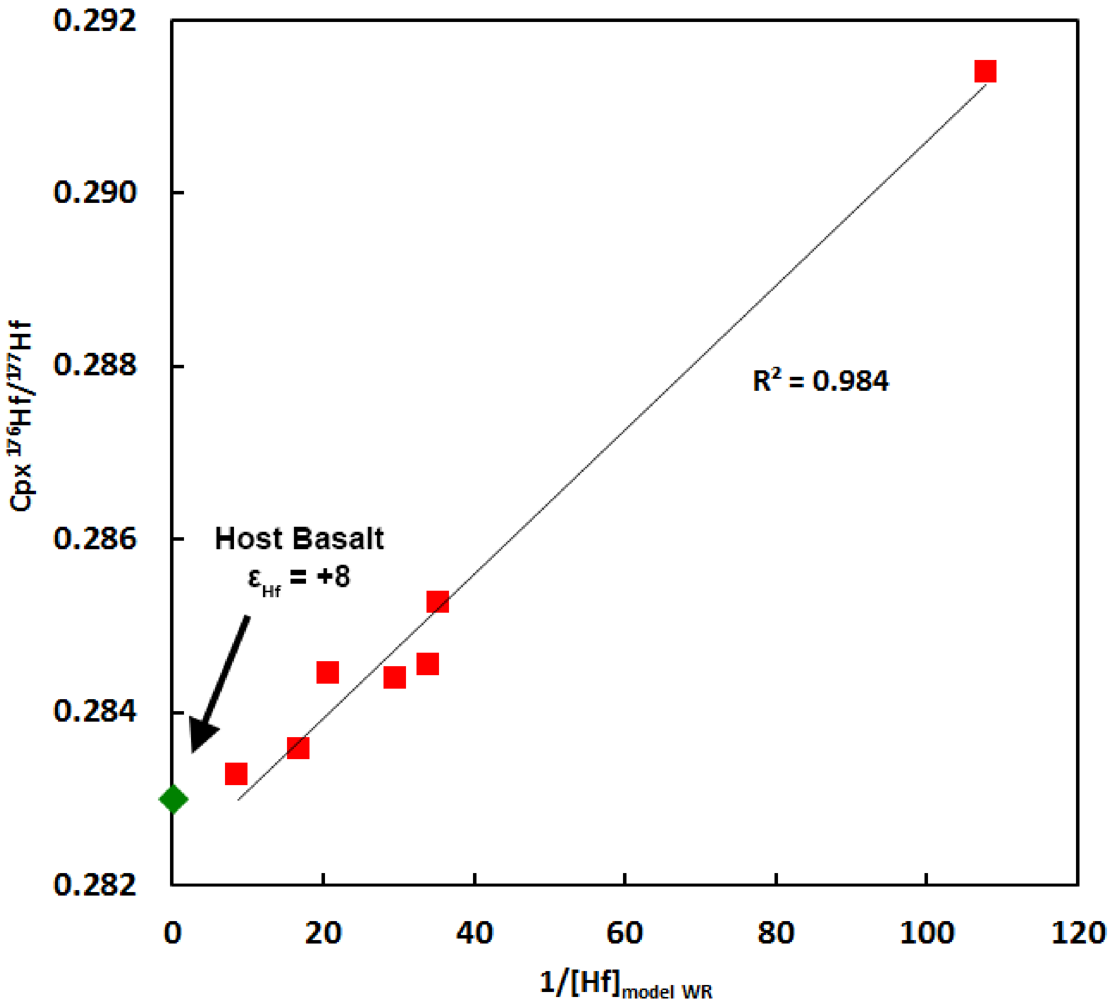

Figure 3.13c Plot of clinopyroxene Hf isotopes versus 1/[Hf]$_{\text{model whole rock}}$

Pervasive metasomatic overprinting of Hf isotopes in SCLM-derived spinel peridotites potentially explains the anomalously high initial ε_{Hf} that are commonly observed in whole rock Lu-Hf isochrons. The initial ε_{Hf} should represent the composition of the SCLM source at t_0, which is generally assumed to be depleted mantle. The Hf isotopic evolution of depleted mantle through time has been estimated by looking at the initial composition of juvenile rocks and/or zircons through time (e.g. Vervoort and Blichert-Toft (1999)). Alternatively one can take the estimated composition of average depleted mantle today (ε_{Hf} ~ +20) and project it back through time to CHUR using an assumed differentiation age or Lu/Hf ratio of depleted mantle. These models broadly agree; for example both estimate the depleted mantle at 2 Ga to have ε_{Hf} of +7 to +10. Several studies have observed Lu-Hf whole rock isochrons with initial ε_{Hf} that are higher than depleted mantle is thought to be at t_0 (e.g. +28±17 at 1.8 Ga (Spitsbergen; Choi et al., 2010), +19±5 at 1.7 Ga (Yangyuan, North China Craton; Liu et al., 2012); +15±4 at 2.6 Ga (Hannuoba, North China Craton; Choi et al., 2008); +20±15 at 1.2 Ga (this study)). However, if Lu/Hf – Hf isotope correlations are the result of mixing and do not have age significance, then the "initial" Hf isotope composition (e.g. y-intercept on whole rock isochron) should represent the enriched (e.g. metasomatic) component not depleted mantle at the apparent t_0.

3.5 CONCLUSIONS

Measured mineral trace element compositions can be used to estimate intercrystalline partitioning in mantle xenoliths. These partition coefficients can be used to infer the trace element budget of bulk xenoliths. Significant differences between model whole rock trace element compositions (the sum of the primary trace element-hosting minerals; olivine, orthopyroxene, and clinopyroxene) and bulk xenolith trace element compositions in many peridotite xenoliths indicate the presence of one or more grain boundary components that are strongly enriched in LREE and HFSE. These grain boundary components are likely related to recent metasomatic processes and are therefore unrelated to the long-term history of the xenoliths. When these grain-boundary components are ignored it is apparent that orthopyroxene and, to a lesser extent, olivine host significant amounts of the whole rock Lu and Hf. This is especially so in refractory samples. Orthopyroxene and olivine have higher Lu/Hf ratios than cpx. Thus, whole-rock Lu/Hf ratios are also higher than cpx Lu/Hf ratios.

Despite having higher Lu/Hf than cpx, opx in several suites of peridotite xenoliths has Hf isotopes that are equivalent to or less radiogenic than cpx Hf isotopes from the same sample despite the fact that opx Lu/Hf is higher than cpx Lu/Hf. This indicates that cpx and opx have equilibrated above the Lu-Hf closure temperature. Orthopyroxenes with less radiogenic Hf than cpx probably reflect metasomatic enrichment of Hf that is not (or less) apparent in cpx. Samples that have cpx and opx with equivalent Hf isotopes have equilibration temperatures of 1000-1030°C indicating that the Lu-Hf closure temperature is <1000°C. Therefore, Lu-Hf whole rock isochrons that include samples with equilibration temperatures >1000°C should use the whole rock Lu/Hf ratio. Use of cpx Lu/Hf ratios in whole rock isochrons for samples that have equilibrated above their Lu-Hf closure temperature will produce erroneously old ages because cpx Lu/Hf ratios are lower than whole rock Lu/Hf ratios. In SCLM-derived samples, hafnium isotopes and Lu/Hf ratios do not generally correlate with indicators of melt depletion. This indicates that Lu/Hf – Hf isotope correlations that are observed in many xenoliths suites today are not produced by ancient melt depletion. Instead Lu/Hf – Hf isotope correlations may reflect variable metasomatic enrichment of depleted lithospheric mantle.

Appendix 1: Bulk xenolith major and trace element compositions of RGR xenoliths

Sample	**07EB1.01**	**07EB1.05**	**07EB1.11**	**07EB1.11d**	**07EB2.03**	**07EB4.01**
Group	**I**	**I**	**I**	**I**	**I**	**I**
Type	**F**	**F**	**R**	**R**	**F**	**F**
SiO_2	44.70	43.07	43.09	42.87	45.01	45.51
TiO_2	0.13	0.12	0.01	0.01	0.11	0.17
AlO_3	3.58	3.59	1.18	1.16	4.57	4.42
FeO*	8.26	8.48	8.01	7.99	8.09	8.22
MnO	0.15	0.18	0.13	0.13	0.13	0.14
MgO	39.24	38.64	43.78	44.20	39.23	37.66
CaO	3.72	3.94	0.93	0.93	2.75	3.61
Na_2O	0.25	0.19	0.00	0.00	0.21	0.27
K_2O	0.03	0.00	0.00	0.00	0.01	0.01
P_2O_5	0.02	0.02	0.01	0.01	0.01	0.02
Sum	100.09	98.24	97.14	97.30	100.12	100.02
La	0.32	0.21	0.15	0.16	0.25	0.26
Ce	0.73	0.66	0.33	0.35	0.56	0.82
Pr	0.11	0.12	0.04	0.04	0.10	0.15
Nd	0.59	0.65	0.14	0.13	0.52	0.84
Sm	0.23	0.25	0.03	0.03	0.23	0.36
Eu	0.11	0.10	0.01	0.01	0.10	0.15
Gd	0.35	0.37	0.04	0.03	0.36	0.54
Tb	0.08	0.07	0.01	0.01	0.07	0.11
Dy	0.56	0.50	0.04	0.04	0.51	0.74
Ho	0.12	0.11	0.01	0.01	0.11	0.16
Er	0.35	0.32	0.02	0.03	0.33	0.46
Tm	0.05	0.05	0.00	0.01	0.05	0.07
Yb	0.33	0.31	0.04	0.05	0.33	0.44
Lu	0.06	0.05	0.01	0.01	0.05	0.07
Ba	11.40	10.80	33.07	31.90	2.55	6.51
Th	0.05	0.02	0.03	0.05	0.02	0.02
Nb	0.41	0.24	0.29	0.29	0.12	0.16
Y	3.05	2.84	0.24	0.24	2.91	3.95
Hf	0.14	0.17	0.03	0.03	0.15	0.24
Ta	0.02	0.01	0.01	0.01	0.00	0.01
U	0.12	0.73	0.06	0.07	0.03	0.01
Pb	0.11	0.35	0.26	0.05	0.11	0.07
Rb	0.35	0.17	0.31	0.32	0.15	0.18
Cs	0.02	0.02	0.03	0.03	0.01	0.01
Sr	33.86	45.55	13.51	13.56	8.64	17.63
Sc	12.89	11.87	7.54	7.45	13.46	15.94
Zr	4.89	5.74	1.03	1.32	5.06	6.80

[a] Major elements in weight percent, trace elements in parts per million.
Samples 07EB1.11 and CC07-1-35 were run in duplicate.

Sample	**07EB4.05**	**07EB4.21**	**BELB 4-30**	**BELB 5-5**	**BELB 5-8**	**BELB 9-8**
Group	**I**	**I**	**I**	**I**	**I**	**I**
Type	**F**	**F**	**R**	**F**	**F**	**F**
SiO_2	45.51	45.60	38.64	40.54	43.42	43.04
TiO_2	0.14	0.08	0.05	0.11	0.15	0.08
Al_2O_3	3.92	3.62	2.29	3.88	4.50	3.34
FeO*	8.94	8.01	7.80	8.64	8.98	8.00
MnO	0.15	0.13	0.23	0.14	0.14	0.13
MgO	37.76	39.86	35.16	34.74	37.23	38.44
CaO	3.54	2.95	8.10	6.70	3.65	2.98
Na_2O	0.26	0.16	0.15	0.27	0.31	0.17
K_2O	0.01	0.00	0.01	0.01	0.03	0.01
P_2O_5	0.02	0.01	0.02	0.02	0.02	0.01
Sum	100.26	100.43	92.45	95.04	98.44	96.20
La	0.46	0.10	1.00	0.26	0.22	0.08
Ce	1.16	0.23	1.84	0.50	0.68	0.18
Pr	0.17	0.04	0.20	0.09	0.12	0.02
Nd	0.90	0.26	0.75	0.50	0.73	0.06
Sm	0.34	0.16	0.18	0.23	0.32	0.01
Eu	0.13	0.07	0.07	0.10	0.14	0.00
Gd	0.47	0.24	0.28	0.38	0.49	0.01
Tb	0.10	0.06	0.05	0.08	0.10	0.00
Dy	0.66	0.46	0.34	0.59	0.70	0.01
Ho	0.14	0.11	0.08	0.13	0.16	0.00
Er	0.42	0.30	0.23	0.38	0.45	0.01
Tm	0.06	0.05	0.03	0.06	0.07	0.00
Yb	0.39	0.31	0.24	0.38	0.43	0.01
Lu	0.06	0.05	0.04	0.06	0.07	0.00
Ba	3.99	1.96	5.29	1.62	3.44	0.14
Th	0.07	0.03	0.06	0.02	0.04	0.02
Nb	0.28	0.10	0.42	0.29	0.32	0.66
Y	3.57	2.58	2.63	3.31	3.93	0.07
Hf	0.22	0.10	0.08	0.16	0.22	0.04
Ta	0.01	0.00	0.02	0.00	0.00	0.00
U	0.02	0.01	0.37	0.28	0.16	0.16
Pb	0.17	0.04	0.26	0.11	0.25	0.07
Rb	0.33	0.30	0.79	0.54	0.98	0.59
Cs	0.01	0.01	0.08	0.02	0.02	0.01
Sr	15.03	3.29	43.63	16.93	13.58	14.72
Sc	14.13	13.46	10.68	14.56	16.51	4.56
Zr	6.92	2.25	3.14	5.63	7.10	3.79

Sample	BELB 9-15	CC07-1-04	CC07-1-06	CC07-1-09	CC07-1-14	CC07-1-20
Group	I	I	I	I	I	I
Type	R	-	-	-	-	-
SiO_2	40.95	41.62	43.97	43.57	45.12	46.11
TiO_2	0.00	0.01	0.098	2.93	0.04	0.02
Al_2O_3	0.65	0.82	3.64	7.30	2.24	2.52
FeO*	7.82	8.16	9.21	0.12	8.15	7.37
MnO	0.11	0.12	0.151	41.23	0.13	0.12
MgO	47.49	49.77	40.01	3.78	42.68	41.70
CaO	0.74	0.10	1.74	0.06	1.94	1.85
Na_2O	0.00	0.00	0.08	0.04	0.05	0.00
K_2O	0.00	0.00	0.00	0.00	0.02	0.00
P_2O_5	0.00	0.01	0.016	0.02	0.01	0.01
Sum	97.78	100.63	98.92	99.05	100.36	99.71
La	0.08	0.47	0.45	0.65	0.63	0.58
Ce	0.18	0.84	1.22	1.74	1.33	1.06
Pr	0.02	0.09	0.18	0.25	0.17	0.11
Nd	0.06	0.27	0.82	1.01	0.63	0.35
Sm	0.01	0.03	0.20	0.24	0.13	0.05
Eu	0.00	0.01	0.08	0.07	0.04	0.01
Gd	0.01	0.03	0.23	0.26	0.13	0.05
Tb	0.00	0.01	0.04	0.05	0.03	0.01
Dy	0.01	0.03	0.28	0.37	0.17	0.11
Ho	0.00	0.01	0.06	0.08	0.04	0.03
Er	0.01	0.02	0.17	0.27	0.13	0.09
Tm	0.00	0.00	0.02	0.04	0.02	0.02
Yb	0.01	0.02	0.16	0.27	0.14	0.11
Lu	0.00	0.00	0.03	0.04	0.02	0.02
Ba	0.14	2.99	1.83	4	4.37	1.23
Th	0.02	0.10	0.04	0.05	0.04	0.05
Nb	0.66	0.29	0.24	0.20	0.16	0.34
Y	0.07	0.15	1.49	2.25	1.02	0.71
Hf	0.04	0.03	0.19	0.06	0.06	0.03
Ta	0.00	0.02	0.02	0.01	0.01	0.02
U	0.16	0.04	0.02	0.03	0.02	0.02
Pb	0.07	0.09	0.10	0.12	0.57	0.07
Rb	0.59	0.14	0.11	0.2	0.38	0.16
Cs	0.01	0.00	0.00	0.01	0.01	0.01
Sr	14.72	3.74	10.91	39	18.08	30.34
Sc	4.56	2.46	9.77	13.1	10.92	12.29
Zr	3.79	1.77	6.85	2	2.69	1.17

Sample	CC07-1-22	CC07-1-23	CC07-1-24	CC07-1-26	CC07-1-29	CC07-1-35
Group	I	II	I	I	I	I
Type	-	-	-	-	-	-
SiO_2	44.32	44.77	43.37	43.10	40.27	44.08
TiO_2	0.02	0.281	0.051	0.069	1.09	0.03
Al_2O_3	2.45	4.49	3.24	2.53	7.86	3.10
FeO*	7.65	9.88	9.27	8.93	0.12	7.83
MnO	0.12	0.158	0.142	0.130	49.78	0.12
MgO	41.82	32.57	39.87	42.60	0.46	40.94
CaO	2.77	7.64	2.36	2.44	0.01	2.56
Na_2O	0.06	0.39	0.15	0.12	0.01	0.09
K_2O	0.00	0.02	0.00	0.00	0.00	0.01
P_2O_5	0.01	0.019	0.009	0.014	0.01	0.02
Sum	99.23	100.22	98.47	99.94	99.60	98.78
La	0.53	1.04	0.49	0.45	0.16	1.21
Ce	0.92	2.73	1.08	1.27	0.30	2.76
Pr	0.10	0.42	0.13	0.19	0.03	0.33
Nd	0.33	2.18	0.53	0.90	0.12	1.26
Sm	0.07	0.73	0.15	0.22	0.04	0.22
Eu	0.02	0.28	0.06	0.08	0.01	0.08
Gd	0.08	0.90	0.19	0.27	0.04	0.20
Tb	0.02	0.16	0.04	0.04	0.01	0.04
Dy	0.20	0.99	0.27	0.28	0.04	0.23
Ho	0.05	0.20	0.06	0.06	0.01	0.05
Er	0.15	0.51	0.18	0.16	0.03	0.16
Tm	0.03	0.07	0.03	0.02	0.01	0.03
Yb	0.18	0.41	0.19	0.16	0.04	0.18
Lu	0.03	0.06	0.03	0.03	0.01	0.03
Ba	8.66	4.65	1.84	1.33	1	3.45
Th	0.07	0.09	0.08	0.05	0.04	0.08
Nb	0.20	0.62	0.19	0.18	0.10	0.45
Y	1.26	4.85	1.56	1.47	0.28	1.40
Hf	0.04	0.41	0.07	0.11	0.03	0.12
Ta	0.01	0.04	0.02	0.01	0.01	0.04
U	0.03	0.03	0.03	0.01	0.02	0.03
Pb	0.06	0.19	0.10	0.10	0.05	0.12
Rb	0.11	0.43	0.10	0.14	0.0	0.24
Cs	0.01	0.02	0.00	0.01	0.01	0.01
Sr	28.10	25.92	12.26	16.46	4	40.65
Sc	12.08	23.04	11.75	10.52	5.2	10.66
Zr	1.61	11.89	3.27	3.56	1	7.52

Sample Group Type	CC07-1-35r I -	CC07-1-51 I -	CC07-2-01 I -	CC07-3-01 I -
SiO_2	44.36	44.28	45.14	43.08
TiO_2	0.02	0.03	0.18	0.10
Al_2O_3	2.86	2.46	2.73	2.18
FeO*	7.51	9.78	8.78	10.54
MnO	0.12	0.15	0.14	0.16
MgO	40.24	40.06	40.58	41.14
CaO	2.82	2.24	2.16	2.94
Na_2O	0.09	0.10	0.22	0.09
K_2O	0.01	0.00	0.05	0.00
P_2O_5	0.02	0.01	0.04	0.01
Sum	98.05	99.11	100.00	100.24
La	1.28	0.35	1.49	0.27
Ce	3.01	0.89	3.35	0.81
Pr	0.36	0.12	0.45	0.13
Nd	1.34	0.47	2.07	0.67
Sm	0.25	0.11	0.50	0.22
Eu	0.08	0.04	0.16	0.09
Gd	0.21	0.11	0.49	0.32
Tb	0.04	0.02	0.08	0.05
Dy	0.26	0.15	0.46	0.34
Ho	0.06	0.03	0.09	0.07
Er	0.18	0.11	0.23	0.20
Tm	0.03	0.02	0.03	0.03
Yb	0.20	0.14	0.21	0.18
Lu	0.03	0.02	0.03	0.03
Ba	2.28	2.18	19.57	2.17
Th	0.10	0.06	0.16	0.04
Nb	0.35	0.10	1.81	0.13
Y	1.56	0.96	2.24	1.71
Hf	0.17	0.04	0.32	0.13
Ta	0.04	0.01	0.12	0.01
U	0.04	0.02	0.06	0.01
Pb	0.22	0.08	0.12	0.06
Rb	0.16	0.15	0.58	0.13
Cs	0.00	0.01	0.01	0.00
Sr	43.97	18.69	30.64	10.22
Sc	11.65	11.41	10.60	11.98
Zr	8.82	1.91	13.02	3.62

Appendix 2: Clinopyroxene major and trace element compositions of RGR xenoliths

Sample	07EB1.01	07EB1.05	07EB1.06	07EB1.09	07EB1.10	07EB1.11
Group	I	I	I	I	I	I
Type	F	F	R	F	F	R
SiO_2	51.42	51.12	52.90	50.87	50.65	52.36
Al_2O_3	7.32	7.69	4.03	7.58	7.41	4.04
FeO	3.02	2.97	2.38	2.91	2.98	2.51
MnO	0.11	0.11	0.09	0.08	0.08	0.07
MgO	15.40	14.60	17.07	14.60	14.87	16.85
CaO	19.55	19.63	21.03	19.33	19.70	21.29
Na_2O	1.60	1.83	0.82	1.85	1.68	0.86
Cr_2O_3	0.88	0.77	1.36	0.68	0.72	1.24
TiO_2	0.43	0.66	0.05	0.62	0.51	0.05
NiO	0.07	0.03	0.08	0.04	0.07	0.04
Sum	99.80	99.42	99.80	98.55	98.67	99.31
Ti	2464	3405	369	3956	3429	444
Sr	35.2	58.2	20.5	77.4	33.2	22.1
Y	15.0	17.7	3.3	20.5	19.1	4.1
Zr	17.1	27.2	3.4	36.2	19.1	4.4
Nb	0.039	0.044	1.054	-	-	-
La	0.15	1.06	1.077	0.88	0.31	1.18
Ce	1.06	3.21	2.190	3.91	1.60	2.14
Nd	2.24	3.61	1.047	4.75	3.13	1.17
Sm	1.20	1.57	0.326	1.97	1.58	0.37
Eu	0.52	0.67	0.120	0.78	0.67	0.14
Gd	1.81	2.30	0.416	2.69	2.46	0.51
Dy	2.69	3.13	0.565	3.52	3.36	0.69
Er	1.70	1.97	0.383	2.22	2.14	0.47
Yb	1.62	1.87	0.401	2.03	1.98	0.50
Lu	0.220	0.256	0.058	-	-	-
Hf	0.57	0.83	0.107	1.05	0.85	0.14
Ta	-	0.005	0.122	-	-	-
Pb	-	0.051	0.011	-	-	-
Th	-	0.056	0.109	-	-	-
U	-	0.019	0.027	-	-	-

Sample	07EB1.16	07EB2.03	07EB4.01	07EB4.05	07EB4.06	07EB4.07
Group	I	I	I	I	I	I
Type	F	F	F	F	F	F
SiO_2	51.61	51.36	50.99	51.34	52.06	52.24
Al_2O_3	5.56	7.32	7.57	7.63	7.50	7.08
FeO	3.00	2.78	2.96	2.92	2.85	2.64
MnO	0.08	0.09	0.09	0.09	0.10	0.09
MgO	16.00	14.84	14.61	14.75	14.81	15.10
CaO	20.59	19.94	19.70	19.64	19.67	20.13
Na_2O	1.16	1.82	1.77	1.76	1.74	1.58
Cr_2O_3	1.20	0.82	0.67	0.72	0.73	0.81
TiO_2	0.15	0.52	0.60	0.57	0.65	0.57
NiO	0.04	0.05	0.07	0.05	0.07	0.09
Sum	99.37	99.54	99.03	99.48	100.19	100.33
Ti	-	3448	4379	3498	3528	3254
Sr	-	56.9	67.2	51.5	59.5	40.3
Y	-	20.1	19.3	15.2	18.8	19.1
Zr	-	29.0	32.3	22.2	28.6	18.9
Nb	-	-	0.102	0.009	-	-
La	-	0.59	0.780	0.49	2.06	0.86
Ce	-	2.60	3.302	2.66	5.42	3.01
Nd	-	3.54	4.654	3.71	4.50	3.78
Sm	-	1.63	1.936	1.54	1.72	1.61
Eu	-	0.67	0.795	0.65	0.68	0.67
Gd	-	2.52	2.686	2.15	2.48	2.37
Dy	-	3.48	3.603	2.81	3.32	3.31
Er	-	2.21	2.202	1.74	2.03	2.13
Yb	-	2.05	2.098	1.67	1.92	1.97
Lu	-	-	0.290	0.236	-	-
Hf	-	0.93	1.050	0.74	0.94	0.74
Ta	-	-	0.006	0.001	-	-
Pb	-	-	0.009	0.014	-	-
Th	-	-	0.014	0.011	-	-
U	-	-	0.004	0.006	-	-

Sample	07EB4.13	07EB4.18	07EB4.19	07EB4.21	07EB4.22	BELB 4-1
Group	I	I	I	I	I	I
Type	F	R	R	F	F	F
SiO_2	51.78	52.74	53.39	51.17	51.99	51.25
Al_2O_3	6.92	3.58	3.03	6.61	6.90	6.99
FeO	2.74	2.20	2.35	2.76	2.52	2.88
MnO	0.10	0.07	0.09	0.10	0.11	0.05
MgO	15.02	17.04	17.39	14.99	15.07	14.79
CaO	20.19	22.09	21.36	20.55	20.04	19.88
Na_2O	1.56	0.67	0.76	1.53	1.65	1.62
Cr_2O_3	0.75	1.02	1.21	0.84	0.95	0.84
TiO_2	0.48	0.02	0.13	0.37	0.56	0.54
NiO	0.06	0.08	0.06	0.05	0.03	0.05
Sum	99.59	99.51	99.78	98.96	99.81	98.89
Ti	2822	127	668	2215	2989	3368
Sr	15.6	6.1	47.3	8.9	54.4	68.9
Y	17.7	1.1	3.5	14.1	17.5	15.8
Zr	10.7	0.5	6.4	6.8	24.6	29.1
Nb	-	-	-	0.032	-	-
La	0.07	0.44	2.15	0.06	0.59	0.91
Ce	0.59	0.79	3.83	0.28	2.56	3.76
Nd	2.10	0.24	1.88	1.35	3.48	4.17
Sm	1.26	0.04	0.54	0.92	1.51	1.56
Eu	0.55	0.01	0.20	0.43	0.60	0.64
Gd	2.20	0.04	0.68	1.65	2.30	2.18
Dy	3.09	0.12	0.70	2.49	3.04	2.91
Er	2.02	0.18	0.37	1.60	1.91	1.87
Yb	1.94	0.29	0.34	1.61	1.77	1.73
Lu	-	-	-	0.225	-	-
Hf	0.60	0.01	0.23	0.38	0.79	0.81
Ta	-	-	-	-	-	-
Pb	-	-	-	-	-	0.02
Th	-	-	-	0.019	-	-
U	-	-	-	0.009	-	-

Sample	BELB 4-30	BELB 5-1	BELB 5-5	BELB 5-8	BELB 9-15	BELB 9-6
Group	I	I	I	I	I	I
Type	R	F	F	F	R	F
SiO_2	51.70	51.78	51.46	51.36	53.63	51.51
Al_2O_3	6.37	7.05	7.32	7.43	2.39	7.27
FeO	2.99	2.74	2.86	2.86	2.07	2.79
MnO	0.06	0.05	0.05	0.05	0.04	0.06
MgO	15.33	14.87	14.72	14.63	16.99	14.63
CaO	19.89	20.08	19.60	19.70	21.82	19.71
Na_2O	1.54	1.70	1.80	1.79	0.84	1.75
Cr_2O_3	0.92	0.81	0.80	0.72	1.04	0.86
TiO_2	0.28	0.50	0.51	0.61	0.02	0.51
NiO	0.04	0.04	0.04	0.04	0.03	0.04
Sum	99.12	99.62	99.16	99.20	98.86	99.13
Ti	1618	3015	3183	3897	70	3187
Sr	144.0	20.6	54.4	48.7	67.9	45.2
Y	13.8	15.6	17.3	17.9	0.6	16.1
Zr	27.3	13.6	24.3	26.3	0.5	19.3
Nb	-	-	-	-	-	-
La	8.05	0.07	0.57	0.42	2.82	0.46
Ce	21.71	0.83	2.26	2.42	4.74	1.97
Nd	10.96	2.50	3.11	3.70	1.07	2.90
Sm	2.24	1.34	1.47	1.62	0.13	1.37
Eu	0.86	0.57	0.60	0.66	0.05	0.59
Gd	2.15	2.06	2.23	2.45	0.09	2.14
Dy	2.56	2.90	3.18	3.29	0.08	2.93
Er	1.55	1.89	2.07	2.12	0.08	1.93
Yb	1.51	1.77	1.94	1.98	0.14	1.80
Lu	-	-	-	-	-	-
Hf	0.47	0.64	0.75	0.89	0.02	0.61
Ta	-	-	-	-	-	-
Pb	0.11	0.01	0.01	0.04	0.11	0.02
Th	-	-	-	-	-	-
U	-	-	-	-	-	-

Sample	BELB 9-8	CC07-1-01	CC07-1-04	CC07-1-06	CC07-1-09
Group	I	II	I	I	I
Type	F	-	-	-	-
SiO_2	51.48	50.77	-	52.37	53.25
Al_2O_3	6.69	6.85	-	4.81	3.35
FeO	2.61	4.10	-	3.17	2.24
MnO	0.05	0.13	-	0.11	0.06
MgO	14.84	14.55	-	16.00	17.23
CaO	20.34	21.41	-	21.40	23.22
Na_2O	1.51	0.89	-	0.99	0.32
Cr_2O_3	0.81	0.72	-	0.63	0.33
TiO_2	0.49	0.72	-	0.23	0.06
NiO	0.02	0.05	-	0.05	0.06
Sum	98.84	100.19	-	99.75	100.12
Ti	2932	4221	-	852	461
Sr	17.5	76.8	-	131.9	255.0
Y	15.9	11.0	-	6.2	11.5
Zr	13.5	26.9	-	22.8	8.1
Nb	-		-	1.185	0.181
La	0.08	2.52	-	3.91	3.308
Ce	0.83	7.53	-	12.32	10.746
Nd	2.31	6.14	-	6.52	6.197
Sm	1.29	1.96	-	1.31	1.334
Eu	0.53	0.70	-	0.45	0.462
Gd	1.99	2.28	-	1.09	1.353
Dy	2.86	2.22	-	1.14	1.942
Er	1.87	1.18	-	0.68	1.402
Yb	1.79	0.99	-	0.65	1.310
Lu	-		-	0.093	0.173
Hf	0.62	0.99	-	0.40	0.224
Ta	-		-	0.172	0.021
Pb	0.01		-	0.060	0.459
Th	-		-	0.198	0.069
U	-		-	0.075	0.116

Sample	**CC07-1-14**	**CC07-1-20**	**CC07-1-22**	**CC07-1-23**	**CC07-1-24**	**CC07-1-26**
Group	**I**	**I**	**I**	**II**	**I**	**I**
Type	-	-	-	-	-	-
SiO_2	51.82	52.07	52.57	50.98	52.17	51.67
Al_2O_3	5.82	4.02	4.93	6.65	4.59	5.53
FeO	2.68	2.53	2.70	3.85	2.77	3.34
MnO	0.09	0.09	0.08	0.13	0.07	0.05
MgO	15.64	17.08	16.02	14.86	15.94	16.00
CaO	21.38	22.75	21.36	20.89	21.64	20.10
Na_2O	1.12	0.30	1.25	0.98	1.10	1.08
Cr_2O_3	1.10	0.59	0.56	1.12	0.53	1.04
TiO_2	0.21	0.08	0.18	0.56	0.33	0.34
NiO	0.04	0.05	0.04	0.03	0.07	0.04
Sum	99.71	100.22	99.67	100.03	99.22	99.20
Ti	719	374	494	3309	1078	-
Sr	152.0	378.6	221.7	52.2	109.2	-
Y	6.5	4.7	5.9	9.8	7.9	-
Zr	9.0	1.1	1.7	21.7	10.5	-
Nb	0.399	0.489	0.414	-	-	-
La	2.60	5.143	3.58	1.69	2.68	-
Ce	8.70	8.997	5.49	5.21	6.29	-
Nd	4.39	2.043	1.79	4.60	2.97	-
Sm	0.79	0.297	0.30	1.49	0.78	-
Eu	0.28	0.125	0.12	0.57	0.31	-
Gd	0.77	0.414	0.44	1.84	0.91	-
Dy	1.12	0.776	1.03	1.97	1.33	-
Er	0.80	0.575	0.80	1.09	0.89	-
Yb	0.79	0.573	0.84	0.90	0.90	-
Lu	0.117	0.082	0.127	-	-	-
Hf	0.19	0.037	0.02	0.75	0.19	-
Ta	0.032	0.030	0.023	-	-	-
Pb	0.112	0.114	0.240	-	-	-
Th	0.045	0.423	0.253	-	-	-
U	0.025	0.302	0.101	-	-	-

Sample	**CC07-1-27**	**CC07-1-29**	**CC07-1-33**	**CC07-1-35**	**CC07-1-41**	**CC07-1-51**
Group	**II**	**I**	**II**	**I**	**I**	**I**
Type	-	-	-	-	-	-
SiO_2	47.77	53.76	49.49	52.25	53.03	52.59
Al_2O_3	9.07	2.40	8.22	5.16	3.28	5.65
FeO	4.21	1.94	4.27	2.97	2.52	3.89
MnO	0.12	0.08	0.12	0.09	0.08	0.07
MgO	14.69	17.73	14.31	16.40	17.26	15.72
CaO	19.40	23.71	21.05	21.20	23.04	20.03
Na_2O	1.38	0.20	1.10	0.97	0.29	1.36
Cr_2O_3	0.01	0.35	0.45	0.90	0.23	0.99
TiO_2	1.45	0.11	0.72	0.08	0.10	0.08
NiO	0.04	0.05	0.02	0.04	0.03	0.04
Sum	98.13	100.35	99.75	100.06	99.87	100.43
Ti	-	656	4253	404	596	570
Sr	-	109	54	356	294	196
Y	-	7	11	8	10	7
Zr	-	3	23	29	22	12
Nb	-	0.082	-	-	0.615	-
La	-	2.231	1.49	9.12	5.938	3.98
Ce	-	4.697	4.87	21.33	19.820	9.99
Nd	-	2.779	4.72	8.90	10.633	5.20
Sm	-	0.955	1.62	1.35	1.919	1.03
Eu	-	0.310	0.60	0.42	0.573	0.34
Gd	-	1.235	1.99	0.91	1.579	0.88
Dy	-	1.509	2.23	1.09	1.715	1.17
Er	-	0.874	1.23	0.71	1.127	0.81
Yb	-	0.714	1.11	0.79	1.040	0.80
Lu	-	0.107	-	-	0.152	-
Hf	-	0.145	0.76	0.19	0.207	0.17
Ta	-	0.009	-	-	0.081	-
Pb	-	0.205	-	-	0.532	-
Th	-	0.042	-	-	0.179	-
U	-	0.057	-	-	0.145	-

Sample Group Type	CC07-2-01 I -	CC07-3-01 I -
SiO_2	51.76	50.99
Al_2O_3	6.08	5.76
FeO	3.32	3.57
MnO	0.10	0.06
MgO	16.29	15.79
CaO	19.77	21.25
Na_2O	1.07	0.90
Cr_2O_3	1.30	0.61
TiO_2	0.67	0.45
NiO	0.05	0.04
Sum	100.41	99.43
Ti	3599	3315
Sr	180	60
Y	12	11
Zr	33	20
Nb	1.135	0.485
La	3.419	1.32
Ce	12.325	5.02
Nd	10.815	4.46
Sm	2.862	1.61
Eu	0.946	0.53
Gd	2.643	1.84
Dy	2.504	2.11
Er	1.273	1.22
Yb	1.068	1.12
Lu	0.145	0.150
Hf	0.974	0.70
Ta	0.122	0.030
Pb	0.098	0.111
Th	0.118	0.046
U	0.051	0.022

Appendix 3: Orthopyroxene major and trace element compositions of RGR xenoliths

Sample	**07EB1.01**	**07EB1.05**	**07EB1.06**	**07EB1.09**	**07EB1.10**	**07EB1.11**
Group	**I**	**I**	**I**	**I**	**I**	**I**
Type	**F**	**F**	**R**	**F**	**F**	**R**
SiO_2	54.29	54.27	55.82	53.95	53.86	55.13
Al_2O_3	5.40	5.13	3.49	4.89	4.91	3.37
FeO	6.24	6.55	5.63	6.44	6.47	5.53
MnO	0.14	0.15	0.10	0.16	0.15	0.12
MgO	32.12	32.08	33.83	31.99	32.03	33.16
CaO	0.97	0.81	0.93	0.80	0.83	0.98
Na_2O	0.14	0.13	0.08	0.12	0.11	0.07
Cr_2O_3	0.42	0.35	0.72	0.30	0.30	0.66
TiO_2	0.12	0.13	0.02	0.12	0.12	0.03
NiO	0.10	0.07	0.11	0.08	0.09	0.10
Sum	99.95	99.67	100.74	98.86	98.87	99.16
Ti	636	884	153	-	-	161
Sr	0.116	0.21968272	0.065	-	-	0.273
Y	1.118	1.1668022	0.323	-	-	0.331
Zr	1.184	1.9496717	0.422	-	-	0.401
Nb	0.003	0.00393393	0.069	-	-	-
La	0.000	0.00150749	0.006	-	-	0.001
Ce	0.005	0.01694106	0.012	-	-	0.007
Nd	0.017	0.02839729	0.010	-	-	0.009
Sm	0.016	0.02326491	0.006	-	-	0.003
Eu	0.009	0.01037483	0.003	-	-	0.002
Gd	0.049	0.0563693	0.013	-	-	0.013
Dy	0.138	0.14390263	0.038	-	-	0.035
Er	0.148	0.15619963	0.047	-	-	0.048
Yb	0.242	0.25943774	0.083	-	-	0.089
Lu	0.042	0.04813757	0.014	-	-	-
Hf	0.037	0.05393555	0.010	-	-	0.010

Sample	07EB1.16	07EB2.03	07EB4.01	07EB4.05	07EB4.06	07EB4.07
Group	I	I	I	I	I	I
Type	F	F	F	F	F	F
SiO_2	53.82	54.41	53.93	54.38	-	-
Al_2O_3	4.49	4.84	4.99	5.00	-	-
FeO	8.07	6.37	6.70	6.82	-	-
MnO	0.16	0.16	0.16	0.18	-	-
MgO	31.04	32.45	31.97	32.16	-	-
CaO	1.02	0.77	0.79	0.77	-	-
Na_2O	0.11	0.12	0.11	0.12	-	-
Cr_2O_3	0.63	0.38	0.31	0.33	-	-
TiO_2	0.09	0.11	0.10	0.11	-	-
NiO	0.10	0.11	0.10	0.12	-	-
Sum	99.53	99.72	99.14	99.98	-	-
Ti	-	757	991	731	-	-
Sr	-	0.126	0.193	0.158	-	-
Y	-	1.076	1.211	0.884	-	-
Zr	-	1.448	1.779	1.093	-	-
Nb	-	0.004	0.005	0.003	-	-
La	-	0.001	0.005	0.001	-	-
Ce	-	0.008	0.020	0.010	-	-
Nd	-	0.020	0.032	0.018	-	-
Sm	-	0.017	0.022	0.015	-	-
Eu	-	0.008	0.011	0.008	-	-
Gd	-	0.044	0.053	0.037	-	-
Dy	-	0.121	0.150	0.105	-	-
Er	-	0.149	0.166	0.122	-	-
Yb	-	0.249	0.287	0.212	-	-
Lu	-	0.046	0.051	0.039	-	-
Hf	-	0.042	0.057	0.037	-	-

Sample	**07EB4.13**	**07EB4.18**	**07EB4.19**	**07EB4.21**	**07EB4.22**	**BELB 4-1**
Group	**I**	**I**	**I**	**I**	**I**	**I**
Type	**F**	**R**	**R**	**F**	**F**	**F**
SiO_2	-	55.53	-	54.16	-	-
Al_2O_3	-	3.31	-	4.52	-	-
FeO	-	5.57	-	6.37	-	-
MnO	-	0.14	-	0.16	-	-
MgO	-	33.47	-	32.29	-	-
CaO	-	0.85	-	0.71	-	-
Na_2O	-	0.06	-	0.09	-	-
Cr_2O_3	-	0.59	-	0.40	-	-
TiO_2	-	0.01	-	0.07	-	-
NiO	-	0.11	-	0.11	-	-
Sum	-	99.63	-	98.87	-	-
Ti	-	-	-	503	-	-
Sr	-	-	-	0.113	-	-
Y	-	-	-	0.881	-	-
Zr	-	-	-	0.391	-	-
Nb	-	-	-	0.005	-	-
La	-	-	-	0.001	-	-
Ce	-	-	-	0.006	-	-
Nd	-	-	-	0.013	-	-
Sm	-	-	-	0.011	-	-
Eu	-	-	-	0.007	-	-
Gd	-	-	-	0.035	-	-
Dy	-	-	-	0.102	-	-
Er	-	-	-	0.123	-	-
Yb	-	-	-	0.209	-	-
Lu	-	-	-	0.041	-	-
Hf	-	-	-	0.019	-	-

Sample Group Type	BELB 4-30 I R	BELB 5-1 I F	BELB 5-5 I F	BELB 5-8 I F	BELB 9-15 I R	BELB 9-6 I F
SiO_2	54.67	55.60	-	55.38	56.74	55.37
Al_2O_3	4.59	4.66	-	4.84	2.07	4.72
FeO	6.45	6.77	-	6.71	5.24	6.46
MnO	0.14	0.13	-	0.14	0.09	0.13
MgO	32.30	32.85	-	32.56	33.96	32.72
CaO	0.92	0.75	-	0.76	0.89	0.69
Na_2O	0.12	0.10	-	0.12	0.10	0.09
Cr_2O_3	0.49	0.34	-	0.32	0.59	0.32
TiO_2	0.09	0.10	-	0.11	0.01	0.13
NiO	0.10	0.11	-	0.11	0.10	0.09
Sum	99.87	101.42	-	101.06	99.79	100.71
Ti	-	-	-	-	-	-
Sr	-	-	-	-	-	-
Y	-	-	-	-	-	-
Zr	-	-	-	-	-	-
Nb	-	-	-	-	-	-
La	-	-	-	-	-	-
Ce	-	-	-	-	-	-
Nd	-	-	-	-	-	-
Sm	-	-	-	-	-	-
Eu	-	-	-	-	-	-
Gd	-	-	-	-	-	-
Dy	-	-	-	-	-	-
Er	-	-	-	-	-	-
Yb	-	-	-	-	-	-
Lu	-	-	-	-	-	-
Hf	-	-	-	-	-	-

Sample	BELB 9-8	CC07-1-01	CC07-1-04	CC07-1-06	CC07-1-09
Group	I	II	I	I	I
Type	F	-	-	-	-
SiO_2	55.54	52.76	56.53	55.03	56.87
Al_2O_3	4.43	6.10	1.68	3.71	2.85
FeO	6.30	9.34	5.38	7.20	5.66
MnO	0.13	0.18	0.14	0.15	0.13
MgO	33.01	28.34	34.56	32.75	33.79
CaO	0.71	1.21	0.46	0.85	0.59
Na_2O	0.09	0.06	0.06	0.07	0.02
Cr_2O_3	0.33	0.43	0.30	0.34	0.27
TiO_2	0.09	0.24	0.04	0.10	0.04
NiO	0.09	0.06	0.09	0.10	0.12
Sum	100.72		99.23	100.30	100.32
Ti	-	-	-	233	173
Sr	-	-	-	0.692	0.274
Y	-	-	-	0.545	0.937
Zr	-	-	-	1.683	0.768
Nb	-	-	-	0.033	0.008
La	-	-	-	0.022	0.005
Ce	-	-	-	0.083	0.023
Nd	-	-	-	0.068	0.031
Sm	-	-	-	0.020	0.014
Eu	-	-	-	0.009	0.006
Gd	-	-	-	0.035	0.031
Dy	-	-	-	0.066	0.102
Er	-	-	-	0.067	0.140
Yb	-	-	-	0.114	0.252
Lu	-	-	-	0.021	0.048
Hf	-	-	-	0.026	0.020

Sample	**CC07-1-14**	**CC07-1-20**	**CC07-1-22**	**CC07-1-23**	**CC07-1-24**	**CC07-1-26**
Group	**I**	**I**	**I**	**II**	**I**	**I**
Type	**-**	**-**	**-**	**-**	**-**	**-**
SiO_2	54.77	54.66	54.72	53.79	53.901	54.48
Al_2O_3	4.57	4.14	4.31	6.26	3.616	5.26
FeO	6.08	5.72	6.30	8.81	6.797	6.65
MnO	0.14	0.15	0.14	0.17	0.146	0.12
MgO	32.77	33.37	32.58	29.21	33.318	32.04
CaO	0.88	0.80	0.87	1.15	0.670	0.95
Na_2O	0.07	0.04	0.06	0.08	0.066	0.11
Cr_2O_3	0.56	0.57	0.44	0.53	0.359	0.52
TiO_2	0.05	0.02	0.08	0.22	0.053	0.21
NiO	0.11	0.11	0.08	0.08	0.097	0.13
Sum	99.70		99.58	100.30	99.02	100.47
Ti	174	162	173	-	-	-
Sr	0.818	1.291	1.285	-	-	-
Y	0.527	0.499	0.617	-	-	-
Zr	0.785	0.194	0.280	-	-	-
Nb	0.024	0.039	0.025	-	-	-
La	0.017	0.024	0.020	-	-	-
Ce	0.067	0.065	0.045	-	-	-
Nd	0.045	0.022	0.024	-	-	-
Sm	0.011	0.005	0.007	-	-	-
Eu	0.006	0.003	0.003	-	-	-
Gd	0.019	0.012	0.018	-	-	-
Dy	0.061	0.050	0.074	-	-	-
Er	0.078	0.067	0.103	-	-	-
Yb	0.140	0.127	0.184	-	-	-
Lu	0.026	0.024	0.037	-	-	-
Hf	0.014	0.005	0.004	-	-	-

Sample Group Type	CC07-1-27 II -	CC07-1-29 I -	CC07-1-33 II -	CC07-1-35 I -	CC07-1-41 I -	CC07-1-51 I -
SiO_2	-	57.32	52.38	55.12	56.28	53.82
Al_2O_3	-	2.19	6.81	4.46	2.54	4.69
FeO	-	5.18	9.16	6.15	5.98	7.99
MnO	-	0.13	0.20	0.13	0.13	0.13
MgO	-	34.64	30.01	32.92	34.45	31.12
CaO	-	0.44	0.99	0.95	0.58	0.99
Na_2O	-	0.01	0.07	0.07	0.02	0.13
Cr_2O_3	-	0.20	0.28	0.57	0.20	0.54
TiO_2	-	0.06	0.24	0.05	0.03	0.03
NiO	-	0.07	0.07	0.10	0.10	0.09
Sum	-	100.25	100.22	100.51	100.31	99.52
Ti	-	323	-	216	218	273
Sr	-	0.119	-	0.957	0.313	0.622
Y	-	0.640	-	0.587	0.842	0.656
Zr	-	0.324	-	1.255	1.029	1.059
Nb	-	0.006	-	-	0.024	-
La	-	0.005	-	0.020	0.015	0.005
Ce	-	0.012	-	0.079	0.046	0.031
Nd	-	0.016	-	0.054	0.075	0.050
Sm	-	0.009	-	0.014	0.016	0.025
Eu	-	0.004	-	0.005	0.008	0.008
Gd	-	0.028	-	0.025	0.028	0.044
Dy	-	0.078	-	0.064	0.086	0.078
Er	-	0.093	-	0.086	0.120	0.097
Yb	-	0.160	-	0.170	0.201	0.149
Lu	-	0.032	-	-	0.043	-
Hf	-	0.015	-	0.021	0.013	0.012

Sample	**CC07-2-01**	**CC07-3-01**
Group	**I**	**I**
Type	**-**	**-**
SiO_2	55.02	54.57
Al_2O_3	4.84	4.00
FeO	6.36	8.03
MnO	0.12	0.16
MgO	32.10	32.35
CaO	1.10	0.87
Na_2O	0.11	0.05
Cr_2O_3	0.68	0.31
TiO_2	0.20	0.10
NiO	0.12	0.06
Sum	100.65	100.50
Ti	1334	-
Sr	1.192	-
Y	1.155	-
Zr	3.364	-
Nb	0.091	-
La	0.032	-
Ce	0.116	-
Nd	0.143	-
Sm	0.058	-
Eu	0.024	-
Gd	0.093	-
Dy	0.169	-
Er	0.149	-
Yb	0.206	-
Lu	0.034	-
Hf	0.094	-

Appendix 4: Olivine and spinel major element compositions of RGR xenoliths

Sample	**07EB1.01**	**07EB1.05**	**07EB1.06**	**07EB1.09**	**07EB1.10**	**07EB1.11**
Group	**I**	**I**	**I**	**I**	**I**	**I**
Type	**F**	**F**	**R**	**F**	**F**	**R**
Olivine						
SiO_2	40.54	40.43	40.55	40.18	40.16	40.40
Al_2O_3	0.04	0.02	0.03	0.02	0.02	0.03
FeO	9.84	10.49	8.92	10.40	10.22	8.81
MnO	0.16	0.15	0.13	0.15	0.14	0.13
MgO	48.97	48.62	50.83	48.42	48.59	49.73
CaO	0.10	0.07	0.09	0.07	0.07	0.09
Na_2O	0.01	0.01	0.01	0.02	0.01	0.01
Cr_2O_3	0.02	0.02	0.04	0.01	0.04	0.03
TiO_2	0.01	0.01	0.03	0.01	0.01	0.01
NiO	0.37	0.34	0.40	0.38	0.40	0.39
Sum	100.05	100.17	101.01	99.65	99.65	99.63
Mg#	0.899	0.892	0.910	0.893	0.894	0.910
Spinel						
SiO_2	0.10	0.07	0.04	0.03	0.03	0.05
Al_2O_3	56.44	58.47	36.73	58.84	57.05	37.36
FeO	10.96	10.89	13.71	10.93	11.32	12.99
MnO	0.10	0.08	0.08	0.07	0.10	0.09
MgO	21.81	21.77	17.79	21.30	20.79	18.77
CaO	0.02	0.01	0.01	0.01	0.01	0.01
Na_2O	-	-	-	-	-	-
Cr_2O_3	10.23	8.76	31.62	8.19	9.15	31.41
TiO_2	0.11	0.12	0.07	0.11	0.08	0.08
NiO	0.39	0.40	0.24	0.40	0.40	0.24
Sum	100.15	100.56	100.28	99.88	98.93	101.00
Cr#	0.108	0.091	0.366	0.085	0.097	0.361

Sample	**07EB1.16**	**07EB2.03**	**07EB4.01**	**07EB4.05**	**07EB4.06**	**07EB4.07**
Group	**I**	**I**	**I**	**I**	**I**	**I**
Type	**F**	**F**	**F**	**F**	**F**	**F**
Olivine						
SiO_2	39.81	40.23	40.12	40.47	-	-
Al_2O_3	0.03	0.02	0.03	0.03	-	-
FeO	13.30	10.54	10.75	10.98	-	-
MnO	0.20	0.15	0.15	0.16	-	-
MgO	46.55	48.65	48.28	48.46	-	-
CaO	0.10	0.07	0.07	0.07	-	-
Na_2O	0.01	0.01	0.01	0.01	-	-
Cr_2O_3	0.02	0.03	0.01	0.03	-	-
TiO_2	0.01	0.01	0.00	0.03	-	-
NiO	0.33	0.34	0.36	0.40	-	-
Sum	100.36	100.05	99.79	100.64	-	-
Mg#	0.862	0.892	0.889	0.887	-	-
Spinel						
SiO_2	0.04	0.05	0.08	0.07	0.03	0.02
Al_2O_3	44.36	56.98	59.03	56.90	57.21	57.71
FeO	17.35	10.92	10.85	12.35	12.63	10.17
MnO	0.07	0.08	0.09	0.10	0.11	0.08
MgO	17.62	21.02	20.70	20.36	20.29	21.05
CaO	0.01	0.02	0.01	0.00	0.01	0.00
Na_2O	-	-	-	-	-	-
Cr_2O_3	18.97	10.03	7.90	8.74	9.44	9.37
TiO_2	0.24	0.06	0.09	0.06	0.04	0.06
NiO	0.28	0.38	0.40	0.38	0.38	0.37
Sum	98.94	99.54	99.16	98.95	100.14	98.83
Cr#	0.223	0.106	0.082	0.093	0.100	0.098

Sample	07EB4.13	07EB4.18	07EB4.19	07EB4.21	07EB4.22	BELB 4-1
Group	I	I	I	I	I	I
Type	F	R	R	F	F	F
Olivine						
SiO_2	-	40.67	-	40.10	-	-
Al_2O_3	-	0.02	-	0.01	-	-
FeO	-	9.35	-	10.08	-	-
MnO	-	0.13	-	0.15	-	-
MgO	-	49.59	-	48.57	-	-
CaO	-	0.07	-	0.06	-	-
Na_2O	-	0.01	-	0.00	-	-
Cr_2O_3	-	0.02	-	0.03	-	-
TiO_2	-	0.01	-	0.00	-	-
NiO	-	0.36	-	0.39	-	-
Sum	-	100.24	-	99.39	-	-
Mg#	-	0.904	-	0.896	-	-
Spinel						
SiO_2	0.03	0.07	0.04	0.06	0.03	0.05
Al_2O_3	57.60	39.38	29.03	57.01	56.38	57.67
FeO	10.79	12.15	15.04	10.72	10.29	11.17
MnO	0.07	0.09	0.07	0.07	0.08	0.00
MgO	21.06	18.65	17.13	20.88	21.39	20.85
CaO	0.01	0.01	0.00	0.01	0.01	0.00
Na_2O	-	-	-	-	-	-
Cr_2O_3	9.13	28.82	39.74	10.60	11.16	10.84
TiO_2	0.11	0.01	0.17	0.06	0.07	0.10
NiO	0.39	0.24	0.20	0.38	0.37	0.36
Sum	99.19	99.42	101.42	99.79	99.78	101.05
Cr#	0.096	0.329	0.479	0.111	0.117	0.112

Sample	BELB 4-30	BELB 5-1	BELB 5-5	BELB 5-8	BELB 9-15	BELB 9-6
Group	I	I	I	I	I	I
Type	R	F	F	F	R	F
Olivine						
SiO_2	40.69	40.38	-	40.44	41.25	40.95
Al_2O_3	0.02	0.02	-	0.02	0.02	0.02
FeO	10.27	10.85	-	10.77	8.50	10.30
MnO	0.16	0.16	-	0.14	0.12	0.15
MgO	49.09	48.92	-	49.11	50.69	48.98
CaO	0.08	0.08	-	0.08	0.07	0.07
Na_2O	0.01	0.01	-	0.01	0.00	0.01
Cr_2O_3	0.02	0.02	-	0.02	0.01	0.01
TiO_2	0.01	0.01	-	0.01	0.02	0.01
NiO	0.35	0.38	-	0.38	0.41	0.37
Sum	100.70	100.83	-	100.98	101.10	100.87
Mg#	0.895	0.889	-	0.890	0.914	0.895
Spinel						
SiO_2	0.09	0.05	0.04	0.04	0.08	0.04
Al_2O_3	53.65	58.41	58.81	59.88	27.78	58.17
FeO	11.59	10.79	10.95	10.86	13.67	10.51
MnO	0.08	0.00	0.00	0.00	0.08	0.00
MgO	19.98	20.99	21.04	20.99	16.29	20.77
CaO	0.01	0.00	0.01	0.00	0.01	0.00
Na_2O	-	-	-	-	-	-
Cr_2O_3	13.15	10.03	9.28	8.23	41.36	10.61
TiO_2	0.09	0.09	0.11	0.08	0.03	0.07
NiO	0.35	0.35	0.35	0.39	0.17	0.39
Sum	98.99	100.70	100.59	100.47	99.28	100.55
Cr#	0.141	0.103	0.096	0.084	0.500	0.109

Sample	BELB 9-8	CC07-1-01	CC07-1-04	CC07-1-06	CC07-1-09
Group	I	II	I	I	I
Type	F	-	-	-	-
Olivine					
SiO_2	40.47	39.87	40.86	40.10	41.39
Al_2O_3	0.02	0.02	0.01	0.01	0.01
FeO	10.13	14.44	8.18	11.52	8.79
MnO	0.14	0.19	0.14	0.19	0.11
MgO	49.48	43.83	50.46	48.81	49.59
CaO	0.07	0.06	0.05	0.05	0.04
Na_2O	0.01	0.01	0.01	0.04	0.01
Cr_2O_3	0.01	0.02	0.03	0.02	0.03
TiO_2	0.01	0.01	0.03	0.01	0.03
NiO	0.39	0.21	0.38	0.37	0.37
Sum	100.73	98.66	100.13	101.12	
Mg#	0.897	0.844	0.917	0.883	0.910
Spinel					
SiO_2	0.03	-	0.02	0.02	0.02
Al_2O_3	58.16	-	29.70	51.13	49.91
FeO	10.31	-	16.14	12.18	15.51
MnO	0.00	-	0.11	0.05	0.11
MgO	20.94	-	15.94	19.08	18.54
CaO	0.01	-	0.01	0.01	0.00
Na_2O	-	-	-	-	-
Cr_2O_3	10.76	-	37.70	16.62	16.05
TiO_2	0.07	-	0.09	0.04	0.31
NiO	0.38	-	0.18	0.34	0.35
Sum	100.67	-	99.88	99.46	100.80
Cr#	0.110	-	0.460	0.179	0.178

Sample	**CC07-1-14**	**CC07-1-20**	**CC07-1-22**	**CC07-1-23**	**CC07-1-24**	**CC07-1-26**
Group	**I**	**I**	**I**	**II**	**I**	**I**
Type	-	-	-	-	-	-
Olivine						
SiO_2	40.79	40.36	40.22	40.76	40.36	40.36
Al_2O_3	0.02	0.01	0.08	0.02	0.01	0.04
FeO	9.39	9.00	9.86	13.65	11.06	10.57
MnO	0.13	0.13	0.14	0.19	0.16	0.15
MgO	49.66	49.94	49.21	45.35	49.48	48.77
CaO	0.05	0.07	0.05	0.08	0.04	0.09
Na_2O	0.01	0.01	0.01	0.01	0.00	0.03
Cr_2O_3	0.02	0.01	0.03	0.01	0.01	0.02
TiO_2	0.01	0.03	0.02	0.01	0.01	0.02
NiO	0.39	0.40	0.40	0.26	0.39	0.32
Sum	100.47	99.98	100.02	100.33	101.51	100.36
Mg#	0.904	0.908	0.899	0.856	0.889	0.892
Spinel						
SiO_2	0.03	0.04	0.03	0.04	0.02	-
Al_2O_3	47.51	46.92	48.75	44.29	49.95	-
FeO	12.29	12.39	12.54	19.21	13.03	-
MnO	0.09	0.08	0.08	0.14	0.09	-
MgO	19.35	19.32	19.34	15.88	18.20	-
CaO	0.02	0.01	0.00	0.01	0.01	-
Na_2O	-	-	-	-	-	-
Cr_2O_3	19.05	19.67	17.66	20.31	17.60	-
TiO_2	0.05	0.05	0.09	0.46	0.11	-
NiO	0.30	0.32	0.35	0.25	0.31	-
Sum	98.67	98.80	98.84	100.58	99.32	-
Cr#	0.212	0.220	0.196	0.235	0.191	-

Sample	**CC07-1-27**	**CC07-1-29**	**CC07-1-33**	**CC07-1-35**	**CC07-1-41**	**CC07-1-51**
Group	**II**	**I**	**II**	**I**	**I**	**I**
Type	**-**	**-**	**-**	**-**	**-**	**-**
Olivine						
SiO_2	-	41.66	40.07	41.01	41.40	39.98
Al_2O_3	-	0.01	0.02	0.02	0.01	0.02
FeO	-	7.91	14.48	9.64	9.21	13.15
MnO	-	0.13	0.20	0.14	0.14	0.17
MgO	-	50.39	46.51	49.85	49.20	46.40
CaO	-	0.03	0.07	0.08	0.04	0.11
Na_2O	-	0.04	0.01	0.03	0.02	0.03
Cr_2O_3	-	0.03	0.02	0.02	0.04	0.03
TiO_2	-	0.00	0.02	0.00	0.00	0.01
NiO	-	0.35	0.25	0.40	0.42	0.35
Sum	-	100.54	101.65	101.18	100.47	100.26
Mg#	-	0.919	0.851	0.902	0.905	0.863
Spinel						
SiO_2	-	0.02	0.05	0.05	0.02	0.07
Al_2O_3	-	39.90	59.62	48.47	50.88	47.57
FeO	-	13.66	15.27	12.51	13.68	16.93
MnO	-	0.08	0.13	0.10	0.07	0.13
MgO	-	18.06	19.77	19.91	19.80	18.32
CaO	-	0.00	0.01	0.00	0.01	0.02
Na_2O	-	-	-	-	-	-
Cr_2O_3	-	27.55	5.44	19.04	14.35	17.66
TiO_2	-	0.13	0.24	0.05	0.05	0.19
NiO	-	0.22	0.30	0.33	0.39	0.31
Sum	-	99.61	100.83	100.47	99.25	101.20
Cr#	-	0.317	0.058	0.209	0.159	0.199

Sample	CC07-2-01	CC07-3-01
Group	I	I
Type	-	-
Olivine		
SiO_2	41.04	39.97
Al_2O_3	0.04	0.02
FeO	9.99	12.52
MnO	0.15	0.18
MgO	48.85	48.31
CaO	0.10	0.06
Na_2O	0.02	0.01
Cr_2O_3	0.02	0.01
TiO_2	0.02	0.01
NiO	0.39	0.30
Sum	100.61	101.39
Mg#	0.897	0.873
Spinel		
SiO_2	0.09	0.07
Al_2O_3	47.16	46.62
FeO	13.96	13.96
MnO	0.07	0.10
MgO	19.83	19.36
CaO	0.00	0.01
Na_2O	-	-
Cr_2O_3	18.48	19.54
TiO_2	0.54	0.36
NiO	0.35	0.35
Sum	100.49	100.39
Cr#	0.208	0.219

Appendix 5: Supplement to Chapter 1

A5.1 ANALYTICAL METHODS

Large (>5cm diameter) xenoliths were split in half and a portion was used for bulk analysis. A diamond saw was used to remove any basaltic rind from the xenoliths. Samples were powdered in an alumina ceramic ball mill. Major and trace elements for bulk xenoliths were collected by XRF and ICP-MS at the Washington State University GeoAnalytical Laboratory. Duplicates were run for two samples which were reproducible to within 5% for the Sr, Sc, Ta, Nb, Y and the L-MREE, 10% for the HREE and 15% for the remaining trace elements except Cs, Th, and Pb. Procedures are outlined in (Johnson et al., 1999), (Knaack et al., 1994), and (Jenner et al., 1990). Major element compositions for clinopyroxene, orthopyroxene, olivine, and spinel were measured on thin-sections and epoxy grain mounts at the University of Texas at Austin using a JEOL JXA-8200 EMPA. In most cases 5-10 analyses per mineral per sample were performed. Specific numbers of analyses are available in appendix A.2 and A.3. Analyses were performed at 15kV accelerating voltage, with a 10nA beam current, using a focused beam. Reported major element concentrations are commonly reproducible within 5% (2 s.d.). Clinopyroxene in F-type xenoliths 07EB4.05, 07EB4.07, 07EB4.21, BELB5-1, BELB5-8, BELB9-6 and BELB9-8 from Elephant Butte showed minor core-rim variation and had slightly depleted rims. The concentration of Al_2O_3 in the rims of these samples is ~0.3-0.4 wt. % lower than in the cores (a difference in Cr# of ~0.5). Samples from Cerro Chato did not display significant core-rim variation. Trace elements in clinopyroxene were measured by LA-ICP-MS at UT-Austin using an Agilent 7500ce quadrupole with a New Wave UP-193FX laser system. Initially 100μm spots were used, but were changed to 75μm to achieve better spatial resolution. Spots were pre-ablated and dwell times ranged from 40-60s with 60-120s washout times. NIST-612 was used as a primary standard and BCR-2g as a secondary standard. Analyses of all elements for BCR-2g were accurate to within <10% of the accepted values and Ti, La, Ce, Nd, Sm, and Yb were accurate to within <5% (Appendix A.2). However, our measured values were systematically lower than the preferred values for BCR-2G. Because the difference is minor relative to the observed variations, no additional correction was applied to the data. Repeated analyses of BCR-2g were reproducible to within ~5% (1σ). Strontium, Nd and Pb isotopes were measured on cpx separates. Clinopyroxene separates from a subset of xenoliths were digested in an HF:HNO_3 solution and Sr, Nd and Pb were extracted and purified following procedures similar to (Lassiter et al., 2003) and (Carlson and Irving, 1994). Sr-Spec, REE-spec/HDEHP, and AG1-X8 resins were used to separate Sr, Nd, and Pb, respectively. Rhenium and osmium were separated from bulk xenoliths following the procedure of (Lassiter et al., 2003) except that Os was extracted from inverse aqua regia using CCl_4 instead of Br_2. Osmium was then purified further by microdistillation (Birck et al., 1997). Strontium and Pb were run as metals on single Re filaments and Nd as a metal on double Re filaments using the Triton TIMS at the University of Texas at Austin. Osmium was run on Pt filaments as OsO_3^- using N-TIMS. Rhenium was measured on the Micromass IsoProbe Multicollector ICP-MS at the University of Texas at Austin. Rhenium and osmium concentrations were determined using a mixed ^{190}Os-^{185}Re spike.

The average NBS 987 $^{87}Sr/^{86}Sr$ for the TIMS lab for the 12 months during which analyses were performed was 0.710253 ± 0.000011 (2 s.d.) Pb-isotopes for most samples were corrected for mass fractionation via double-spike method (Todt et al., 1993).

Double-spike corrected values for NBS 981 Pb standard during the period of analyses were $^{206}Pb/^{204}Pb$ of 19.392 ± 0.003 (2 s.d), $^{207}Pb/^{204}Pb$ of 15.487 ± 0.004 (2 s.d.), and $^{208}Pb/^{204}Pb$ of 36.685 ± 0.013 (2 s.d.). Samples with too low Pb concentrations to be analyzed via double-spike were run using an ion counter with a peak-hopping routine. A standard-sample fractionation correction was applied to these samples. Samples were corrected for 1.3‰ per AMU mass fractionation based on measured values for NBS981. The AMES-1 standard was run frequently in between samples and produced an average $^{143}Nd/^{144}Nd$ of 0.512073 ± 0.000010 (2 s.d.). Blanks were <240pg for Sr, <17pg for Pb, and <120 pg for Nd. The cpx separates, on average, contained 10,000-20,000 ng of Sr, 20-100 ng of Pb, and 500-1000 ng of Nd. The absolute amounts of Sr, Pb, and Nd were such that the impact from blanks was negligible. Rhenium blanks were <5pg/g. Osmium blanks were <4pg/g.

A5.2 PETROLOGY

Mantle xenoliths from Elephant Butte are spinel peridotites consisting of olivine, orthopyroxene, clinopyroxene, and spinel in varying proportions. The xenoliths are classified according to texture and composition after [(Frey and Prinz, 1978); (Mercier and Nicolas, 1975); (Harte, 1977)]. Sample textures can be found in Appendix A.4. Following (Frey and Prinz, 1978), ultramafic xenoliths are divided into two groups based on composition. Group-I xenoliths are primarily olivine-rich peridotites containing Cr-rich clinopyroxene and spinel. Group-II xenoliths consist mostly of clinopyroxene-rich pyroxenites whose cpx have higher Al and Ti contents than those in Group-I xenoliths and commonly have low olivine Mg-number (<85). The global origin of group-II xenoliths is the subject of debate. The presence of poikilitic textures in some group-II xenoliths is suggestive of a cumulate nature (Frey and Prinz, 1978). However, it is common to find cross-cutting vein networks of composite group-I and group-II xenoliths which is more indicative of wall rock interaction with ascending magmas (Wilshire and Shervais, 1975).

All of the xenoliths from Elephant Butte belong to group-I. Protogranular and equigranular textural types are present at Elephant Butte. Kil and Wendlandt (2004) find xenoliths with equigranular textures to have derived from lower temperatures than xenoliths with protogranular textures. We do not observe this trend in our xenoliths. These xenoliths have asthenospheric mantle trace element signatures. A range of grain sizes (olivine from 0.5mm to 8mm) is present with the coarsest grain size corresponding to the lowest modal abundance of clinopyroxene. Elephant Butte xenoliths range from 3-19% cpx. Coarse-grained (orthopyroxene and olivine ~4-7mm) xenoliths typically have low cpx abundance, averaging <5%. The majority of Elephant Butte xenoliths are more fertile than the coarse-grained samples, with cpx abundance ranging from 12-19%.

Xenoliths from Cerro Chato are more diverse, although all are spinel peridotites. Both group-I and group-II xenoliths are present. Composite (group-I and II) xenoliths are also found at Cerro Chato. Most group-I xenoliths are lherzolites (7-14% cpx) although some harzburgites and dunites are present. The group-II xenoliths at Cerro Chato are primarily wehrlites and cpx-rich (>35%) lherzolites with varying modal mineral proportions. Exsolution lamellae are common in group-II clinopyroxenes, but absent in cpx in group-I xenoliths. In one group-II wehrlite, amphibole is present. Amphibole is not present in any of the other xenoliths. Microscopic Fe-sulfides are present in some of the group-I and group-II xenoliths from Cerro Chato. Sulfides were not observed in samples from Elephant Butte.

Appendix 6: Supplement to Chapter 2

A6.1 LU-HF ANALYTICAL METHODS

Large (>5 cm diameter) samples were disaggregated and 50-150mg of inclusion-free cpx was separated for Lu-Hf analysis. Prior to digestion samples were repeatedly sonicated in 18.2 MΩ water. Samples were digested and Lu and Hf were separated following the methods of (Connelly et al., 2006). Lu and Hf analyses were performed on a Micromass Isoprobe at the University of Texas at Austin. During Hf analyses ^{173}Yb and ^{175}Lu were measured to account for interferences on ^{176}Hf. Fractionation was determined according to the ^{179}Hf/^{177}Hf ratio, which was adjusted for the effect from the addition of spike. Hf isotope dilution and isotope composition analyses were performed simultaneously using a ^{180}Hf spike. The average ^{176}Hf/^{177}Hf of JMC475 during the 6-month study was = 0.282181 ± 0.000025 (1σ, n = 25). A solution of BHVO-2 was run as a secondary standard throughout the study and had an average ^{176}Hf/^{177}Hf of 0.283091 ± 0.000014 (1σ, n = 13). Samples are reported relative to the accepted JMC475 value of ^{176}Hf/^{177}Hf = 0.282160. Lu concentrations were determined using a spike enriched in ^{176}Lu. ^{173}Yb and ^{180}Hf were monitored to account for interferences on ^{176}Lu. A fractionation factor was determined based on ^{171}Yb/^{173}Yb and a correction factor was applied to account for the difference in fractionation between Yb and Lu. Cpx Nd analyses and spinel major element analyses were performed following the methods of (Byerly and Lassiter, 2012). Neodymium was run as a metal on double Re filaments using the Triton TIMS at the University of Texas at Austin. The AMES-1 standard was run frequently in between samples and produced an average ^{143}Nd/^{144}Nd of 0.512070 ±

0.000010 (2 s.d.). Methods for Sr and Pb analyses can be found in (Byerly and Lassiter, 2012). Blanks were <30pg for Nd, <40pg for Hf, and <5pg for Lu.

A6.2 MODELING PERIDOTITE MELTING WITH PMELTS

In order to model the adiabatic ascent and melting of mantle with different bulk compositions we utilized pMELTS software (Ghiorso et al., 2002). We used the average bulk-composition of the Elephant Butte xenoliths to estimate the melt productivity of fertile mantle with ultra-depleted isotopic compositions. In order to simulate the major element composition of ultra-depleted domains from the Gakkel ridge and Hawai'i we subtracted varying amounts of MORB (Workman and Hart, 2005) from a primitive mantle composition (McDonough and Sun, 1995) until we reached the average bulk-Al_2O_3 composition of the respective localities. These compositions are shown in Table A2.2.1. Those bulk compositions were entered into the pMELTS software to model adiabatic ascent and melting. The bulk compositions were initially equilibrated at 1375°C and 25kb at the FMQ buffer. The initial temperature of 1375°C was chosen to correspond to a potential temperature of ~1350°C (Lee et al., 2009). The samples were then brought up isentropically to 2kb without constraint on fO_2 while fractionating any liquid that was produced. The results of these models are shown below.

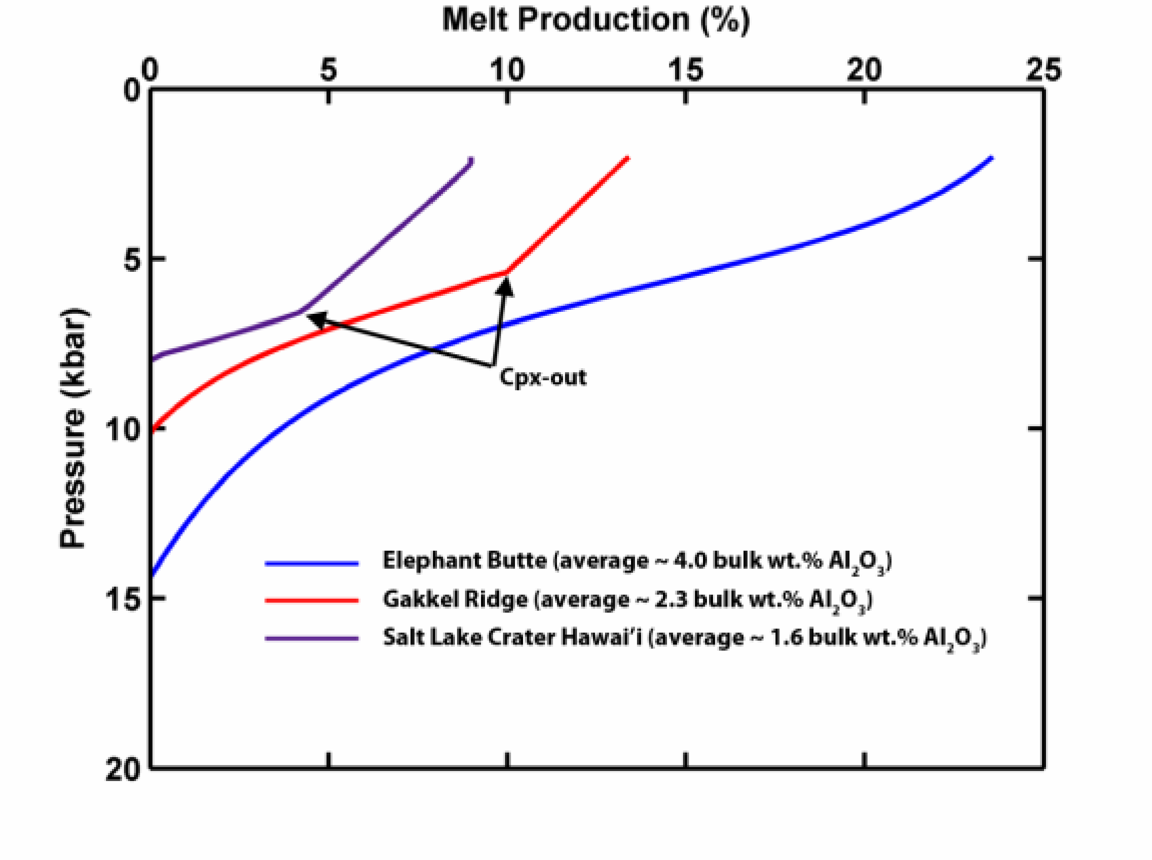

Figure A6.2.1 Results of pMELTS models for the adiabatic ascent and melting of ultra-depleted mantle with different starting bulk compositions.

The amount of melt produced is strongly controlled by the starting composition. Despite their moderately refractory to refractory compositions, samples from Hawai'i and the Gakkel ridge are capable of producing melt

The results of these models suggest that very fertile (> 3.5wt. % Al_2O_3) ultra-depleted domains, such as those from Elephant Butte, may be under-sampled by abyssal peridotites due to some degree of recent melt extraction. Abyssal peridotites sample the top of the adiabatic melting column beneath a mid-ocean ridge (~2.2kb) and could have experienced up to 15-20% melt extraction subsequent to their emplacement on the seafloor, whereas samples derived from ~40km depth would have experienced very little (<5%) melt extraction in the same melting column.

Table A6.2.1 Inputs and results of pMELTS model

Starting Compositon

	Elephant Butte	Gakkel Ridge[a]	Salt Lake Crater Hawai'i[b]
SiO_2	44.69	44.24	43.94
Al_2O_3	4.03	2.28	1.56
FeO^T	8.43	8.05	8.05
MnO	0.15	0.13	0.13
MgO	38.52	42.79	44.39
CaO	3.45	1.97	1.44
Na_2O	0.24	0.04	0.00
Cr_2O_3	0.37	0.44	0.45
TiO_2	0.13	0.08	0.04

[a] Bulk composition was estimated by removing MORB from PM to reach ~2.3 wt.% Al_2O_3 (average of Gakkel Ridge peridotites)

[b] Bulk composition was estimated by removing MORB from PM to reach ~1.6 wt.% Al_2O_3 (average of SLC Hawai'i xenoliths)

Accumulated Melts

	Elephant Butte	Gakkel Ridge	Salt Lake Crater Hawai'i
SiO_2	49.78	50.58	53.19
Al_2O_3	16.05	14.79	14.48
FeO^T	8.53	8.45	6.77
MnO	0.01	0.01	0.01
MgO	12.00	13.23	13.11
CaO	11.77	11.74	11.83
Na_2O	1.03	0.30	0.00
Cr_2O_3	0.03	0.04	0.09
TiO_2	0.54	0.57	0.41

Residue

	Elephant Butte	Gakkel Ridge	Salt Lake Crater Hawai'i
SiO_2	43.08	43.23	43.03
Al_2O_3	0.34	0.36	0.29
FeO^T	8.39	7.98	8.17
MnO	0.19	0.15	0.14
MgO	46.60	47.29	47.45
CaO	0.90	0.47	0.42
Na_2O	0.00	0.00	0.00
Cr_2O_3	0.47	0.50	0.49
TiO_2	0.00	0.00	0.00

A6.3 MIXING OF ECLOGITE COMPONENT

We chose our eclogite component to be derived from MORB that was subducted into the mantle 2.0 Ga. We assumed the MORB at 2 Ga to have the same isotopic composition as DMM at 2 Ga (using Lu/Hf, Sm/Nd, ^{143}Nd/^{144}Nd, and ^{176}Hf/^{177}Hf of DMM from Workman and Hart, 2005). We also assumed MORB generated at 2 Ga to have the same composition as average MORB today. During subduction neither the isotopic compositions nor parent/daughter ratios are disturbed. This subducted MORB component then remains chemically isolated from the rest of the mantle for 2 Ga while undergoing radiogenic in-growth to yield its present-day composition. The weighted mean Hf and Nd isotopic compositions of the Elephant Butte xenoliths were used along with average Hf and Nd concentrations from the Elephant Butte xenoliths. The average Elephant Butte mantle component was mixed with the 2 Ga MORB component to generate the mixing curve in Figure 2B.

Inputs to mixing model

	Nd (ppm)	**^{143}Nd/^{144}Nd**	**ε_{Nd}**	**Hf (ppm)**	**^{176}Hf/^{177}Hf**	**ε_{Hf}**
Elephant Butte	0.53	0.513358	14.0	0.15	0.283474	24.8
MORB-derived eclogite	9.3	0.512327	-6.1	2.31	0.282211	-19.8

A6.4 PREFERENTIAL SAMPLING OF FERTILE MANTLE COMPONENTS

The pMELTS models describe above demonstrate that a range of source compositions are capable of melting when advected along a modern mantle adiabat. In a heterogeneous mantle, melts brought to the surface represent a sum of melts generate by melting sources with a range of fertilities and incompatible trace element compositions. Because the fertile components melt more, melt over a larger depth range, and have higher incompatible trace element concentrations, the melts generated from a heterogeneous mantle will be biased towards these fertile compositions. To demonstrate this effect we have performed a Monte Carlo simulation to model the compositions of melts that would be generated from a heterogeneous mantle. We took primitive mantle (McDonough and Sun, 1995) and extracted variable amounts of melt at 2 Ga. This ancient melting results in a wide range of major element compositions and isotopic compositions in the mantle (Figure S2). This mantle is brought up adiabatically and melts following the pMELTS models described above. The amount of melting, and depth at which melting initiates is a function of the fertility of the source (e.g. Figure S1). For simplicity we summed the melts generated from five discrete intervals in a triangular melting region. In the scenario shown in Figure S2, an average of 9 ± 0.3 (1□) % melt was extracted from primitive mantle to generate the source mantle. This results in an average bulk composition of ~3.2 ± 0.5 (1□) wt. % Al_2O_3 which ranges from ~4.4 to ~1.3 wt. Al_2O_3. The 2Ga time integrated effect of this melt depletion results in a mantle with a weighted mean ε_{Hf} of ~44. However, the melts generated from melting this mantle in a triangular melt region have ε_{Hf} of ~29 (Figure S2). This is due to the large proportion of melt generated by more fertile (and less depleted) components. The melts appear the represent a mantle that is considerable less-depleted than the actual source composition.

Salters and Stracke (2004) estimate the major element composition of DMM by subtracting a small amount (1.5% total from two different pressures) of melt from PM. Their constraints on the amount of melt extracted are the isotopic compositions and parent/daughter ratios of their estimate for DMM. This method underestimates the average amount of melt extraction from PM due to MORB melts having less depleted compositions than the actual average mantle source if the mantle is compositionally heterogeneous on the scale sampled at mid-ocean ridges.

Workman and Hart (2005) estimate major the element of DMM by determining the modal abundances of mantle minerals that correspond to their estimate for the trace element composition of MORB (via correlations between modal abundances and incompatible trace elements in abyssal peridotites). They too encounter the same problem that MORB preferentially sample the most fertile (and least depleted) mantle. Therefore, since their estimate for DMM is not as depleted in incompatible trace elements as "average" peridotitic convecting upper mantle they overestimate the fertility of DMM.

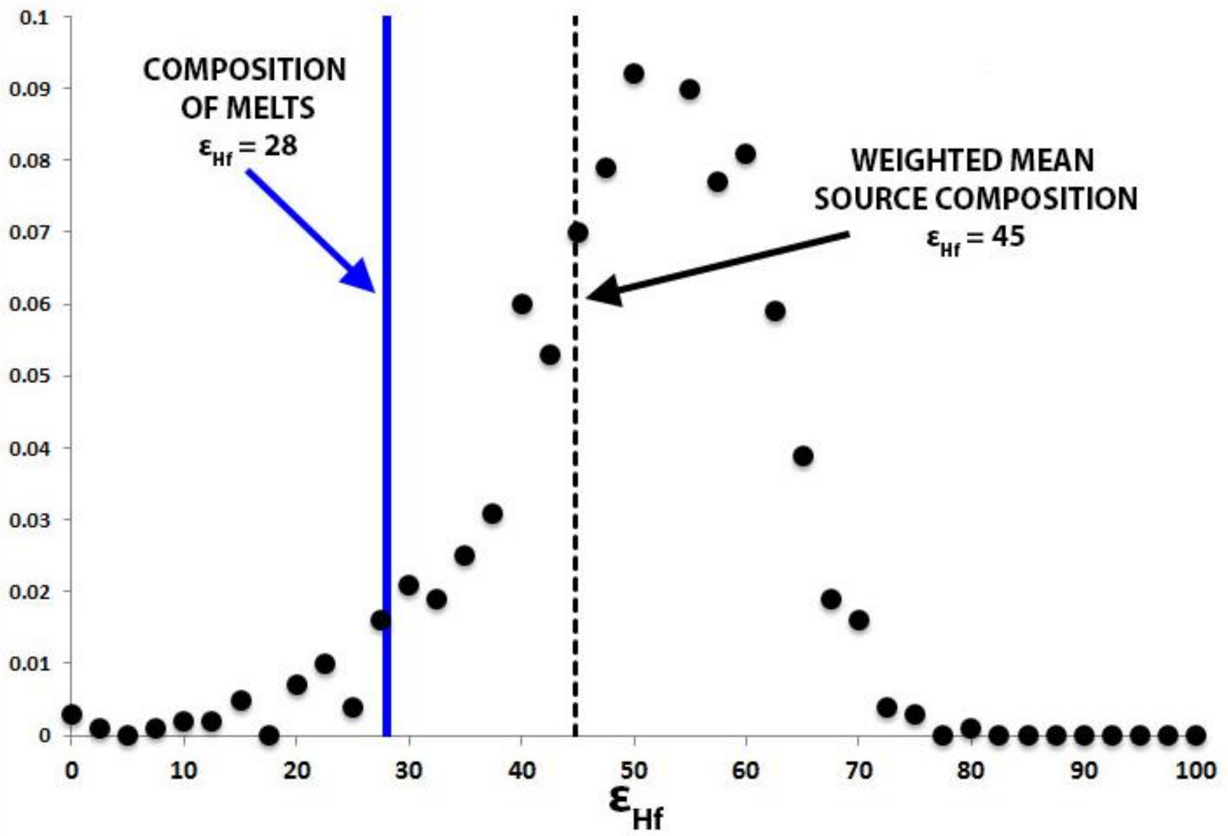

Figure A6.4.1 Monte Carlo simulation demonstrating the distribution of mantle hafnium isotopic compositions resulting from variable (9 ± 3 (1□) %) melt extraction from primitive mantle at 2 Ga (black circles).

The weighted mean hafnium composition of the mantle source at present day is shown as a dashed black line. The melts extracted from this mantle source have a less-depleted isotopic composition (solid blue line).

Appendix 7: Supplement to Chapter 3

DETAILED ANALYTICAL METHODS

A ~30ppb solution of JMC475 was measured several (5-10) times per day during the course of the study. The within-day reproducibility of the JMC standard was typically approximately one epsilon. Samples are reported relative to the accepted JMC475 value of $^{176}Hf/^{177}Hf = 0.282160$. A solution of BHVO-2 was run as a secondary standard throughout the study and had an average $^{176}Hf/^{177}Hf$ of 0.283096 ± 0.000020 (2 s.d.) The AMES-1 neodymium standard was run frequently in between samples and produced an average $^{143}Nd/^{144}Nd$ of 0.512070 ± 0.000010 (2 s.d.). Blanks were <30pg for Nd, <40pg for Hf, and <5pg for Lu. Spot sizes of 150μm were used for LA-ICP-MS analyses of cpx and opx. NIST-612 was used as a primary standard and BCR-2g as a secondary standard. Analyses of all elements for BCR-2g were accurate to within <10% of the accepted values and Ti, La, Ce, Nd, Sm, and Yb were accurate to within <5% Repeated analyses of BCR-2g were reproducible to within ~10% (1σ). Multiple (5-10) grains were analyzed of each mineral phase with average reproducibilities of < 9% for the REE+Hf for cpx and < 26% for the REE+Hf for opx.

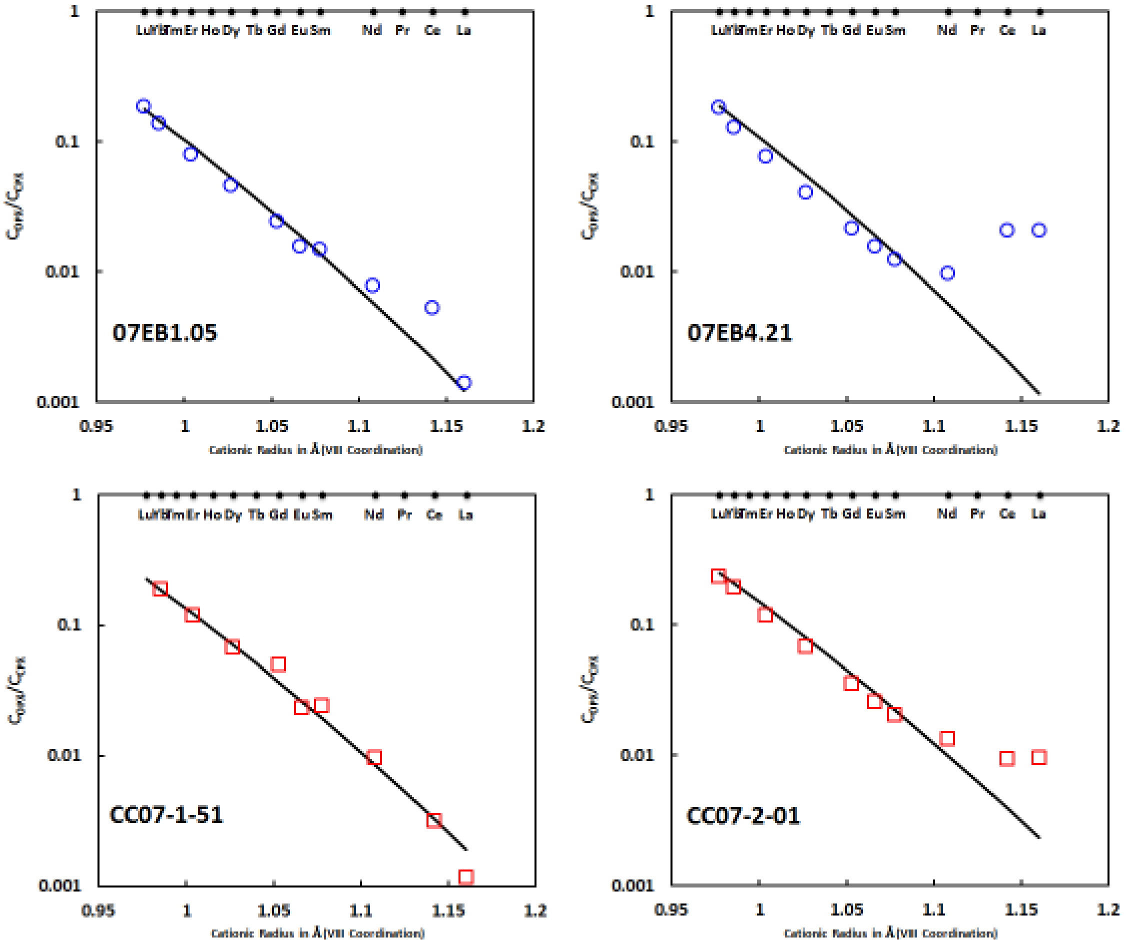

Figure A7.1 Plot of C_{OPX}/C_{CPX} ($D^{OPX/CPX}$) versus REE cationic radius (VIII coordination)

Samples 07EB1.05 and CC07-1-51 show good correlation between C_{OPX}/C_{CPX} and cationic radius for all REE indicating cpx and opx are in equilibrium. Samples 07EB4.21 and CC07-2-01 have LREE that fall off of the correlation indicating these elements are not equilibrated between cpx and opx.

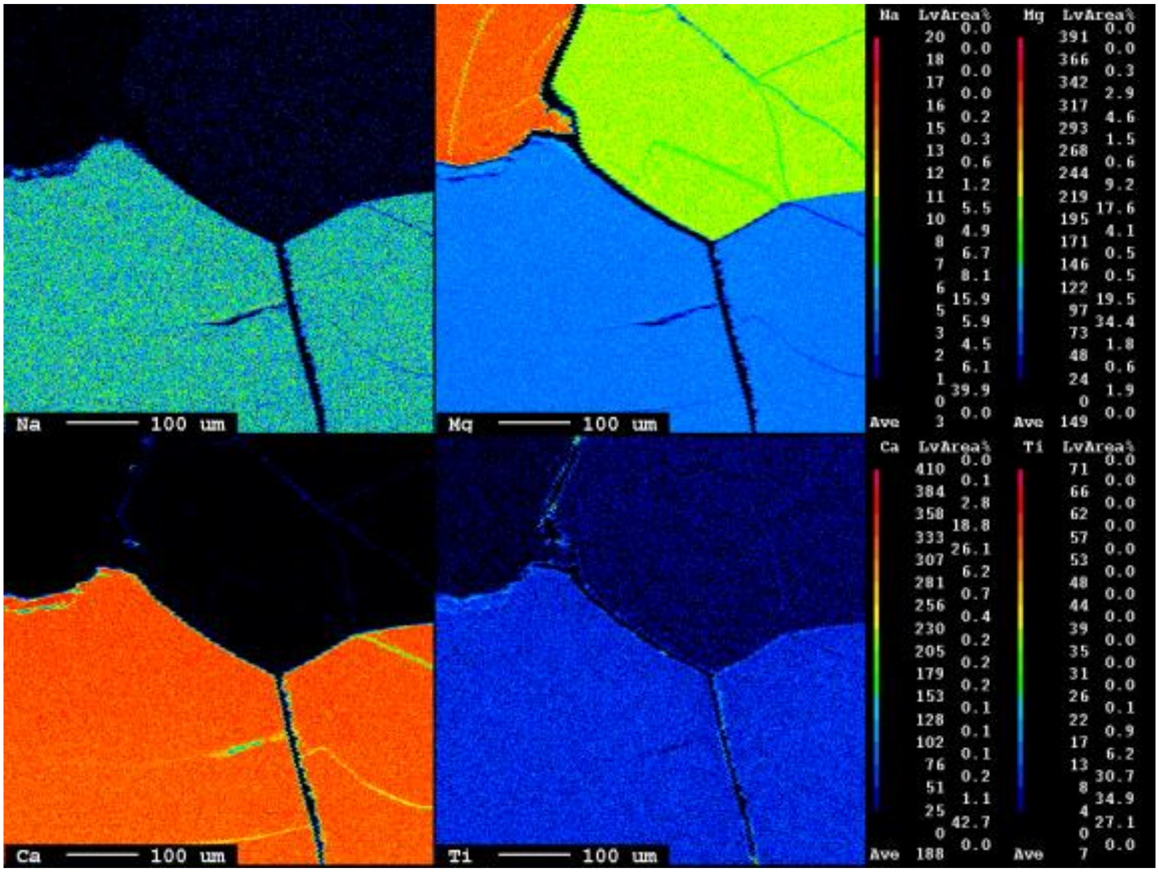

Figure A7.2a X-ray map showing example of grain boundaries in sample 07EB4.05

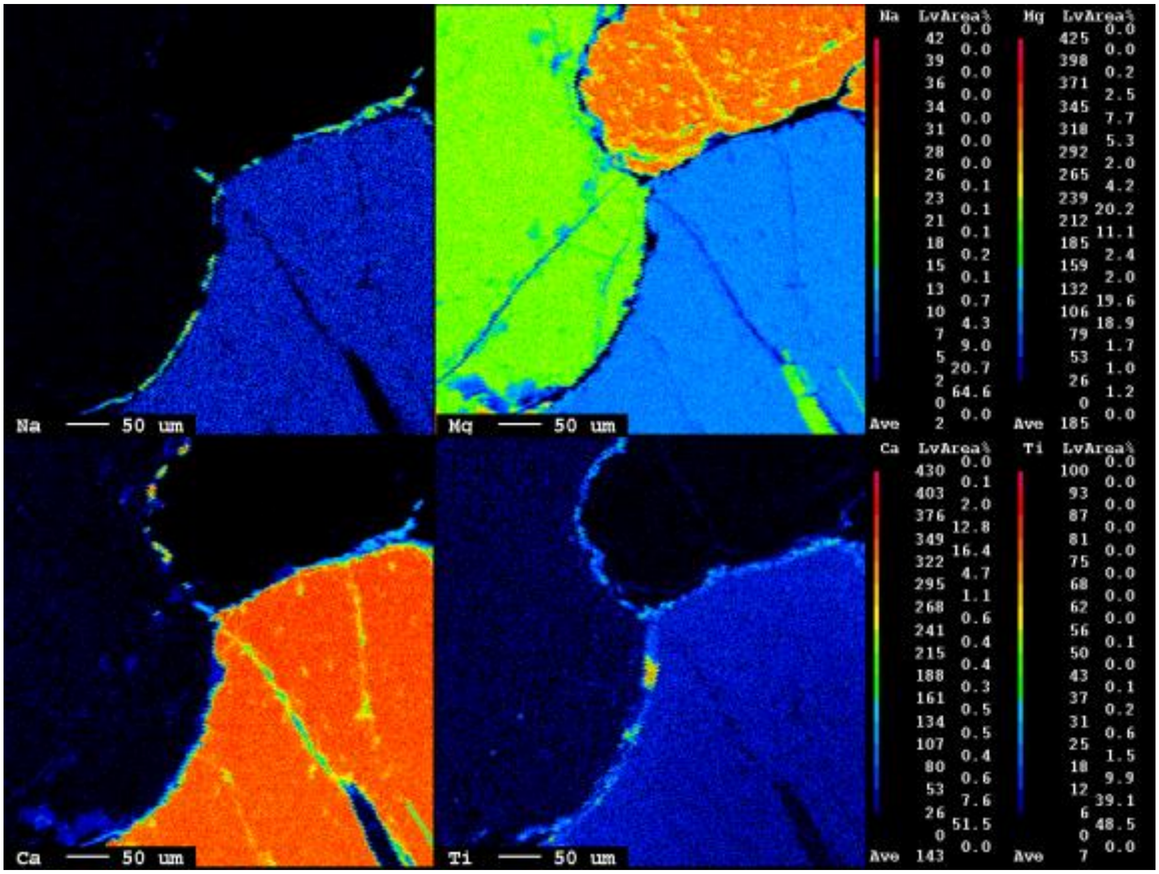

Figure A7.2b X-ray map showing example of grain boundaries in sample 07EB4.05

Note the high concentrations of Ti (lower right panel) along the grain boundaries and the higher relative concentrations along the rim of the cpx (lower right mineral)

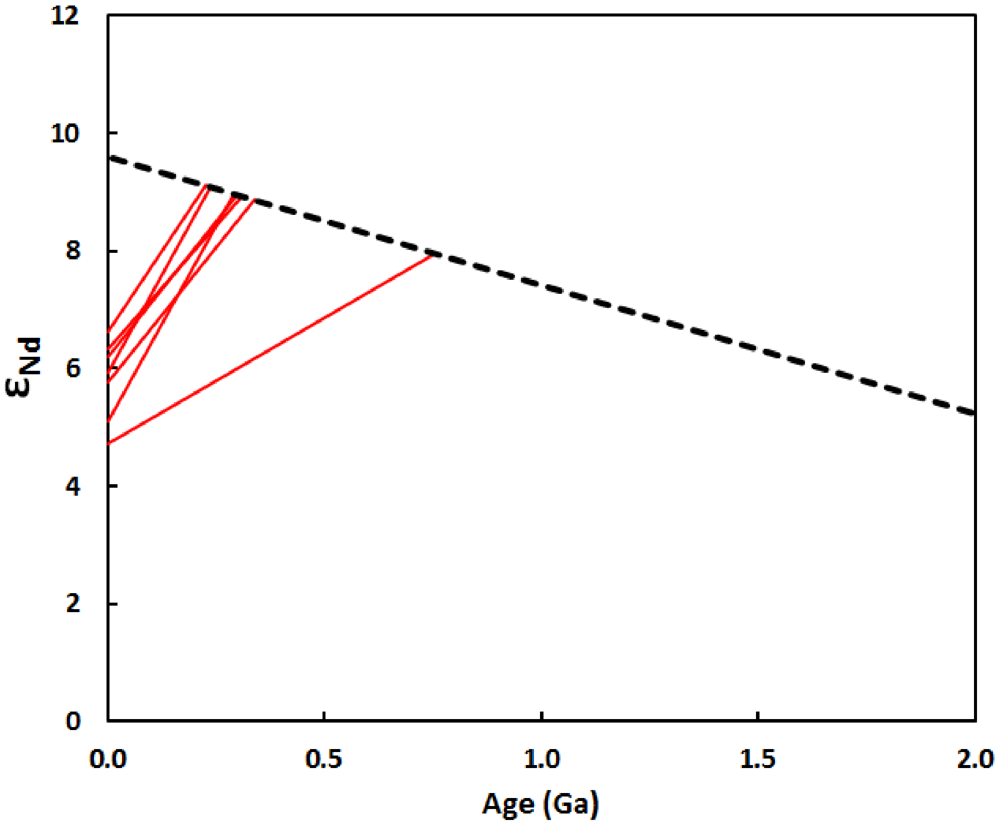

Figure A7.3 Plot of Nd depleted mantle model ages for Cerro Chato samples

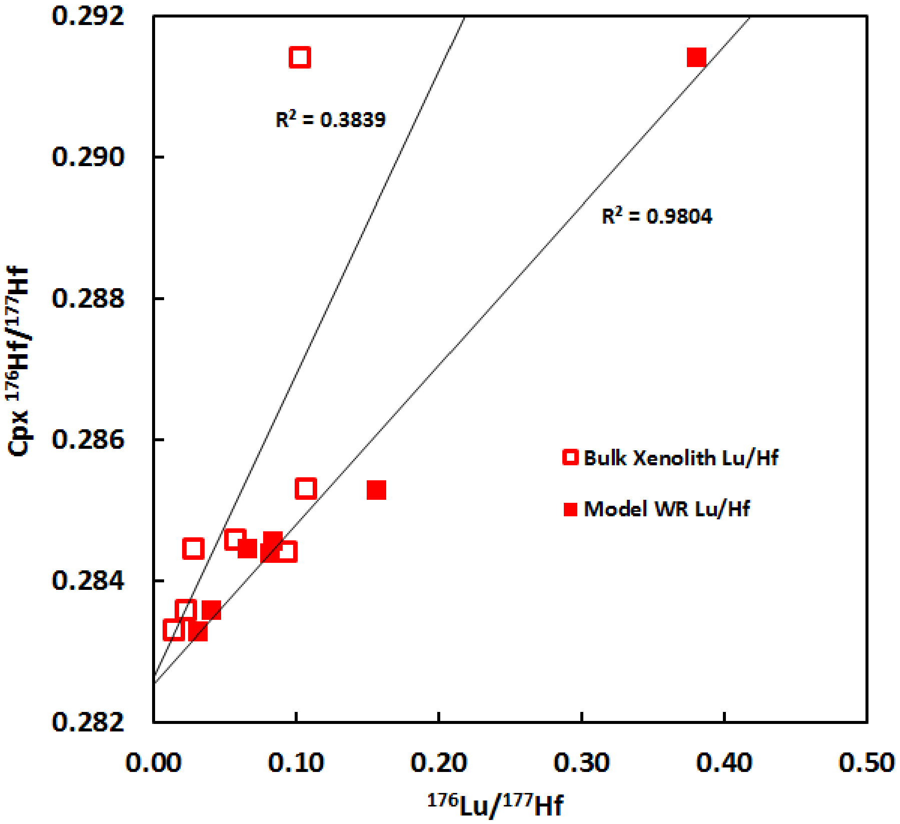

Figure A7.4 Plot of cpx ^{176}Hf/^{177}Hf versus ^{176}Lu/^{177}Hf using measured whole rock Lu/Hf and model whole rock Lu/Hf

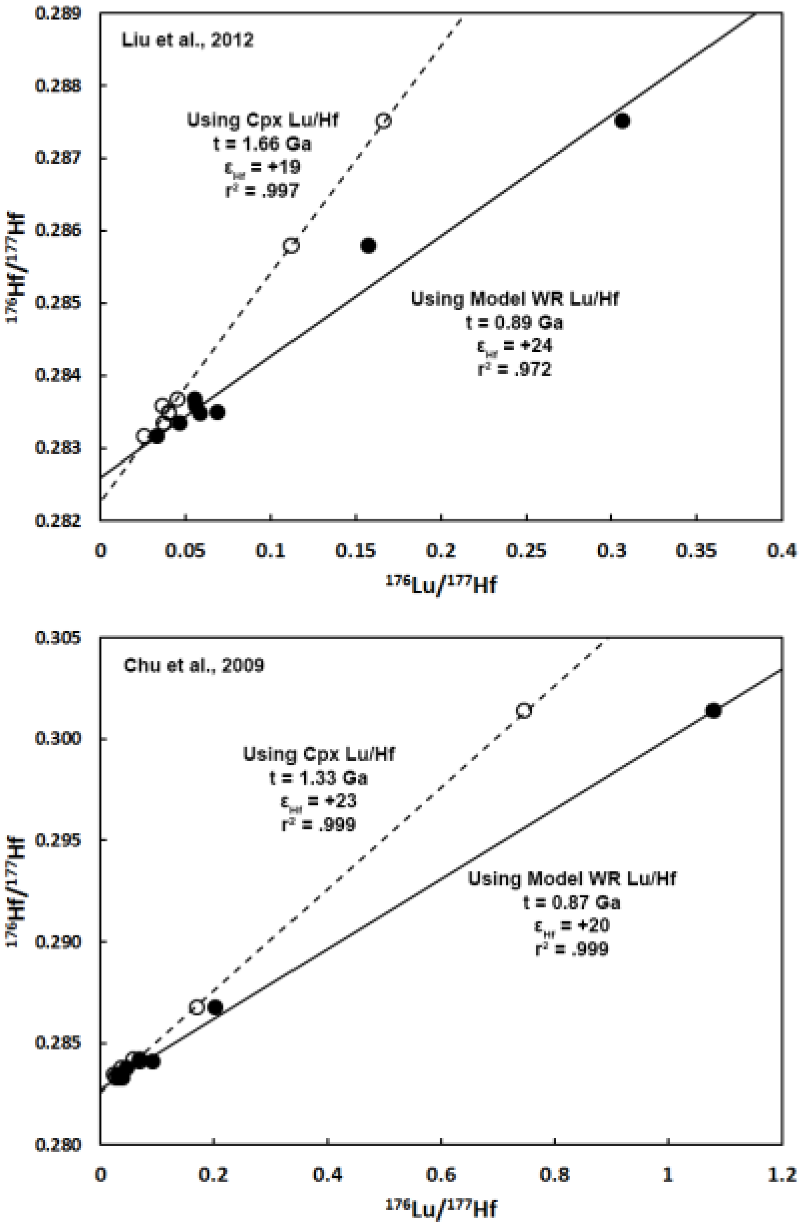

Figure A7.5 Comparison of ages from clinopyroxene Lu/Hf and whole rock Lu/Hf pseudoisochrons

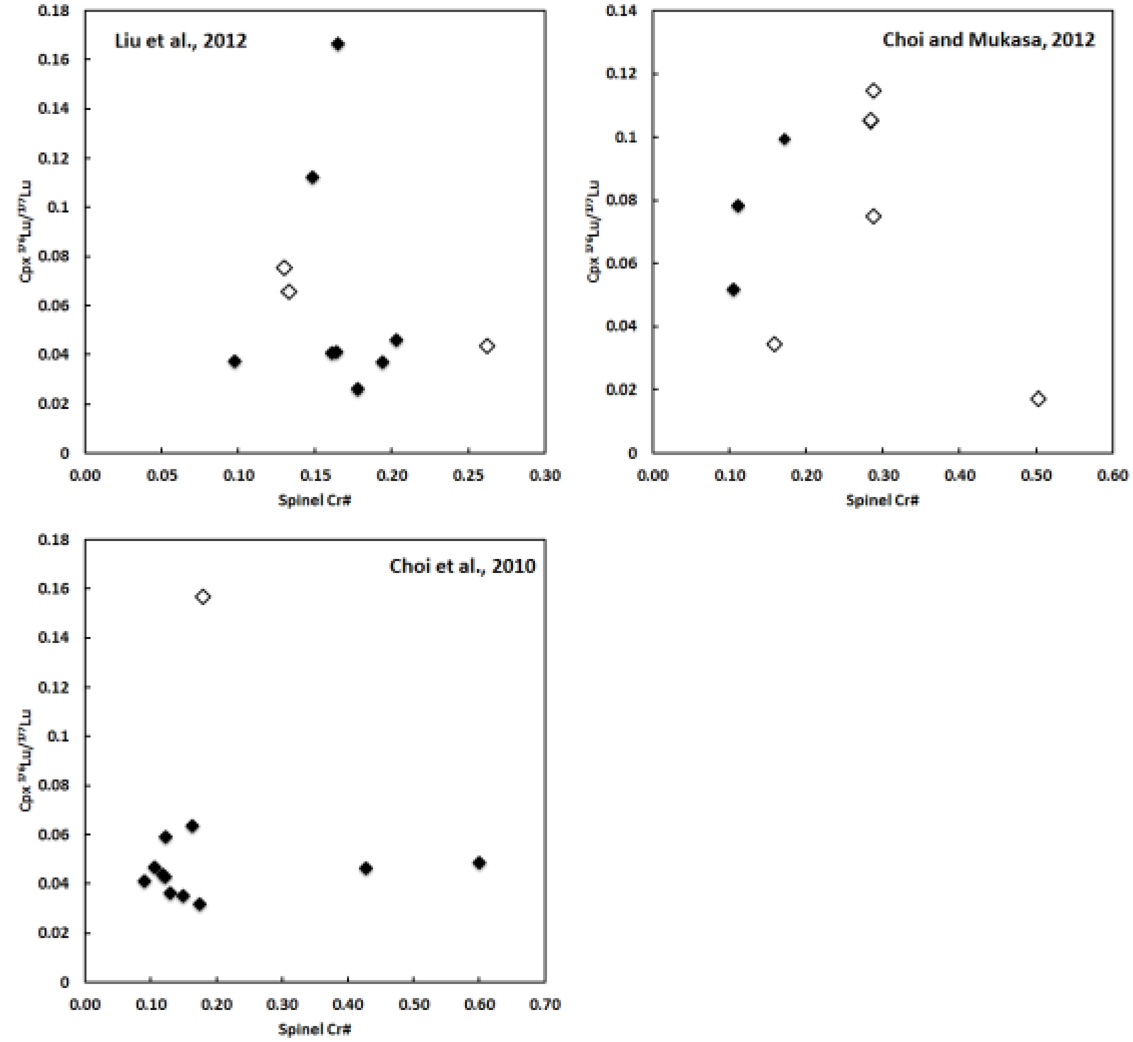

Figure A7.6 Plot of Lu/Hf versus spinel Cr# for several suites of SCLM-derived peridotite xenoliths

Conclusion

Mantle xenoliths provide a unique record of myriad upper mantle processes including melt depletion, metasomatism, and wholesale recycling of lithosphere into the convecting mantle. This dissertation describes how geochemical analysis of mantle xenoliths can be used to trace the chemical and physical evolution of Earth's mantle through deep time.

The xenolith suite at Elephant Butte samples the mantle beneath the central RGR and their composition indicates the existence of chemically stratified SCLM. Some xenoliths strongly resemble xenoliths from the adjacent Colorado Plateau and we interpret these to be sampling residual Proterozoic lithosphere beneath the central rift. The majority of xenoliths, however, have chemical compositions that resemble estimates for the composition of the convecting upper mantle. We interpret these to be derived from convecting mantle material that has recently accreted at the base of the Proterozoic lithosphere. Our model suggests that these samples are derived from shallow (<45km) depths, which requires significant thinning of the residual lithosphere that cannot be accounted by rift-related extension alone. Therefore, we suggest that a large portion of the Proterozoic lithospheric mantle beneath the central RGR was convectively removed and replaced by hot asthenospheric mantle, which has since cooled and is now physically part of the SCLM.

Mid-ocean ridge basalts (MORB), which form by partially melting convecting upper mantle material, have long been used to constrain the composition of the upper mantle. Using these mantle-derived melts to infer mantle composition has its drawbacks; most notably due to the fact that these accumulated melts tend to "smooth out" any heterogeneity is present in the source. Thus, direct sampling of the convecting upper mantle via abyssal peridotites and mantle xenoliths provides a more accurate sampling of the MORB source. Samples from myriad tectonic environments indicate that the upper mantle is quite heterogeneous and, as we discuss, extends to highly depleted isotopic compositions that are not observed in MORB. We show that these highly depleted domains are widely distributed and capable of generating melt if advected beneath mid-ocean ridges. To explain moderate isotopic compositions observed in MORB today, we suggest that MORB melts represent mixtures of melts generated from a highly heterogeneous upper mantle that includes isotopically enriched and depleted components. We also show that MORB can preferentially sample fertile components in the mantle, which would generally bias MORB isotopes towards enriched compositions.

The Lu-Hf system is a useful compliment to the Rb-Sr, Sm-Nd, and Re-Os systems for characterizing the melt depletion/re-enrichment history the upper mantle. However, as with any isotope system, care must be taken to ensure that the date is properly interpreted. We demonstrate that cpx Lu/Hf is not a suitable proxy for whole rock Lu/Hf when interpreting Lu-Hf pseudoisochrons. Use of cpx Lu/Hf for age determination in samples that have equilibrated above their Lu-Hf closure temperature can result in dramatic (20-40%) overestimation of apparent ages. We also show that the Lu/Hf – Hf isotope correlations that are commonly observed in suites of SCLM-derived xenoliths can be produced by mixing (e.g. metasomatic overprinting). This could explain the common lack of correlation between Hf isotopes and/or Lu/Hf ratios with indicators of melt-depletion. Although the Lu-Hf system is less susceptible to overprinting than the Sm-Nd system it is important to consider the extent to which samples have been metasomatised before attempting to interpret the age significance of Lu/Hf – Hf isotope correlations.

References

Agranier, A., Lee, C.T.A., 2007. Quantifying trace element disequilibria in mantle xenoliths and abyssal peridotites. Earth and Planetary Science Letters 257, 290-298.

Alibert, C., 1994. Peridotite Xenoliths from Western Grand-Canyon and the Thumb - a Probe into the Subcontinental Mantle of the Colorado Plateau. J Geophys Res-Sol Ea 99, 21605-21620.

Allegre, C.J., Turcotte, D.L., 1986. Implications of a Two-Component Marble-Cake Mantle. Nature 323, 123-127.

Aoki, K., 1981. Major element geochemistry of chromian spinel peridotite xenoliths in the Green Knobs kimberlite, New Mexico. Science Reports of the Tohoku University Series III, 127-130.

Audi, G., Bersillon, O., Blachot, J., Wapstra, A.H., 2003. The Nubase evaluation of nuclear and decay properties. Nuclear Physics A 729, 3-128.

Bachman, G.O., Mehnert, H.H., 1978. New K-Ar dates and the late Pliocene to Holocene geomorphic history of the central Rio Grande region, New Mexico. Geological Society of America Bulletin 89, 283.

Baldridge, W.S., 1979a. Mafic and Ultramafic Inclusion Suites from the Rio-Grande Rift (New-Mexico) and Their Bearing on the Composition and Thermal State of the Lithosphere. Journal of Volcanology and Geothermal Research 6, 319-351.

Baldridge, W.S., 1979b. Petrology and petrogenesis of Plio-Pleistocene basaltic rocks from the central Rio Grande rift, New Mexico, and their relation to rift structure. , in: Riecker, R.E. (Ed.), Rio Grande Rift Tectonics and Magmatism.

Baldridge, W.S., Damon, P.E., Shafiqullah, M., Bridwell, R.J., 1980. Evolution of the central Rio Grande Rift, New Mexico: New Potassium-Argon Ages. Earth and Planetary Science Letters 51, 309-321.

Beard, B.L., Glazner, A.F., 1995. Trace element and Sr and Nd isotopic composition of mantle xenoliths from the Big Pine volcanic field, California. J. Geophys. Res. 100, 4169-4179.

Bedini, R.M., Blichert-Toft, J., Boyet, M., Albarede, F., 2004. Isotopic constraints on the cooling of the continental lithosphere. Earth and Planetary Science Letters 223, 99-111.

Bedini, R.M., Bodinier, J.L., 1999. Distribution of incompatible trace elements between the constituents of spinel peridotite xenoliths: ICP-MS data from the East African Rift. Geochimica et Cosmochimica Acta 63, 3883-3900.

Bedini, R.M., Bodinier, J.L., Dautria, J.M., Morten, L., 1997. Evolution of LILE-enriched small melt fractions in the lithospheric mantle: a case study from the East African Rift. Earth and Planetary Science Letters 153, 67-83.

Bennett, V.C., Depaolo, D.J., 1987. Proterozoic crustal history of the western United States as determined by neodymium isotopic mapping. Geological Society of America Bulletin 99, 674.

Best, M.G., 1970. Kaersutite-peridotite inclusions and kindred megacrysts in basanitic lavas, Grand Canyon, Arizona. Contributions to Mineralogy and Petrology 27, 25-44.

Best, M.G., 1975. Amphibole-bearing Cumulate Inclusions, Grand Canyon, Arizona and their bearing on Silica-Undersaturated Hydrous Magmas in the Upper Mantle. Journal of Petrology 16, 212-236.

Bird, P., 1979. Continental Delamination and the Colorado Plateau. Journal of Geophysical Research 84, 7561-7571.

Bizimis, M., Griselin, M., Lassiter, J.C., Salters, V.J.M., Sen, G., 2007. Ancient recycled mantle lithosphere in the Hawaiian plume: Osmium-Hafnium isotopic evidence from peridotite mantle xenoliths. Earth and Planetary Science Letters 257, 259-273.

Bizimis, M., Sen, G., Salters, V.J.M., 2003. Hf-Nd isotope decoupling in the oceanic lithosphere: constraints from spinel peridotites from Oahu, Hawaii. Earth and Planetary Science Letters 217, 43-58.

Bizimis, M., Sen, G., Salters, V.J.M., Keshav, S., 2005. Hf-Nd-Sr isotope systematics of garnet pyroxenites from Salt Lake Crater, Oahu, Hawaii: Evidence for a depleted component in Hawaiian volcanism. Geochimica et Cosmochimica Acta 69, 2629-2646.

Blichert-Toft, J., Albarede, F., Kornprobst, J., 1999. Lu-Hf isotope systematics of garnet pyroxenites from Beni Bousera, Morocco: Implications for basalt origin. Science 283, 1303-1306.

Bodinier, J.I., Merlet, C., Bedini, R.M., Simien, F., Remaidi, M., Garrido, C.J., 1996. Distribution of niobium, tantalum, and other highly incompatible trace elements in the lithospheric mantle: The spinel paradox. Geochimica et Cosmochimica Acta 60, 545-550.

Boyet, M., Carlson, R.W., 2006. A new geochemical model for the Earth's mantle inferred from 146Sm-142Nd systematics. Earth and Planetary Science Letters 250, 254-268.

Brandon, A.D., Snow, J.E., Walker, R.J., Morgan, J.W., Mock, T.D., 2000. 190Pt/186Os and 187Re/187Os systematics of abyssal peridotites. Earth and Planetary Science Letters 177, 319-335.

Brandon, A.D., Walker, R.J., 2005. The debate over core–mantle interaction. Earth and Planetary Science Letters 232, 211-225.

Brey, G.P., Köhler, T., 1990. Geothermobarometry in Four-phase Lherzolites II. New Thermobarometers, and Practical Assessment of Existing Thermobarometers. Journal of Petrology 31, 1353-1378.

Brice, J.C., 1975. Some thermodynamic aspects of the growth of strained crystals. Journal of Crystal Growth 28, 249-253.

Brunelli, D., Seyler, M., Cipriani, A., Ottolini, L., Bonatti, E., 2006. Discontinuous melt extraction and weak refertilization of mantle peridotites at the Vema lithospheric section (Mid-Atlantic ridge). Journal of Petrology 47, 745-771.

Byerly, B.L., Lassiter, J.C., 2012. Evidence from mantle xenoliths for lithosphere removal beneath the central Rio Grande Rift. Earth and Planetary Science Letters 355-356, 82-93.

Byerly, B.L., Lassiter, J.C., 2014. Isotopically ultradepleted domains in the convecting upper mantle: Implications for MORB petrogenesis. Geology 42, 203-206

Carlson, R.W., Irving, A.J., Schulze, D.J., Hearn, B.C., 2004. Timing of Precambrian melt depletion and Phanerozoic refertilization events in the lithospheric mantle of the Wyoming Craton and adjacent Central Plains Orogen. Lithos 77, 453-472.

Carlson, R.W., Pearson, D.G., James, D.E., 2005. Physical, chemical, and chronological characteristics of continental mantle. Reviews of Geophysics 43, RG1001.

Cather, S.M., Chamberlin, R.M., Chapin, C.E., McIntosh, W.C., 1994. Stratigraphic consequences of episodic extension in the Lemitar Mountains, central Rio Grande rift, Geol. Soc. Amer. Spec. Pap., pp. 157-170.

Chapin, C.E., 1979. Evolution of the Rio Grande Rift - A Summary, in: Riecker, R.E. (Ed.), Rio Grande rift: tectonics and magmatism, pp. 1-5.

Chapin, C.E., Cather, S.M., 1994. Tectonic setting of the axial basins of the northern and central Rio Grande rift, Geol. Soc. Amer. Spec. Pap. , pp. 5-25.

Chatterjee, R.N., Byerly, B.L., Lassiter, J.C., 2011. Isotopic evidence from lavas and mantle xenoliths for a mixed asthenosphereic-lithospheric source for RIo Grande rift magmas. DI51A-2115 presented at 2011 Fall Meeting, AGU, San Francisco, Calif.

Cherniak, D.J., Hanchar, J.M., Watson, E.B., 1997a. Diffusion of tetravalent cations in zircon. Contributions to Mineralogy and Petrology 127, 383-390.

Cherniak, D.J., Hanchar, J.M., Watson, E.B., 1997b. Rare-earth diffusion in zircon. Chemical Geology 134, 289-301.

Choi, S.H., Mukasa, S.B., 2012. Lu-Hf and Sm-Nd isotope systematics of Korean spinel peridotites: A case for metasomatically induced Nd-Hf decoupling. Lithos 154, 263-276.

Choi, S.H., Mukasa, S.B., Zhou, X.-H., Xian, X.H., Andronikov, A.V., 2008. Mantle dynamics beneath East Asia constrained by Sr, Nd, Pb and Hf isotopic systematics of ultramafic xenoliths and their host basalts from Hannuoba, North China. Chemical Geology 248, 40-61.

Choi, S.H., Suzuki, K., Mukasa, S.B., Lee, J.I., Jung, H., 2010. Lu-Hf and Re-Os systematics of peridotite xenoliths from Spitsbergen, western Svalbard: Implications for mantle-crust coupling. Earth and Planetary Science Letters 297, 121-132.

Chu, Z.-Y., Wu, F.-Y., Walker, R.J., Rudnick, R.L., Pitcher, L., Puchtel, I.S., Yang, Y.-H., Wilde, S.A., 2009. Temporal Evolution of the Lithospheric Mantle beneath the Eastern North China Craton. Journal of Petrology 50, 1857-1898.

Cipriani, A., Brueckner, H.K., Bonatti, E., Brunelli, D., 2004. Oceanic crust generated by elusive parents: Sr and Nd isotopes in basalt-peridotite pairs from the Mid-Atlantic Ridge. Geology 32, 657-660.

Condie, K.C., Cox, J., O'Reilly, S.Y., Griffin, W.L., Kerrich, R., 2004. Distribution of high field strength and rare earth elements in mantle and lower crustal xenoliths from the southwestern United States: The role of grain-boundary phases. Geochimica et Cosmochimica Acta 68, 3919-3942.

Connelly, J., Ulfbeck, D., Thrane, K., Bizzarro, M., Housh, T., 2006. A method for purifying Lu and Hf for analyses by MC-ICP-MS using TODGA resin. Chemical Geology 233, 126-136.

Conrad, C.P., Molnar, P., 1997. The growth of Rayleigh–Taylor-type instabilities in the lithosphere for various rheological and density structures. Geophys J Int 129, 95-112.

Dick, H.J.B., Bullen, T., 1984. Chromian spinel as a petrogenetic indicator in abyssal and alpine-type peridotites and spatially associated lavas. Contributions to Mineralogy and Petrology 86, 54-76.

Downes, H., 2001. Formation and modification of the shallow sub-continental lithospheric mantle: a review of geochemical evidence from ultramafic xenolith suites and tectonically emplaced ultramafic massifs of western and central Europe. Journal of Petrology 42, 233-250.

Eby, G.N., Lloyd, F.E., Woolley, A.R., 2009. Geochemistry and petrogenesis of the Fort Portal, Uganda, extrusive carbonatite. Lithos 113, 785-800.

Eggins, S.M., Rudnick, R.L., McDonough, W.F., 1998. The composition of peridotites and their minerals: A laser-ablation ICP-MS study. Earth and Planetary Science Letters 154, 53-71.

Ehrenberg, S.N., 1982. Petrogenesis of Garnet Lherzolite and Megacrystalline Nodules from the Thumb, Navajo Volcanic Field. Journal of Petrology 23, 507-547.

Eiler, J.M., Schiano, P., Kitchen, N., Stolper, E.M., 2000. Oxygen-isotope evidence for recycled crust in the sources of mid-ocean-ridge basalts. Nature 403, 530-534.

England, P., Houseman, G., 1989. Extension During Continental Convergence, With Application to the Tibetan Plateau. J. Geophys. Res. 94, 17561-17579.

Esser, B.K., Turekian, K.K., 1993. The osmium isotopic composition of the continental crust. Geochimica et Cosmochimica Acta 57, 3093-3104.

Frey, F.A., Green, D.H., 1974. Mineralogy, Geochemistry and Origin of Ilherzolite Inclusions in Victorian Basanites. Geochimica et Cosmochimica Acta 38, 1023-1059.

Frey, F.A., Prinz, M., 1978. Ultramafic inclusions from San Carlos, Arizona: petrologic and geochemical data bearing on their petrogenesis. Earth and Planetary Science Letters 38, 129-176.

Galer, S.J.G., Onions, R.K., 1989. Chemical and Isotopic Studies of Ultramafic Inclusions from the San-Carlos Volcanic Field, Arizona - a Bearing on Their Petrogenesis. Journal of Petrology 30, 1033-1064.

Gao, S., Rudnick, R.L., Carlson, R.W., McDonough, W.F., Liu, Y.-S., 2002. Re-Os evidence for replacement of ancient mantle lithosphere beneath the North China craton. Earth and Planetary Science Letters 198, 307-322.

Gao, W., Grand, S.P., Baldridge, W.S., Wilson, D., West, M., Ni, J.F., Aster, R., 2004. Upper mantle convection beneath the central Rio Grande rift imaged by P and S wave tomography. J Geophys Res-Sol Ea 109.

Garrido, C.J., Bodinier, J.-L., Alard, O., 2000. Incompatible trace element partitioning and residence in anhydrous spinel peridotites and websterites from the Ronda orogenic peridotite. Earth and Planetary Science Letters 181, 341-358.

Ghiorso, M.S., Hirschmann, M.M., Reiners, P.W., Kress, V.C., III, 2002. The pMELTS: A revision of MELTS for improved calculation of phase relations and major element partitioning related to partial melting of the mantle to 3 GPa. Geochem. Geophys. Geosyst. 3, 1030.

Green, D.H., Ringwood, A.E., 1970. Mineralogy of peridotitic compositions under upper mantle conditions. Physics of the Earth and Planetary Interiors 3, 359-371.

Griffin, W.L., Andi, Z., O'Reilly, S.Y., Ryan, C.G., 1998. Phanerozoic evolution of the lithosphere beneath the Sino-Korean craton, Mantle Dynamics and Plate Interactions in East Asia. AGU, Washington, DC, pp. 107-126.

Handler, M.R., Bennett, V.C., 1999. Behaviour of Platinum-group elements in the subcontinental mantle of eastern Australia during variable metasomatism and melt depletion. Geochimica et Cosmochimica Acta 63, 3597-3618.

Hart, S.R., 1988. Heterogeneous mantle domains: signatures, genesis and mixing chronologies. Earth and Planetary Science Letters 90, 273-296.

Hart, S.R., Dunn, T., 1993. Experimental cpx/melt partitioning of 24 trace elements. Contributions to Mineralogy and Petrology 113, 1-8.

Harvey, J., Gannoun, A., Burton, K.W., Rogers, N.W., Alard, O., Parkinson, I.J., 2006. Ancient melt extraction from the oceanic upper mantle revealed by Re-Os isotopes in abyssal peridotites from the Mid-Atlantic ridge. Earth and Planetary Science Letters 244, 606-621.

Harvey, J., Yoshikawa, M., Hammond, S.J., Burton, K.W., 2012. Deciphering the Trace Element Characteristics in Kilbourne Hole Peridotite Xenoliths: Melt-Rock Interaction and Metasomatism beneath the Rio Grande Rift, SW USA. Journal of Petrology 53, 1709-1742.

Hauri, E.H., Wagner, T.P., Grove, T.L., 1994. Experimental and natural partitioning of Th, U, Pb and other trace elements between garnet, clinopyroxene and basaltic melts. Chemical Geology 117, 149-166.

Hellebrand, E., Snow, J.E., Dick, H.J.B., Hofmann, A.W., 2001. Coupled major and trace elements as indicators of the extent of melting in mid-ocean-ridge peridotites. Nature 410, 677-681.

Hellebrand, E., Snow, J.E., Hoppe, P., Hoffman, A.W., 2002. Garnet-field Melting and Late-stage Refertilization in 'Residual' Abyssal Peridotites from the Central Indian Ridge. Journal of Petrology 43, 2305-2338.

Hellebrand, E., Snow, J.E., Mostefaoui, S., Hoppe, P., 2005. Trace element distribution between orthopyroxene and clinopyroxene in peridotites from the Gakkel Ridge: a SIMS and NanoSIMS study. Contributions to Mineralogy and Petrology 150, 486-504.

Hirschmann, M.M., Stolper, E.M., 1996. A possible role for garnet pyroxenite in the origin of the "garnet signature" in MORB. Contributions to Mineralogy and Petrology 124, 185-208.

Hirth, G., Kohlstedt, D.L., 1996. Water in the oceanic upper mantle: implications for rheology, melt extraction and the evolution of the lithosphere. Earth and Planetary Science Letters 144, 93-108.

Houseman, G.A., Mckenzie, D.P., Molnar, P., 1981. Convective Instability of a Thickened Boundary-Layer and Its Relevance for the Thermal Evolution of Continental Convergent Belts. Journal of Geophysical Research 86, 6115-6132.

Houseman, G.A., Molnar, P., 1997. Gravitational (Rayleigh-Taylor) instability of a layer with non-linear viscosity and convective thinning of continental lithosphere. Geophys J Int 128, 125-150.

Humphreys, E., Hessler, E., Dueker, K., Farmer, G.L., Erslev, E., Atwater, T., 2003. How Laramide-Age Hydration of North American Lithosphere by the Farallon Slab Controlled Subsequent Activity in the Western United States. International Geology Review 45, 575-595.

Humphreys, E.D., 1995. Post-Laramide removal of the Farallon slab, western United States. Geology 23, 987.

Ionov, D.A., Shirey, S.B., Weis, D., Brügmann, G., 2006. Os–Hf–Sr–Nd isotope and PGE systematics of spinel peridotite xenoliths from Tok, SE Siberian craton: Effects of pervasive metasomatism in shallow refractory mantle. Earth and Planetary Science Letters 241, 47-64.

Irving, A.J., 1974. Pyroxene-rich ultramafic xenoliths in the Newer Basalts of Victoria, Australia. Neues Jahrbuch für Mineralogie - Abhandlungen 120.

Irving, A.J., 1980. Petrology and Geochemistry of Composite Ultramafic Xenoliths in Alkalic Basalts and Implications for Magmatic Processes within the Mantle. Am J Sci 280, 389-426.

Ishikawa, A., Pearson, D.G., Dale, C.W., 2011. Ancient Os isotope signatures from the Ontong Java Plateau lithosphere: Tracing lithospheric accretion history. Earth and Planetary Science Letters 301, 159-170.

Jaques, A.L., Green, D.H., 1980. ANHYDROUS MELTING OF PERIDOTITE AT 0-15 KB PRESSURE AND THE GENESIS OF THOLEIITIC BASALTS. Contributions to Mineralogy and Petrology 73, 287-310.

Johnson, C.M., Beard, B.L., 1993. Evidence from hafnium isotopes for ancient sub-oceanic mantle beneath the Rio Grande rift. Nature 362, 441-444.

Johnson, K.T.M., Dick, H.J.B., Shimizu, N., 1990. Melting in the upper oceanic mantle - an ion microprobe study of diopsides in abyssal peridotites. J Geophys Res-Solid 95, 2661-2678.

Kalfoun, F., Ionov, D., Merlet, C., 2002. HFSE residence and Nb/Ta ratios in metasomatised, rutile-bearing mantle peridotites. Earth and Planetary Science Letters 199, 49-65.

Kay, R.W., Kay, S.M., 1991. Creation and Destruction of Lower Continental-Crust. Geol Rundsch 80, 259-278.

Kay, R.W., Kay, S.M., 1993. Delamination and Delamination Magmatism. Tectonophysics 219, 177-189.

Keller, G.R., Braile, L.W., Morgan, P., 1979. Crustal Structure, Geophysical Models and Contemporary Tectonism of the Colorado Plateau. Tectonophysics 61, 131-147.

Keller, G.R., Morgan, P., Seager, W.R., 1990. Crustal structure, gravity anomalies and heat flow in the southern Rio Grande rift and their relationship to extensional tectonics. Tectonophysics 174, 21-37.

Kempton, P.D., 1987. Mineralogic and Geochemical Evidence for Differing Styles of metasomatism in spinel lherzolite xenoliths: enriched mantle source regions of basalts?, in: Menzies, M.A., Hawkesworth, C.J. (Eds.), Mantle Metasomatism. Academic Press, London.

Kil, Y., Wendlandt, R.F., 2004. Pressure and temperature evolution of upper mantle under the Rio Grande Rift. Contributions to Mineralogy and Petrology 148, 265-280.

Kil, Y., Wendlandt, R.F., 2007. Depleted and enriched mantle processes under the Rio Grande rift: spinel peridotite xenoliths. Contributions to Mineralogy and Petrology 154, 135-151.

Kleine, T., Munker, C., Mezger, K., Palme, H., 2002. Rapid accretion and early core formation on asteroids and the terrestrial planets from Hf-W chronometry. Nature 418, 952-955.

Klemme, S., O'Neill, H.S., 2000. The near-solidus transition from garnet lherzolite to spinel lherzolite. Contributions to Mineralogy and Petrology 138, 237-248.

Laughlin, A.W., Perry, F.V., Damon, P.E., Shafiqullah, M., WoldeGabriel, G., McIntosh, W.C., Harrington, C.D., Wells, S.G., Drake, P.G., 1993. Geochronology of Mount Taylor, Cebollita Mesa, and Zuni-Bandera volcanic fields, Cibola County, New Mexico. New Mexico Geology 15.

Lawton, T.F., McMillan, N.J., 1999. Arc abandonment as a cause for passive continental rifting: Comparison of the Jurassic Mexican Borderland rift and the Cenozoic Rio Grande rift. Geology 27, 779-782.

Lazarov, M., Brey, G.P., Weyer, S., 2012. Evolution of the South African mantle-a case study of garnet peridotites from the Finsch diamond mine (Kaapvaal craton); Part 2: Multiple depletion and re-enrichment processes. Lithos 154, 210-223.

Le Pourhiet, L., Gurnis, M., Saleeby, J., 2006. Mantle instability beneath the Sierra Nevada mountains in California and Death Valley extension. Earth and Planetary Science Letters 251, 104-119.

Lee, C.-T., Yin, Q., Rudnick, R.L., Jacobsen, S.B., 2001a. Preservation of ancient and fertile lithospheric mantle beneath the southwestern United States. Nature 411, 69-73.

Lee, C.-T.A., Harbert, A., Leeman, W.P., 2007. Extension of lattice strain theory to mineral/mineral rare-earth element partitioning: An approach for assessing disequilibrium and developing internally consistent partition coefficients between olivine, orthopyroxene, clinopyroxene and basaltic melt. Geochimica et Cosmochimica Acta 71, 481-496.

Lee, C.-T.A., Luffi, P., Plank, T., Dalton, H., Leeman, W.P., 2009. Constraints on the depths and temperatures of basaltic magma generation on Earth and other terrestrial planets using new thermobarometers for mafic magmas. Earth and Planetary Science Letters 279, 20-33.

Lee, C.T., Rudnick, R.L., Brimhall, G.H., 2001b. Deep lithospheric dynamics beneath the Sierra Nevada during the Mesozoic and Cenozoic as inferred from xenolith petrology. Geochemistry Geophysics Geosystems 2.

Lee, C.T., Yin, Q.Z., Rudnick, R.L., Chesley, J.T., Jacobsen, S.B., 2000. Osmium isotopic evidence for mesozoic removal of lithospheric mantle beneath the Sierra Nevada, California. Science 289, 1912-1916.

Li, Z.-X.A., Lee, C.-T.A., Peslier, A.H., Lenardic, A., Mackwell, S.J., 2008. Water contents in mantle xenoliths from the Colorado Plateau and vicinity: Implications for the mantle rheology and hydration-induced thinning of continental lithosphere. Journal of Geophysical Research 113.

Liang, Y., Sun, C., Yao, L., 2013. A REE-in-two-pyroxene thermometer for mafic and ultramafic rocks. Geochimica et Cosmochimica Acta 102, 246-260.

Lin, W., Wang, Q., 2006. Late Mesozoic extensional tectonics in the North China block: a crustal response to subcontinental mantle removal? Bulletin de la Societe Geologique de France 177, 287-297.

Liu, C.Z., Snow, J.E., Hellebrand, E., Brugmann, G., von der Handt, A., Buchl, A., Hofmann, A.W., 2008. Ancient, highly heterogeneous mantle beneath Gakkel ridge, Arctic Ocean. Nature 452, 311-316.

Liu, J.G., Carlson, R.W., Rudnick, R.L., Walker, R.J., Gao, S., Wu, F.Y., 2012. Comparative Sr-Nd-Hf-Os-Pb isotope systematics of xenolithic peridotites from Yangyuan, North China Craton: Additional evidence for a Paleoproterozoic age. Chemical Geology 332, 1-14.

Lorand, J.-P., 1990. Are spinel Iherzolite xenoliths representative of the abundance of sulfur in the upper mantle? Geochimica et Cosmochimica Acta 54, 1487-1492.

Luffi, P., Saleeby, J.B., Lee, C.-T.A., Ducea, M.N., 2009. Lithospheric mantle duplex beneath the central Mojave Desert revealed by xenoliths from Dish Hill, California. Journal of Geophysical Research 114.

Mack, G.H., Nightengale, A.L., Seager, W.R., Clemons, R.E., 1994. The Oligocene Goodsight-Cedar Hills half graben near Las Cruces and its implications to the evolution of the Mogollon-Datil volcanic field and to the southern Rio Grande rift, in: Chamberlin, R.M., Kues, B.S., Cather, S.M., Barker, J.M., McIntosh, W.C. (Eds.), New Mexico Geological Society Guidebook 45. NMGS, pp. 135-142.

Maclennan, J., 2008. Lead isotope variability in olivine-hosted melt inclusions from Iceland. Geochimica et Cosmochimica Acta 72, 4159-4176.

McDonough, W.F., 1990. Constraints on the Composition of the Continental Lithospheric Mantle. Earth and Planetary Science Letters 101, 1-18.

McDonough, W.F., Sun, S.s., 1995. The composition of the Earth. Chemical Geology 120, 223-253.

McMillan, N.J., 1998. Temporal and spatial magmatic evolution of the Rio Grande rift, in: Mack, G.H., Austin, G.S., Barker, J.M. (Eds.), New Mex. Geol. Soc. Guidebook 49. NMGS, pp. 107-116.

McMillan, N.J., Dickin, A.P., Haag, D.H., 2000. Evolution of magma source regions in the Rio Grande rift, southern New Mexico. GSA Bulletin 112, 1582-1593.

Meisel, T., Walker, R.J., Irving, A.J., Lorand, J.-P., 2001. Osmium isotopic compositions of mantle xenoliths: A global perspective. Geochemica et Cosmochimica Acta 65, 1311-1323.

Meissner, R., Mooney, W., 1998. Weakness of the lower continental crust: a condition for delamination, uplift, and escape. Tectonophysics 296, 47-60.

Menzies, M.A., 1990. Petrology and geochemistry of continental mantle: an historical perspective, in: Menzies, M.A. (Ed.), Continental Mantle. Oxford University Press, New York, p. 184.

Menzies, M.A., Leeman, W.P., Hawkesworth, C.J., 1983. Isotope Geochemistry of Cenozoic Volcanic-Rocks Reveals Mantle Heterogeneity Below Western USA. Nature 303, 205-209.

Menzies, M.A., Rogers, N., Tindle, A., Hawkesworth, C., 1987. Metasomatic and enrichment processes in lithospheric peridotites, an effect of asthenosphere-lithosphere interaction, in: Menzies, M.A., C.J., H. (Eds.), Mantle Metasomatism. Academic Press Inc., London, pp. 313-361.

Morency, C., Doin, M.P., 2004. Numerical simulations of the mantle lithosphere delamination. J Geophys Res-Sol Ea 109.

Mukasa, S.B., Wilshire, H.G., 1997. Isotopic and trace element compositions of upper mantle and lower crustal xenoliths, Cima volcanic field, California: Implications for evolution of the subcontinental lithospheric mantle. J. Geophys. Res. 102, 20133-20148.

Nelson, B.K., DePaolo, D.J., 1985. Rapid production of continental crust 1.7 to 1.9 b.y. ago: Nd isotopic evidence from the basement of the North American mid-continent. GSA Bulletin 96, 746-754.

Niu, Y.L., 1997. Mantle melting and melt extraction processes beneath ocean ridges: Evidence from abyssal peridotites. Journal of Petrology 38, 1047-1074.

Niu, Y.L., 2004. Bulk-rock major and trace element compositions of abyssal peridotites: Implications for mantle melting, melt extraction and post-melting processes beneath mid-ocean ridges. Journal of Petrology 45, 2423-2458.

O'Neill, H.S.C., 1981. The Transition Between Spinel Lherzolite and Garnet Lherzolite, and Its Use as a Geobarometer. Contributions to Mineralogy and Petrology 77, 185-194.

O'Reilly, S.Y., Griffin, W.L., 2000. Apatite in the mantle: implications for metasomatic processes and high heat production in Phanerozoic mantle. Lithos 53, 217-232.

O'Reilly, S.Y., Zhang, M., Griffin, W.L., Begg, G., Hronsky, J., 2009. Ultradeep continental roots and their oceanic remnants: A solution to the geochemical "mantle reservoir" problem? Lithos 112, Supplement 2, 1043-1054.

Pearson, D.G., 1999. The age of continental roots. Lithos 48, 171-194.

Pearson, D.G., Carlson, R.W., Shirey, S.B., Boyd, F.R., Nixon, P.H., 1995. Stabilization of Archean Lithospheric Mantle - a Re-Os Isotope Study of Peridotite Xenoliths from the Kaapvaal Craton. Earth and Planetary Science Letters 134, 341-357.

Pearson, D.G., Nowell, G.M., 2004. Re-Os and Lu-Hf isotope constraints on the origin and age of pyroxenites from the Beni Bousera peridotite massif implications for mixed peridotite-pyroxenite mantle sources. Journal of Petrology 45, 439-455.

Perry, F.V., Baldridge, W.S., DePaolo, D.J., 1987. Role of Asthenosphere and Lithosphere in the Genesis of Late Cenozoic Basaltic Rocks From the Rio Grande Rift and Adjacent Regions of the Southwestern United States. Journal of Geophysical Research 92, 9193-9213.

Rampone, E., Hofmann, A.W., 2012. A global overview of isotopic heterogeneities in the oceanic mantle. Lithos 148, 247-261.

Reiter, M., Eggleston, R.E., Broadwell, B.R., Minier, H., 1986. Estimates of Terrestrial Heat Flow From Deep Petroleum Tests Along the Rio Grande Rift in Central and Southern New Mexico. Journal of Geophysical Research 91, 6225-6245.

Riter, J.C.A., 1999. Geochemical and tectonic evolution of the Colorado Plateau mantle lithosphere: evidence from Grand Canyon mantle xenoliths, Department of Geological Sciences. University of Texas at Austin, Austin.

Riter, J.C.A., Smith, D., 1996. Xenolith constraints on the thermal history of the mantle below the Colorado Plateau. Geology 24, 267.

Roden, M.F., Irving, A.J., Rama Murthy, V., 1988. Isotopic and trace element composition of the upper mantle beneath a young continental rift: Results from Kilbourne Hole, New Mexico. Geochemica et Cosmochimica Acta 52, 461-473.

Roden, M.F., Shimizu, N., 1993. Ion Microprobe Analyses Bearing on the Composition of the Upper-Mantle beneath the Basin and Range and Colorado Plateau Provinces. J Geophys Res-Sol Ea 98, 14091-14108.

Rudnick, R.L., Fountain, D.M., 1995. Nature and Composition of the Continental Crust: A Lower Crustal Perspective. Reviews of Geophysics 33, 267-309.

Salters, V.J.M., Dick, H.J.B., 2002. Mineralogy of the mid-ocean-ridge basalt source from neodymium isotopic composition of abyssal peridotites. Nature 418, 68-72.

Salters, V.J.M., Sachi-Kocher, A., Dick, H., 2011. Ultra Depleted Mantle at the Gakkel Ridge Based on Hafnium and Neodymium Isotopes, National High Magnetic Field Laboratory Research Report. National High Magnetic Field Laboratory.

Salters, V.J.M., Stracke, A., 2004. Composition of the depleted mantle. Geochemistry Geophysics Geosystems 5.

Salters, V.J.M., Zindler, A., 1995. Extreme 176Hf/177Hf in the sub-oceanic mantle. Earth and Planetary Science Letters 129, 13-30.

Scherer, E., Munker, C., Mezger, K., 2001. Calibration of the lutetium-hafnium clock. Science 293, 683-687.

Scherer, E.E., Cameron, K.L., Blichert-Toft, J., 2000. Lu-Hf garnet geochronology: Closure temperature relative to the Sm-Nd system and the effects of trace mineral inclusions. Geochimica Et Cosmochimica Acta 64, 3413-3432.

Schmidberger, S.S., Simonetti, A., Francis, D., Gariepy, C., 2002. Probing Archean lithosphere using the Lu-Hf isotope systematics of peridotite xenoliths from Somerset Island kimberlites, Canada. Earth and Planetary Science Letters 197, 245-259.

Schott, B., Schmeling, H., 1998. Delamination and detachment of a lithospheric root. Tectonophysics 296, 225-247.

Schutt, D.L., Lesher, C.E., 2006. Effects of melt depletion on the density and seismic velocity of garnet and spinel lherzolite. Journal of Geophysical Research: Solid Earth 111, B05401.

Sen, G., Frey, F.A., Shimizu, N., Leeman, W.P., 1993. Evolution of the lithosphere beneath Oahu, Hawaii: rare earth element abundances in mantle xenoliths. Earth and Planetary Science Letters 119, 53-69.

Seyler, M., Lorand, J.P., Dick, H.J.B., Drouin, M., 2007. Pervasive melt percolation reactions in ultra-depleted refractory harzburgites at the Mid-Atlantic Ridge, 15 degrees 20 ' N: ODP Hole 1274A. Contributions to Mineralogy and Petrology 153, 303-319.

Shaw, J.E., Baker, J.A., Kent, A.J.R., Ibrahim, K.M., Menzies, M.A., 2007. The Geochemistry of the Arabian Lithospheric Mantle-a Source for Intraplate Volcanism? Journal of Petrology 48, 1495-1512.

Shimizu, N., 1998. The geochemistry of olivine-hosted melt inclusions in a FAMOUS basalt ALV519-4-1. Physics of the Earth and Planetary Interiors 107, 183-201.

Shirey, S.B., Walker, R.J., 1998. The Re-Os Isotope System in Cosmochemistry and High-Temperature Geochemistry. Annual Review of Earth and Planetary Sciences 26, 423-500.

Shu, Q., Brey, G.P., Gerdes, A., Hoefer, H.E., 2014. Mantle eclogites and garnet pyroxenites – the meaning of two-point isochrons, Sm–Nd and Lu–Hf closure temperatures and the cooling of the subcratonic mantle. Earth and Planetary Science Letters 389, 143-154.

Smith, D., 2000. Insights into the evolution of the uppermost continental mantle from xenolith localities on and near the Colorado Plateau and regional comparisons. Journal of Geophysical Research 105, 16769-16781.

Smith, D., 2010. Antigorite Peridotite, Metaserpentinite, and other Inclusions within Diatremes on the Colorado Plateau, SW USA: Implications for the Mantle Wedge during Low-angle Subduction. Journal of Petrology 51, 1355-1379.

Smith, D., Alexis Riter, J.C., Mertzman, S.A., 1999. Water-rock interactions, orthopyroxene growth, and Si-enrichment in the mantle: evidence in xenoliths from the Colorado Plateau, southwestern United States. Earth and Planetary Science Letters 165, 45-54.

Smith, D., Levy, S., 1976. Petrology of the Green Knobs diatreme and implications for the upper mantle below the Colorado Plateau. Earth and Planetary Science Letters 29, 107-125.

Smith, D., Riter, J.C.A., 1997. Genesis and evolution of low-Al orthopyroxene in spinel peridotite xenoliths, Grand Canyon field, Arizona, USA. Contributions to Mineralogy and Petrology 127, 391-404.

Snow, J.E., Hart, S.R., Dick, H.J.B., 1994. Nd and Sr isotope evidence linking mid-ocean-ridge basalts and abyssal peridotites. Nature 371, 57-60.

Snow, J.E., Reisberg, L., 1995. Os Isotopic Systematics of the Morb Mantle - Results from Altered Abyssal Peridotites. Earth and Planetary Science Letters 133, 411-421.

Song, T.-R.A., Helmberger, D.V., 2007. A depleted, destabilized continental lithosphere near the Rio Grande rift. Earth and Planetary Science Letters 262, 175-184.

Standish, J.J., Hart, S.R., Blusztajn, J., Dick, H.J.B., Lee, K.L., 2002. Abyssal peridotite osmium isotopic compositions from cr-spinel. Geochem. Geophys. Geosyst. 3, 1004.

Stracke, A., Snow, J.E., Hellebrand, E., von der Handt, A., Bourdon, B., Birbaum, K., Günther, D., 2011. Abyssal peridotite Hf isotopes identify extreme mantle depletion. Earth and Planetary Science Letters 308, 359-368.

Sun, C., Liang, Y., 2012. Distribution of REE between clinopyroxene and basaltic melt along a mantle adiabat: effects of major element composition, water, and temperature. Contributions to Mineralogy and Petrology 163, 807-823.

Sun, S.s., McDonough, W.F., 1989. Chemical and isotopic systematics of oceanic basalts: implications for mantle composition and processes. Geological Society, London, Special Publications 42, 313-345.

Turcotte, D.L., Schubert, G., 2002. Geodynamics, 2nd ed. Cambridge University Press, Cambridge.

Van Orman, J., Grove, T., Shimizu, N., 2001. Rare earth element diffusion in diopside: influence of temperature, pressure, and ionic radius, and an elastic model for diffusion in silicates. Contributions to Mineralogy and Petrology 141, 687-703.

Vervoort, J.D., Blichert-Toft, J., 1999. Evolution of the depleted mantle: Hf isotope evidence from juvenile rocks through time. Geochimica Et Cosmochimica Acta 63, 533-556.

Wallner, H., Schmeling, H., 2010. Rift induced delamination of mantle lithosphere and crustal uplift: a new mechanism for explaining Rwenzori Mountains' extreme elevation? Int. J. Earth Sci. 99, 1511-1524.

Warren, J.M., Shimizu, N., Sakaguchi, C., Dick, H.J.B., Nakamura, E., 2009. An assessment of upper mantle heterogeneity based on abyssal peridotite isotopic compositions. J. Geophys. Res. 114, B12203.

Warren, R.G., 1978. Characterization of the lower crust-upper mantle of teh Engle basin, Rio Grande rift, from a petrochemical and field geologic study of basalts and their inclusions, Geological Sciences. Universty of New Mexico, Albuquerque, p. 156.

Warren, R.G., Kudo, A.M., Keil, K., 1979. Geochemistry of lithic and single-crystal inclusions in basalt and a characterization of the upper mantle-lower crust in the Engle basin, Rio Grande rift, New Mexico, in: Riecker, R.E. (Ed.), Rio Grande rift: tectonics and magmatism. American Geophysical Union, Washington, pp. 393-415.

Wilkinson, J.F.G., 1975. Ultramafic inclusions and high pressure megacrysts from a nephelinite sill, Nandewar Mountains, north-eastern New South Wales, and their bearing on the origin of certain ultramafic inclusions in alkaline volcanic rocks. Contributions to Mineralogy and Petrology 51, 235-262.

Wilshire, H.G., Shervais, J.W., 1975. Al-augite and Cr-diopside ultramafic xenoliths in basaltic rocks from western United States. Physics and Chemistry of the Earth 9, 257-272.

Wilson, D., Aster, R., Ni, J., Grand, S., West, M., Gao, W., Baldridge, W.S., Semken, S., 2005. Imaging the seismic structure of the crust and upper mantle beneath the Great Plains, Rio Grande Rift, and Colorado Plateau using receiver functions. J Geophys Res-Sol Ea 110.

Witt-Eickschen, G., O'Neill, H.S.C., 2005. The effect of temperature on the equilibrium distribution of trace elements between clinopyroxene, orthopyroxene, olivine and spinel in upper mantle peridotite. Chemical Geology 221, 65-101.

Witt-Eickschen, G., Palme, H., O'Neill, H.S.C., Allen, C.M., 2009. The geochemistry of the volatile trace elements As, Cd, Ga, In and Sn in the Earth's mantle: New evidence from in situ analyses of mantle xenoliths. Geochimica et Cosmochimica Acta 73, 1755-1778.

Wood, B.J., Blundy, J.D., 1997. A predictive model for rare earth element partitioning between clinopyroxene and anhydrous silicate melt. Contributions to Mineralogy and Petrology 129, 166-181.

Wood, B.J., Blundy, J.D., 2003. 2.09 - Trace Element Partitioning under Crustal and Uppermost Mantle Conditions: The Influences of Ionic Radius, Cation Charge, Pressure, and Temperature, in: Holland, H.D., Turekian, K.K. (Eds.), Treatise on Geochemistry. Pergamon, Oxford, pp. 395-424.

Workman, R.K., Hart, S.R., 2005. Major and trace element composition of the depleted MORB mantle (DMM). Earth and Planetary Science Letters 231, 53-72.

Wu, F.-Y., Walker, R.J., Yang, Y.-H., Yuan, H.-L., Yang, J.-H., 2006. The chemical-temporal evolution of lithospheric mantle underlying the North China Craton. Geochimica et Cosmochimica Acta 70, 5013-5034.

Yao, L., Sun, C., Liang, Y., 2012. A parameterized model for REE distribution between low-Ca pyroxene and basaltic melts with applications to REE partitioning in low-Ca pyroxene along a mantle adiabat and during pyroxenite-derived melt and peridotite interaction. Contributions to Mineralogy and Petrology 164, 261-280.

Yu, S.-Y., Xu, Y.-G., Huang, X.-L., Ma, J.-L., Ge, W.-C., Zhang, H.-H., Qin, X.-F., 2009. Hf-Nd isotopic decoupling in continental mantle lithosphere beneath Northeast China: Effects of pervasive mantle metasomatism. Journal of Asian Earth Sciences 35, 554-570.

Zandt, G., Myers, S.C., Wallace, T.C., 1995. Crust and mantle structure across the Basin and Range-Colorado Plateau boundary at 37°N latitude and implications for Cenozoic extensional mechanism. J Geophys Res-Sol Ea 100, 10529-10548.

Zhang, J., Wang, C., Wang, Y., 2012a. Experimental constraints on the destruction mechanism of the North China Craton. Lithos 149, 91-99.

Zhang, M., Yang, J.-H., Sun, J.-F., Wu, F.-Y., Zhang, M., 2012b. Juvenile subcontinental lithospheric mantle beneath the eastern part of the Central Asian Orogenic Belt. Chemical Geology 328, 109-122.

Vita

Benjamin Byerly was born in Baton Rouge, Louisiana in 1986 to Maud Walsh and Gary Byerly. He attended McKinley Senior High School in Baton Rouge, Louisiana and graduated in May 2004. He enrolled at the University of Oregon in Eugene, Oregon in September 2004. He received his Bachelor of Science with departmental honors in Geological Sciences from the University of Oregon in June 2008. In August 2008 he enrolled in the Graduate School at the University of Texas at Austin.

Permanent address: benbyerly@utexas.edu

This dissertation was typed by the author.